THERMO-MECHANICAL FATIGUE CRACK GROWTH MODELING OF A NICKEL-BASED SUPERALLOY

A Thesis
Presented to
The Academic Faculty

By

Vincent Mark Barker

In Partial Fulfillment
Of the Requirements for the Degree
Master of Science in the
George W. Woodruff School of Mechanical Engineering

Georgia Institute of Technology

August 2011

THERMO-MECHANICAL FATIGUE CRACK GROWTH MODELING OF A NICKEL-BASED SUPERALLOY

Approved by:

Dr. W. Steven Johnson, Advisor
School of Materials Science and Engineering, George W. Woodruff School of Mechanical Engineering
Georgia Institute of Technology

Dr. Stephen D. Antolovich
School of Materials Science and Engineering, George W. Woodruff School of Mechanical Engineering
Georgia Institute of Technology

Dr. Richard W. Neu
School of George W. Woodruff School of Mechanical Engineering, School of Materials Science and Engineering
Georgia Institute of Technology

Date Approved: April 27, 2011

ACKNOWLEDGEMENTS

I would like to acknowledge the many people who have supported and encouraged me throughout this project. First, I want to thank my advisor, Dr. Steve Johnson, for providing valuable insight and direction for this project and for giving me the opportunity to work under his guidance. I would also like to thank Dr. Stephen Antolovich for challenging me to grow in areas that I would otherwise not want to venture. In addition, I am appreciative of Dr. Richard Neu for being on my committee and providing technical insight into this project.

I would like to thank Pratt and Whitney for supplying the materials used in this project and for the hard efforts of Dr. Alexander Staroselsky for working as the Pratt and Whitney technical monitor.

I am grateful for the assistance and support from my fellow peers, Benjamin Adair, Dr. Robert Amaro, and Patxi Fernandez-Zelaia. Their experience with testing procedures and insight into explaining the results was invaluable. I would also like to thank Rick Brown for his extensive knowledge in experimental testing methods and for helping me conduct useful experiments.

Lastly, I am thankful for the support from my friends and family. This thesis is a combined effort from all of these people. Without them, it would not be possible.

TABLE OF CONTENTS

LIST OF TABLES

LIST OF FIGURES

LIST OF SYMBOLS AND ABBREVIATIONS

A	No Retardation Ratio
ASTM	American Society for Testing and Materials
B	Cut Off Ratio
C_f	Foreman Coefficient
c_p	Specific Heat at Constant Pressure
C_p	Paris Coefficient
CT	Compact Tension
da/dN	Increment of Crack Growth per cycle
$\triangle$Keff	Effective Stress Intensity Range
$\triangle$T	Change in Temperature
E	Young's Modulus
HIP	Hot Isostatic Pressing
IN-100	Inconel 100
K	Stress Intensity Factor
K_c	Fracture Toughness
K_{max}*	Nominal Stress Intensity Factor
K_{max}^{OL}	Overload Stress Intensity Factor
K_{op}	Crack Opening Stress Intensity Factor
Kr^*	Residual Stress Intensity Factor with Temperature Variability
Kr_W	Gallagher's Modified Residual Stress Intensity Factor

m	Strain Rate Sensitivity Parameter
$\dot{m}$	Mass Flow Rate
MPYZ	Multi Parameter Yield Zone
n_f	Foreman Exponent
n_p	Paris Exponent
P/M	Powder Metallurgy
PLC	Portevin-Le Chatelier
R	Load Ratio
R_{eff}	Effective R-ratio
R_p	Pressure Ratio
r_p	Plastic Zone Size
SEM	Scanning Electron Microscopy
SENT	Single Edge Notched Tension
S-N	Stress Life
SRS	Strain Rate Sensitivity
TMF	Thermo-Mechanical Fatigue
$\dot{W}$	Rate of Work
Y	No Underload Ratio
Z	Full Underload Ratio
Z_{OL}	Overload Plastic Zone Size
α	Stress State (Plane Stress/Plane Strain)

γ	Gamma Matrix
γ	Gamma Double Prime Strengthening Particles
γ'	Gamma Prime Strengthening Particles
ρ	Density
σ_d	Disk Stress
σ_y	Yield Strength
ω	Rotational Velocity

SUMMARY

A model was created to predict the thermo-mechanical fatigue crack growth rates under typical engine spectrum loading conditions. This model serves as both a crack growth analysis tool to determine residual lifetime of ageing turbine components and as a design tool to assess the effects of temperature and loading variables on crack propagation. The material used in the development of this model was a polycrystalline superalloy, Inconel 100 (IN-100).

The first step in creating a reliable model was to define the first order effects that influence TMF crack growth in a typical engine spectrum. Load interaction effects were determined to be major contributors to lifetime estimates by influencing crack growth rates based upon previous load histories. A yield zone model was modified to include temperature dependent properties that controlled the effects of crack growth retardation and acceleration based upon overloads and underloads, respectively. Multiple overload effects were included in the model to create enhanced retardation compared to single overload tests. Temperature interaction effects were also considered very important due to the wide temperature ranges of turbine engine components. Oxidation and changing temperature effects were accounted for by accelerating crack growth in regions that had been affected by higher temperatures. Constant amplitude crack growth rates were used as a baseline, upon which load and temperature interaction effects were applied. Experimental data of isolated first order effects was used to calibrate and verify the model.

Experimental data provided the means to verify that the model was a good fit to experimental results. The load interaction effects were described by a yield zone model, which included temperature dependent properties. These properties were determined experimentally and were essential in the model's development to include load and temperature contributions. Other interesting factors became apparent through testing. It was seen that specific combinations of strain rate and temperature would lead to serrated yielding, discovered to be the Portevin-Le Chatelier effect. This effect manifested itself as enhanced hardening, leading to unstable strain bursts in specimens that cyclically yielded while changing temperature.

CHAPTER 1: INTRODUCTION

This chapter will discuss the research objectives and provide a motivation upon which the objectives were defined. A thesis overview is included at the end of this chapter that briefly discusses the contents of each chapter.

1.1 Objective

Scientists and engineers have attempted to understand fatigue behavior for centuries. To their credit, much success has been achieved from their hard works and intelligent minds. The amount of knowledge that has been published on this topic is tremendous and continues to grow.

Despite all of this, there remain many areas that need to be further understood. New materials require significant testing and characterization before implementation. Even well understood materials in new environments or under different loading conditions need to be evaluated to ensure adequate performance. This evaluation occurs by either extensive testing or accurately modeling the material behavior.

An objective of this research was to contribute to an area of fatigue analysis that has been left relatively unexplored. This area was identified as a load interaction and temperature dependent modeling approach to thermo-mechanical fatigue (TMF) crack growth. Load interaction models have been studied for many years; however, relatively little information is available which links load interaction to temperature dependent TMF

crack growth. How does cycling temperature affect variable amplitude crack growth rates? What influence will prior loading history have on a component that is subjected to creep, oxidation, and fatigue? These are the type of questions that spurred interest to study this topic.

The focus of this research is on a polycrystalline nickel-base superalloy known as Inconel 100 (IN-100). This alloy is used in turbine disk applications and has very good high temperature strength and fatigue characteristics. Experimental analysis on this alloy aided in the development of a robust load and temperature interaction model. Although the main focus is on one particular alloy, the modeling work was designed to be easily generalized to other material systems.

Several unexpected detours occurred in the process of studying the high temperature load interaction characteristics of IN-100. One was the occurrence of serrated plastic flow under certain testing conditions. Limited information is published about the Portevin-Le Chatelier effect in IN-100. Therefore, resources were used to further the understanding of this potentially damaging behavior.

The main goals of this research are to:

- Demonstrate a viable load interaction model which includes temperature dependent properties
- Provide additional insight into the high temperature behavior of IN-100
- Create a model which can be generalized to other material systems

- Accurately reflect the test results within a TMF load interaction crack growth model
- Exhibit an understanding of fatigue and fracture concepts and how they relate to complex, real world challenges

1.2 Motivation

Understanding the complex fatigue behavior of turbine engine components is vitally important to the companies who manufacture the engines and to the people who put their faith in the reliability of these components. The high risk inherent in this industry is amplified by the complex engineering challenges and the large envelope that these machines are expected to operate within. Substantial research costs are incurred in order to save money in the long term for repairs, replacements, or damages caused by catastrophic failures.

Engine failures can be classified as either contained or uncontained. Uncontained failures have fragments that penetrate the engine casing and are much more serious than contained engine failures, which occur inside the engine casing. Turbine disks are susceptible to uncontained failures because the engine casing is not designed to withstand an impact from a massive disk failure. Therefore, these components are usually labeled as fracture critical and are replaced at the slightest detection of damage.

A major disk failure occurred on June 2, 2006 at Los Angeles International Airport [1]. An American Airlines' owned Boeing 767 was performing a high-powered test run of a

GE built engine when a catastrophic disk failure occurred, sending fragmented disk pieces through the engine casing, as shown in figure 1.1, causing the aircraft to catch fire. Fortunately, nobody was injured; however, failures of this nature are extremely dangerous and very costly.

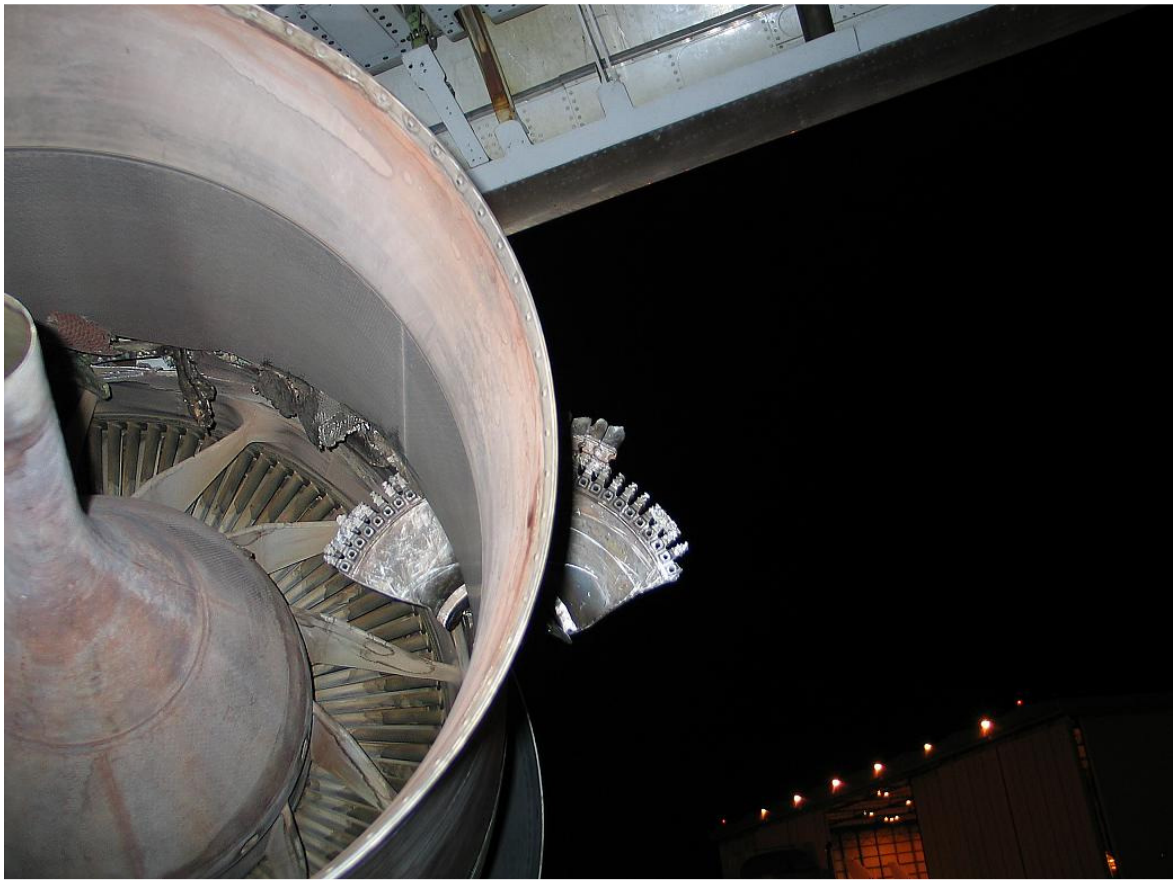

Figure 1.1 - Fragmented Disk from an American Airlines Flight Test [1]

More recently, Rolls-Royce has faced scrutiny due to an uncontained engine failure on a Qantas Airbus A380. On June 9, 2010, Rolls Royce's Trent 900 engine experienced an engine failure on a flight to Sydney from Singapore. The Trent 900 engine is the most common engine used on the A380, currently the world's largest commercial aircraft. The preliminary report suggests that a fatigue failure occurred in a misaligned stub pipe,

resulting in fire and eventually uncontained disk failure [2]. A piece of the fragmented disk is shown in figure 1.2.

Figure 1.2 - Large Piece of a Fracture Disk from a Qantas Airbus A380 [3]

If disks with apparent damage could be proven to have a remaining useful life and that amount of life is accurately quantifiable, then lots of money could be saved in the replacement of these disks. In addition, inspection intervals can be lengthened by gaining knowledge on the durability of these components. Aircraft down time would be kept to a minimum and the maintenance costs would decrease significantly.

The best way to mitigate the risks involved with turbine engines is to understand the mechanisms that control fatigue behavior and optimize the design to increase the useful lifetime of each component.

1.3 Thesis Overview

The overall goal of this thesis is to present a detailed methodology into the development of a variable temperature load interaction crack growth model. Chapter 2 provides a background analysis that describes the basics of a turbine engine and the design implications of a turbine disk and its alloys. Chapter two also highlights the history of fatigue and fracture mechanics, leading into the current technologies dealing with thermo-mechanical fatigue analysis. Past and present approaches to load interaction modeling are presented along with the advantages and disadvantages of each approach. Chapter two concludes with a brief literature review of dynamic strain ageing and its affect to the plastic flow in certain materials under specific testing conditions. Chapter three describes the materials, testing equipment, and testing procedure used in the development of the crack growth model. In this chapter, details are revealed about the microstructure characteristics of general IN-100 as well as the specific details about the processed form of IN-100 used in the model's development. Chapter four discusses the specific tests that were performed and includes an in-depth analysis on the results from these tests. This chapter concludes with an explanation of the dynamic strain ageing phenomenon and its relationship to both the monotonic and cyclic test results. Chapter five provides an in-depth analysis into the variable temperature load interaction model. This chapter begins by describing each facet of the crack growth model and the evolution from physical phenomenon to numerical modeling. The model is calibrated based upon experimental evidence and a series of parametric studies are performed which reveals the relative importance of specific variable on crack growth. Overload data and changing temperature studies are applied to the model to validate its capabilities. Chapter five concludes with user instructions on how to perform crack

growth analysis using this model. Lastly, chapter six summarizes the conclusions and suggests options for future work.

CHAPTER 2: BACKGROUND

This chapter will provide a detailed background analysis starting with basic turbine engine operation and turbine disk design requirements. The role of superalloys in turbine components will be discussed along with the various types and processing forms of superalloys. Next, a discussion on the fatigue and fracture design philosophy will outline the history of fatigue analysis, starting with traditional S-N curves and leading into the current fracture mechanics approach to fatigue crack growth. In addition, a historical overview of modeling load interaction effects will be presented. The last section of this chapter will discuss the dynamic strain ageing effect in IN-100 and its possible implications on fatigue life.

2.1 Turbine Engine

The concept of using high pressure gasses to power machinery can be traced back to Hero's aeolipile in 100 B.C. [4]. Water was heated in an enclosed chamber to produce steam, which was forced through a smaller diameter pipe bent at an angle. This device was mounted on an axle, which rotated due to the moment created by the exiting water vapor. Technology has certainly advanced since these ancient times, but the basic mechanics behind the operation of these machines are as true today as they were thousands of years ago.

2.1.1 Ideal Brayton Cycle

Today's gas turbine engines operate under an open Brayton cycle in which, ideally, heat addition occurs at constant pressure (isobaric) and gas compression and extraction occur at constant enthalpy (isotropic). A schematic for an open Brayton cycle is shown in figure 2.1.

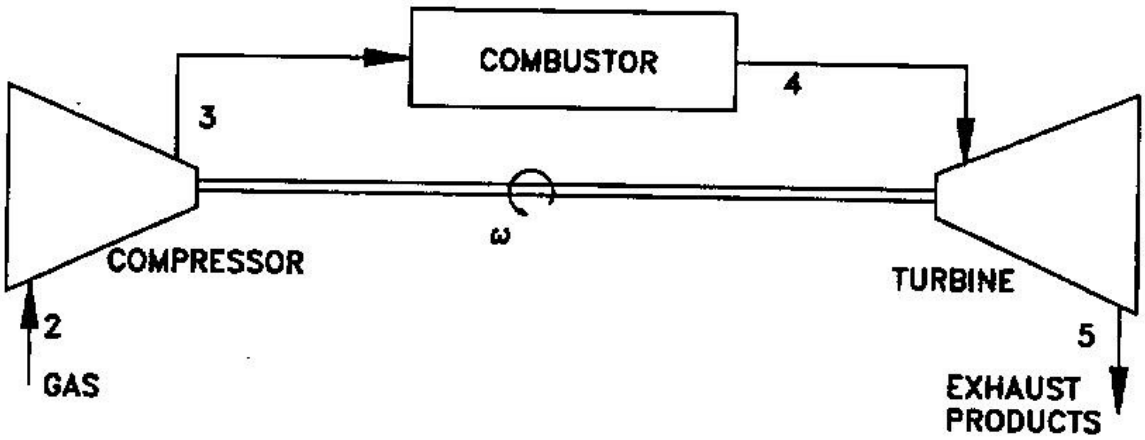

Figure 2.1 - Schematic of an Open Brayton Cycle [4]

The first stage in this cycle compresses inlet air to prepare it for combustion. Chemical energy in the jet fuel is converted into high-pressure potential energy during the combustion phase. Finally, the hot, high-pressure gasses are passed through a turbine and converted into two forms of energy: mechanical energy used to drive the compressor and kinetic energy, which provides the thrust out of the nozzle. This highly simplified, idealized model serves as the backbone behind the core functions of a turbine engine.

In terms of power output, an analysis of a closed Brayton cycle [5] reveals

$$\frac{\dot{W}}{\dot{m}} = c_p \left[T_4 \left(1 - R_P^{\frac{1-\gamma}{\gamma}} \right) + T_2 \left(1 - R_P^{\frac{\gamma-1}{\gamma}} \right) \right] \tag{2.1}$$

where T_4 is the turbine inlet temperature, T_2 is the compressor inlet temperature, c_p is the specific heat, $\dot{W}$ is the rate of output work, $\dot{m}$ is the mass flow rate, R_p is the pressure ratio, and γ is the ratio of specific heat. Therefore, in order to maximize the work output, the temperature at the turbine inlet (T_4) needs to be increased. This creates a limiting factor for turbine engine manufacturers who are restricted by component's structural limits at high temperature.

2.1.2 Modern Turbine Engines

Turbine engines can be classified into several different categories; however, the most popular type for both commercial and military aviation is the turbofan. A schematic of the turbofan is shown in figure 2.2.

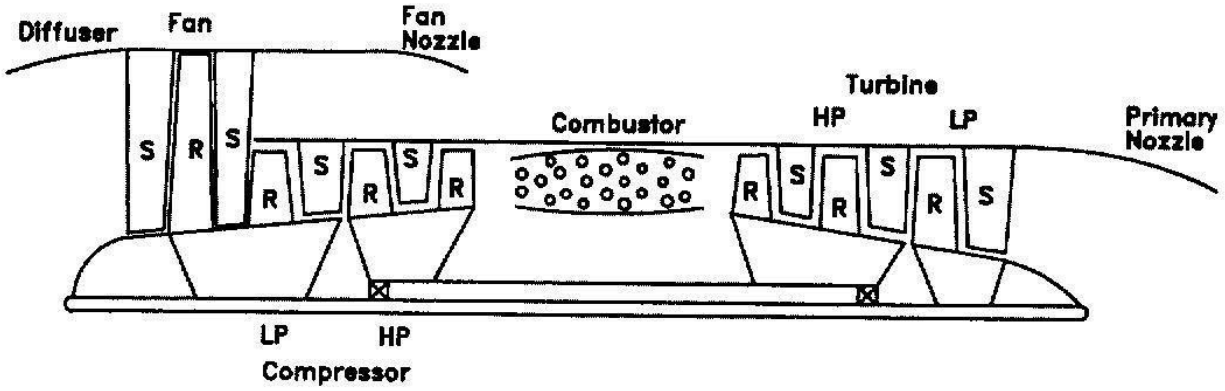

Figure 2.2 - Schematic of Turbofan with No Afterburner [4]

Turbofan engines have a stage prior to the compressor in which air is compressed and the temperature slightly increases. A “splitter” separates the fan and compressor stages, which divides the airstream into bypass air and core air. The bypass air is used for additional thrust, powering other components, and cooling the core stages. An afterburner can be added to the end of the turbine stage, before the primary nozzle, to increase the power output as shown in figure 2.3. Afterburners are not common in commercial aviation since the amount of power generated does not justify the added weight and lower fuel economy.

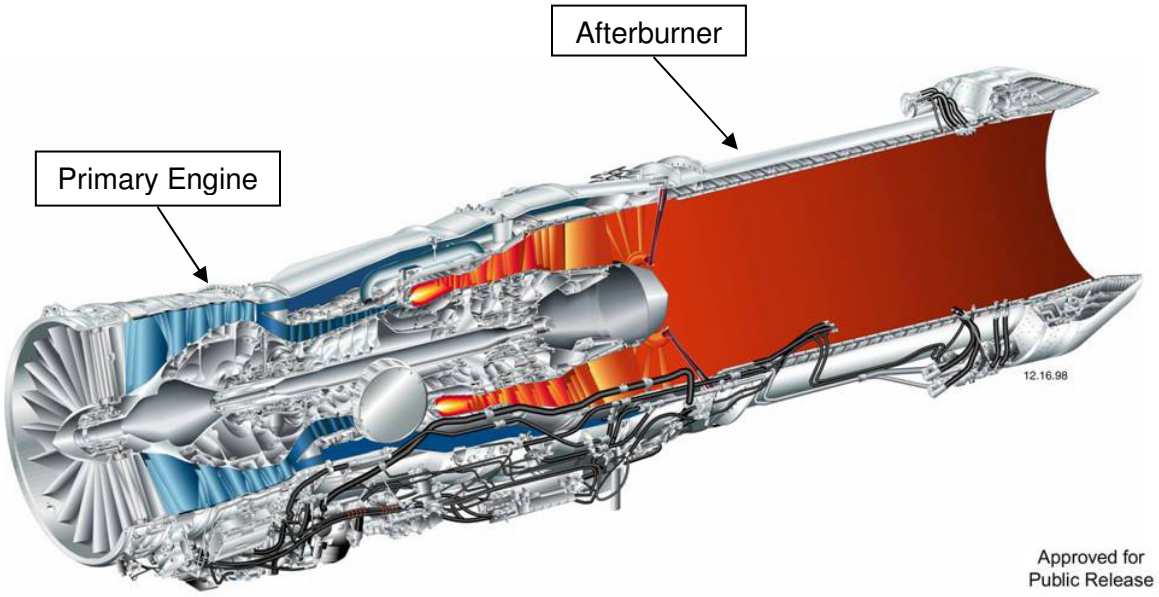

Figure 2.3 - F135 Engine Used for the F-35 Lightning II (Photo Courtesy of Pratt & Whitney)

2.1.3 Turbine Disks

The focus of this thesis is on turbine disk materials. Disks function as the “structural and dynamic stabilizing” component between the blade and the shaft [4]. Disks are used in the compressor and turbine engine stages with the purpose of transmitting energy

between the blades and shaft. They experience very high temperatures due to their proximity to the hot combustion gasses and must withstand high loads due to the centrifugal accelerations inherent in any rotating object. A schematic of the disk and its relation to the airfoil and shaft is shown in figure 2.4.

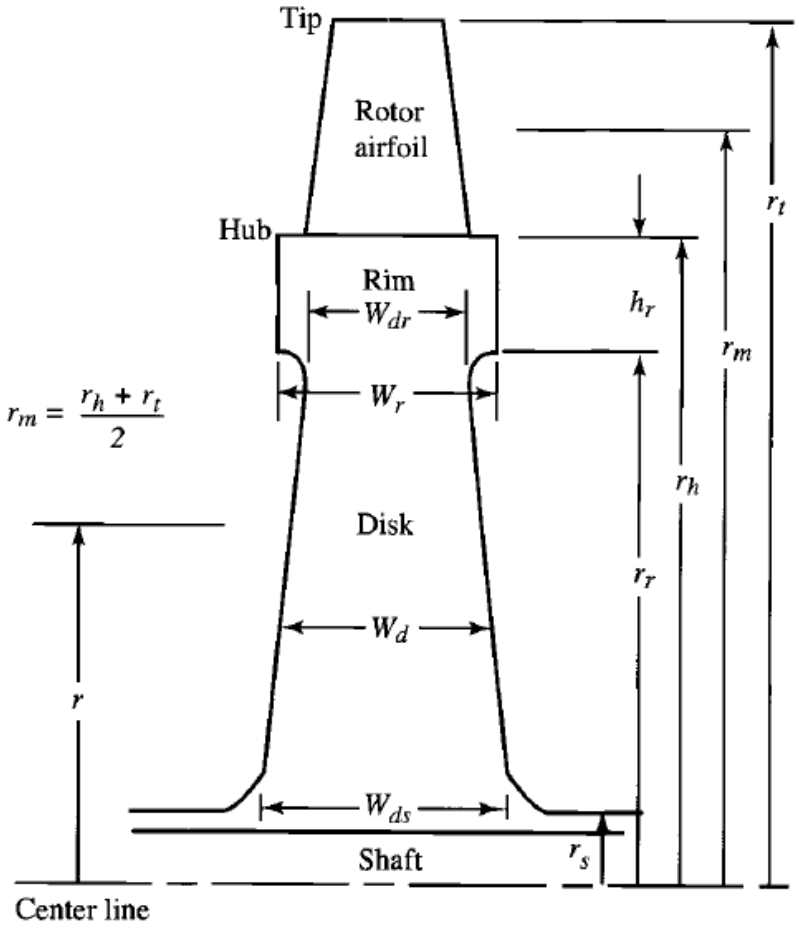

Figure 2.4 - Geometry of Shaft, Disk, Rim, and Airfoil [6]

Stresses within a turbine disk are hard to quantify analytically. Engine designers use complex finite element modeling in conjunction with engineering judgment to size each disk depending on the most severe loading conditions. Mattingly, Heiser, and Pratt [6]

identified three main sources of disk loading: Centrifugal dynamic stresses, torsional stresses, and thermally induced stresses due to temperature gradients. The largest loads are induced from the centrifugal stresses, which lead to the variation in web thickness with radius, derived as

$$\frac{W_d}{W_{dr}} = exp\left[\frac{\rho(\omega r_r)^2}{2\sigma_d}\left(1 - \left(\frac{r}{r_r}\right)^2\right)\right] \tag{2.2}$$

where W_d, W_{dr}, r, and r_r are defined in figure 2.4. Equation 2.2 shows that the thickness of the disk increases as the radius decreases due to the increase in circumferential forces. Another important aspect of equation 2.2 is the thickness dependence on the rim velocity, r_r. Higher rotational speeds increase the allowable thickness of the disk so designers must size the disk to an allowable rotational speed.

Torsional stresses only account for a small contribution to the overall stress state. However, thermal stresses induced by a temperature gradient can be significant. Assuming a constant thickness and linear temperature distribution, Mattingly et al. [6] determined that the maximum stress has a magnitude of $\frac{\alpha E \Delta T}{3}$ at r = 0. Using typical material properties, this maximum thermal stress is around 46.2 MPa. By comparison, the design stress for centrifugal stresses is around 138-207 MPa and the torsional stresses are usually less than 6.9 MPa [6]. This shows that the contribution of thermal stresses is significant and cannot be ignored.

2.2 Superalloys

Superalloys are known for their excellent high temperature properties and have been used for high temperature applications since their development in the 1940s [7]. Their superior strength, creep resistance, and corrosion resistance at high temperatures make them a capable material for turbine engines and have higher performance and life expectancies than most other materials at elevated temperatures. Aerospace applications constitute the majority of superalloy use, but these materials are also found in power plants, automotive components, metal processing, space vehicles, and chemical plant equipment [7].

There are three main types of superalloys: iron-nickel, cobalt, and nickel base [7]. Certain forms of superalloys perform better than others, depending on the application. Nickel base superalloys are the best choice for very high temperature applications but are more expensive than the other two categories. Most turbine disks and blades are nickel based. Iron-nickel superalloys are used at lower temperatures since the main alloying element, iron, quickly loses its strength at high temperatures. Cobalt base superalloys are used in corrosion sensitive applications, but they do not have the same temperature limits as nickel base superalloys.

Further classification of superalloys can be achieved by dividing each type of superalloy into cast and wrought categories. Wrought alloys are formed from cast billets which are thermo-mechanically processed until they reach their final shape [7]. Powder metallurgy falls under the wrought category and is used for many disk alloys with relatively difficult workability and complex geometries. Cast superalloys are generally higher strength and

less ductile than wrought alloys. They can be processed in a directionally solidified or single crystal form, increasing their resistance to environmental attack. The main focus of this research is on a powder metallurgy form of nickel based superalloy known as IN-100.

The microstructure of nickel base superalloys consists on an FCC matrix referred to as the gamma (γ) matrix. Most nickel base superalloys are precipitation strengthened by a dispersion of a Ni_3Al precipitates known as gamma prime (γ') particles [8]. These particles give the superalloys its strength at high temperatures. Grain boundaries are also reinforced by carbides and borides that provide additional strength, but these particles can also contribute to increased fatigue crack growth since environmental attack is accelerated at carbides located on grain boundaries. Figure 2.5 shows a schematic of a typical nickel base superalloy microstructure.

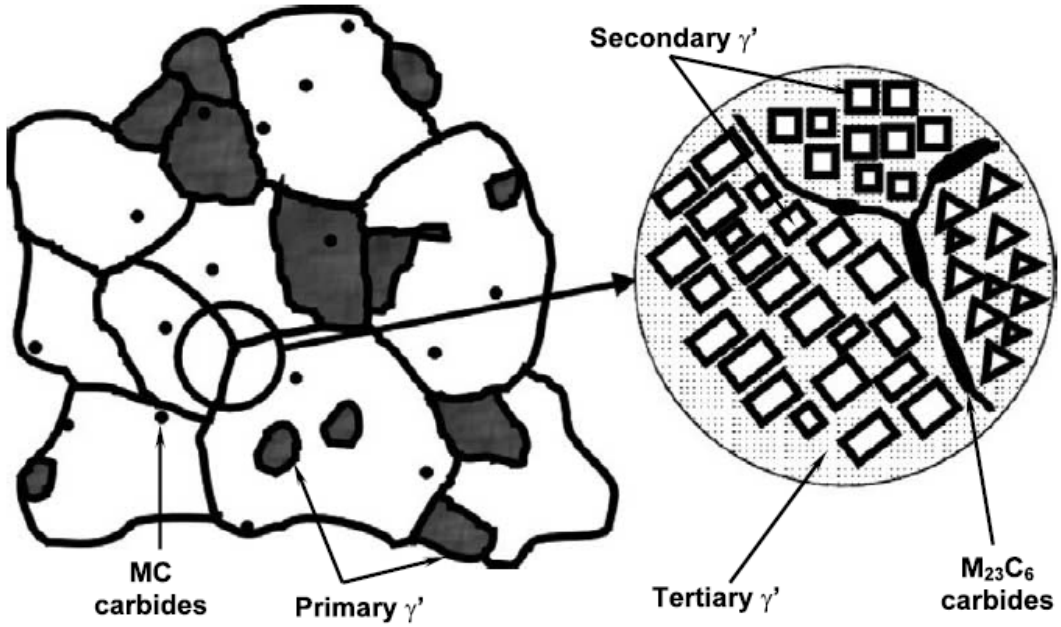

Figure 2.5 - Schematic of a Nickel-Based Superalloy Microstructure [9]

Studies have been done which have confirmed the role of γ' participates in maintaining the yield strength at high temperatures. Beardmore, Davies, and Johnston [10] showed that increasing the volume fraction of γ' particles increases the flow stress at high temperatures due to temperature dependent dislocation mechanisms. They discovered that the flow stress is a function of the γ' volume fraction at high temperatures since the strong γ' particles support the weaker γ matrix. At low γ' volume fractions, dislocations bow around the stronger particles and the flow stress decreases. At low temperatures, the γ' precipitates have lower strength than the matrix and the flow stress is a function of the matrix material [10]. The flow stress's dependence on temperature and γ' volume fraction is shown in figure 2.6.

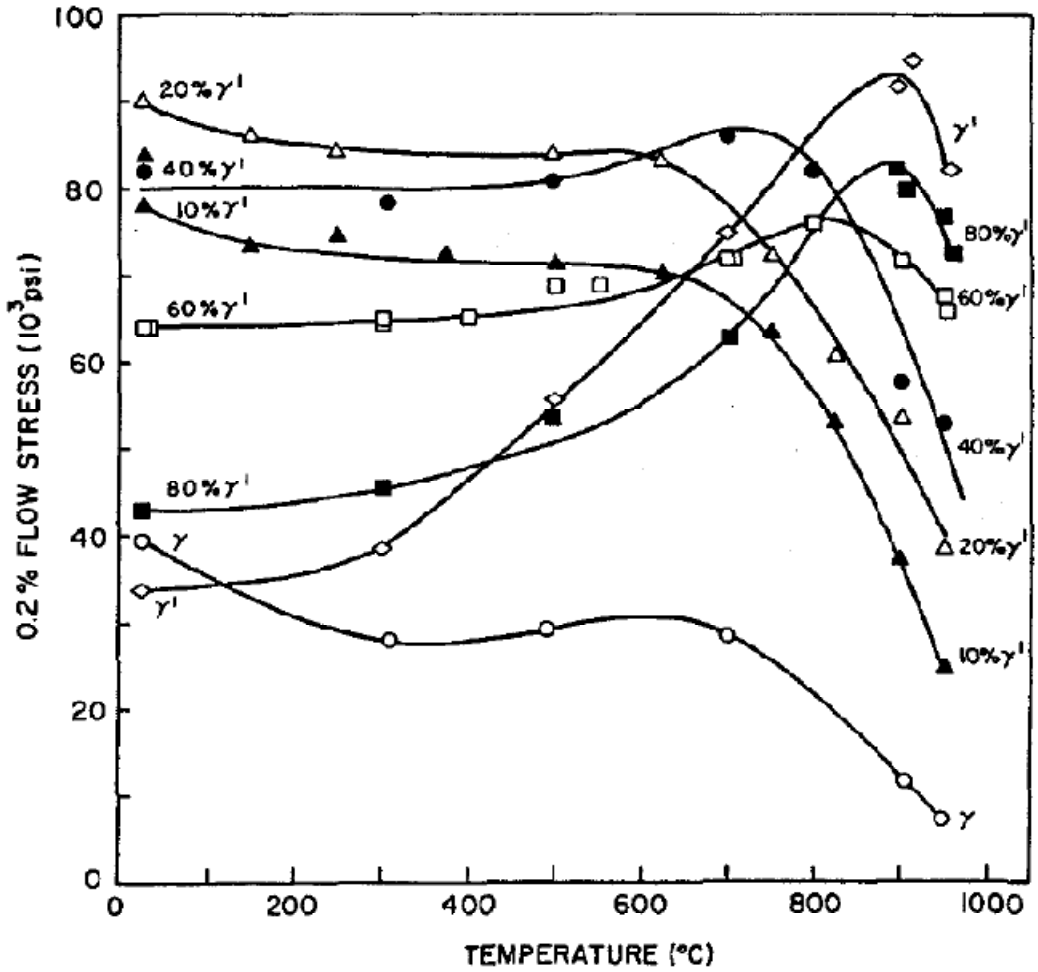

Figure 2.6 - Yield Strength Dependence on Temperature for Different Precipitation Volume Fractions [10]

The underlying mechanism behind the increase in yield strength with temperature is the formations of thermally activated Kear-Wilsdorf locks, causing a cross slip of dislocations from the octahedral to the cubic plane and increasing the critical resolved shear stress with temperature [11]. Kear-Wilsdorf locks were originally discovered in copper/gold alloys [12], but this effect is apparent in superalloys as well.

2.3 Fatigue and Fracture Design Philosophy

Fatigue and fracture design approaches have evolved over time as engineers have become more knowledgeable in the life expectancy of structural components. Unfortunately, many design changes are the result of unexpected failures, which force companies to reassess their design approach and come up with new ways to prove structural reliability. There are two main ideologies regarding the assessment of fatigue life: the safe-life approach and the damage tolerant design approach.

The traditional safe-life design approach is an older philosophy which uses S-N curves and experimentally determined fatigue lives to determine how long a component will last in service [13]. Components that reached the end of their service life are discarded and replaced with new material. In this way, preventative failures on ageing aircraft are maintained by continuously replacing parts. The two main drawbacks to this approach are costly expenses of continuously replacing components that may still have useful life and premature failure which persisted under the safe-life design philosophy.

The two main disadvantages of the safe-life approach led to the development of the current damage tolerance approach for fatigue and fracture analysis. Under this design philosophy, an initial flaw size is assumed present in every location within a structure. The crack propagates based upon external loading conditions and material data obtained from linear elastic fracture mechanics concepts. With the advancement in non-destructive testing technology, in-service components are examined at specific inspection intervals to monitor crack growth and assess the remaining amount of life.

This approach is less empirical than the safe-life approach and provides a cost savings to companies that would otherwise discard parts before their useful life is depleted.

2.4 Overview of Fatigue Behavior and Analysis

Predicting fatigue life has been extensively studied for many years and continues to be studied as a very technically challenging topic. Many advancements have been made to increase the accuracy of lifetime predictions but the variability of fatigue analysis creates more opportunities to further develop this technology. This section will provide a historical view of fatigue analysis, outline current methods used to predict crack growth, discuss the micromechanisms driving fatigue behavior in metals, and examine the variables that influence fatigue behavior in a TMF environment.

2.4.1 Traditional S-N Approach

One of the first significant contributions to the area of lifetime prediction is August Wöhler's development of S-N curves from data obtained from railroad components. An example of an S-N curve for wrought steels is shown in figure 2.7.

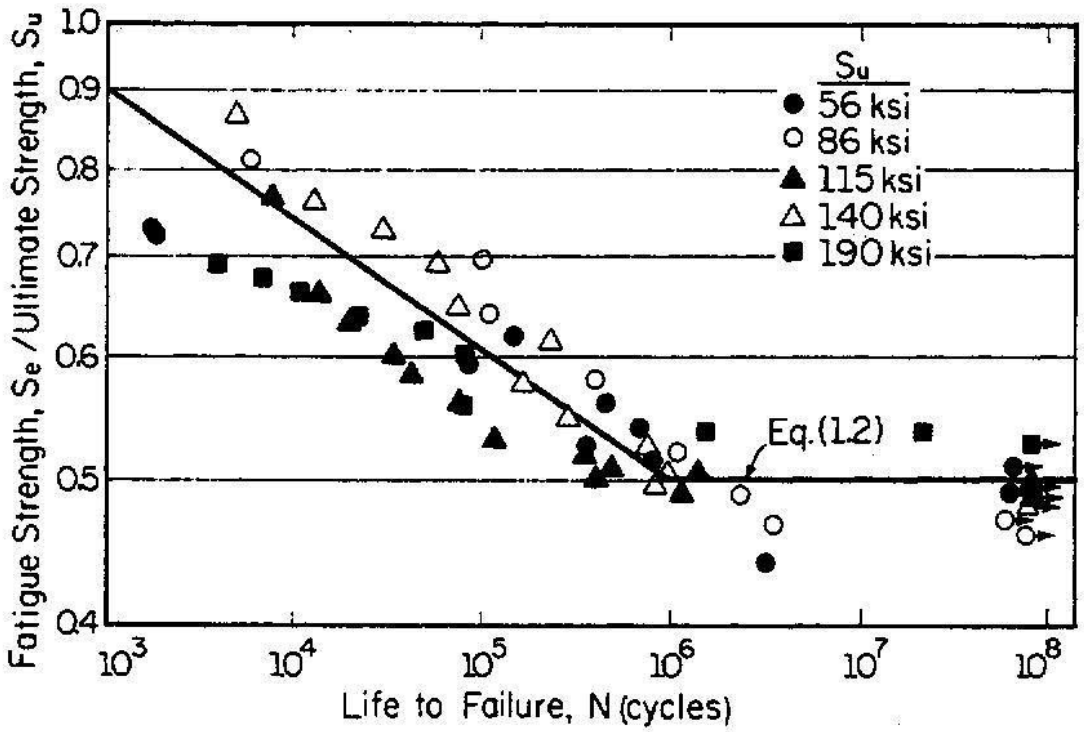

Figure 2.7 - S-N Curve of Several Wrought Steels [14]

S-N curves are widely used as a stress life approach for high cycle fatigue applications because they provide a straightforward way to determine how much useful life is left at specific stress levels. Another important outcome of the S-N approach is the development of the endurance limit. The endurance limit is a stress level used in design to ensure that components could reach infinite lifetime (~10^6 cycles) if cycled at a stress below the endurance limit. However, recent research reveals that the concept of an endurance limit is not accurate and failure can still occur after 10^6 cycles [15, 16].

Although the stress life approach revolutionized the way researchers approached fatigue analysis, it has its drawbacks. The biggest disadvantage is the amount of data needed to create S-N diagrams. Bannantine, Comer, and Handrock [14] list the weaknesses of the stress life method as

- Completely empirical in nature
- Ignored the true stress-strain response
- No distinction between initiation and propagation

Due to these limiting factors and the development of current fracture theories, a new method of lifing components came to fruition. This new method is based on fracture mechanics principles and it is the current design approach used by most advanced technological industries.

2.4.2 Fracture Mechanics Approach

In 1920, Griffith [17] published his famous work which related fracture to the material's inherent resistance. He used an energy approach to formulate the relationship between the potential energy due to internal strain energy or external forces to the work required to cause fracture. This approach worked well for brittle solids but did not apply to ductile materials with large amounts of plastic deformation. Although limited in nature, Griffith's ideas increased interest within the fatigue and fracture community and led to much advancement in the area of fracture mechanics and fatigue analysis.

Irwin and Orowan independently extended Griffith's energy theory to include crack extension in semi-brittle metals by adding a term which included the work due to plastic deformation [18] as shown in equation 2.3.

$$\sigma_f = \left(\frac{2E(\gamma_s + \gamma_p)}{\pi a}\right)^{1/2} \quad (2.3)$$

where σ_f is the fracture stress, E is the modulus of elasticity, a is the crack length, γ_s is the surface energy, and γ_p is the plastic work per unit area. Irwin also developed solutions to stresses at a crack tip [19] which led to the formation of the stress intensity factor, K. This parameter characterizes crack tip conditions in structures with small amounts of plasticity and is used as the leading driving force in crack propagation. Irwin's contributions to the fatigue and fracture community were invaluable since they advanced the development of the methodologies used today.

Paris, Gomez, and Anderson [20] were the first to publish the relationship between the stress intensity factor and crack growth rates. It was discovered that the change in crack growth per cycle was dependent on the stress intensity factor and was not directly influenced by geometry, test frequency, or stress level. This was a major discovery that led to the application of LEFM to fatigue crack growth. The Paris correlation, equation 2.4, is one of the most famous relationships between crack growth rate and stress intensity range and, in most cases, adequately describes stage II crack growth.

$$\frac{da}{dN} = C_p \Delta K^{n_p} \quad (2.4)$$

where dadN is the crack growth rate, C_p is the Paris Coefficient, ΔK is the stress intensity range, and n_p is the Paris exponent. The Paris correlation can be used to predict crack growth rates in components subjected to comparable conditions for which

the Paris coefficients, C_p and n_p, are defined. Fatigue crack growth testing is currently governed by ASTM standard E647.

2.4.3 Micromechanics of Crack Growth

The micromechanics of crack growth have evolved over time, which has led to the current understanding of high cycle fatigue crack growth. The notion that structures subjected to purely elastic cyclic loading and still failed created the need to look more closely at small-scale plasticity around defects. Orowan [21] stated that small scale yielding occurs in grains with favorable orientation or around cracks and notches, even under elastic conditions. During cyclic loading, the yielded region undergoes further plastic deformation and the stresses in this region increase due to the hardening behavior caused by dislocation interaction. At some point, the stresses within the yielded region will exceed the fracture strength and a crack will form or a propagating crack will increase in length. This process happens on a small scale; however, accumulating damage eventually leads to a total fatigue failure across the entire specimen.

2.4.4 TMF Crack Growth

Thermo-mechanical fatigue crack growth is more complicated than pure fatigue crack growth because it includes time dependent material behavior characteristics such as creep and oxidation. Increasing temperature will activate specific mechanisms that can cause more damage than what would be expected by the individual contributions acting alone.

Ghonem, Nicholas, and Pineau [22] studied the effects of mechanical variables during high temperature fatigue crack growth in alloy 718, a precipitation hardened nickel base superalloy. They looked at temperature, frequency, wave shape, hold time, and load interaction effects to assess the significance of each variable on high temperature crack growth. It was shown that fatigue crack growth rates increase with temperature due to oxidation embrittlement at the crack tip. Subsequent fractography showed a transition from low temperature transgranular crack growth to high temperature intergranular crack growth due to grain boundary weakening from environmental attack.

Frequency effects in IN100 were studied by Reger and Remy [23] in both an air environment and inside a vacuum. The vacuum isolates oxidation effects and provides a good measure of the amount of damage attributed to material degradation due to fatigue alone. It was shown that slower frequencies decrease the fatigue life in an oxygen atmosphere by allowing more oxidation to occur during each cycle. The fatigue life increases with frequency, approaching the lifetimes of specimens tested in the vacuum. Figure 2.8 shows some results from this study in which the initiation life of several IN-100 specimens were determined in air and vacuum environments at various strain rates.

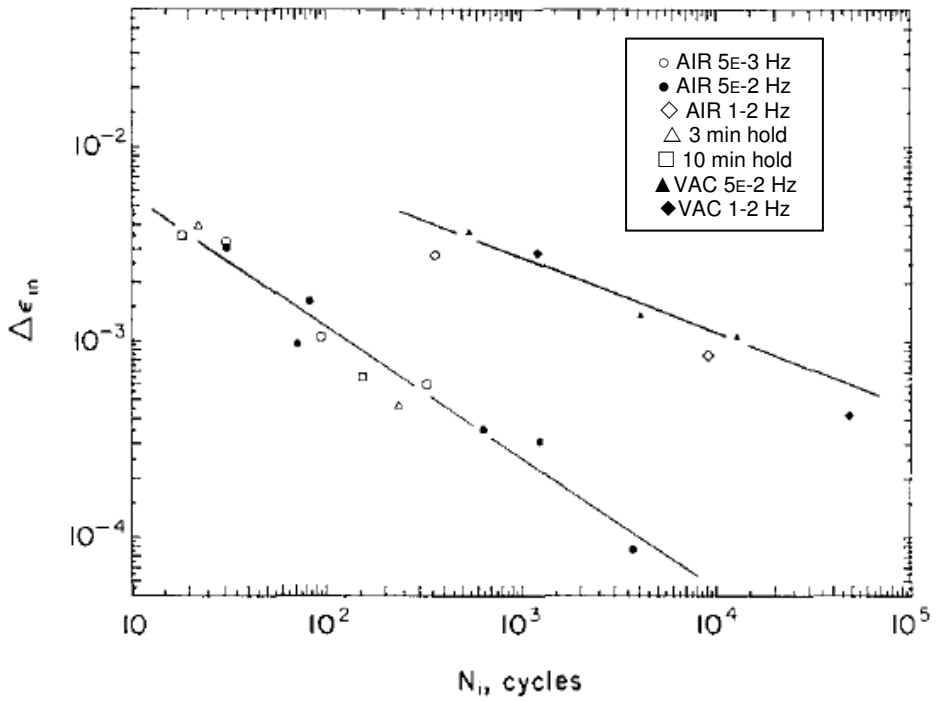

Figure 2.8 - Life to Crack Initiation as a Function of Inelastic Strain Range at 1000°C [23]

The data shows that the initiation life increased for all tests within the vacuum. In addition, the tests at 1-2 Hz in an air environment had initiation lives closer to the specimens tested in a vacuum rather than the slower frequency specimens tested in air. This suggests that high frequency loading is relatively insensitive to the testing environment and that oxidation can have a significant influence on the fatigue life for specimens tested in an air environment at low frequencies. Oxide growth does not have sufficient time to develop when cracking occurs at high frequencies; therefore, loading at high rates reduces the effect of accelerated oxide cracking.

The fracture mechanism can change depending on high temperature testing conditions and this phenomenon can be used to assess the role of environment in propagating cracks. Transgranular fracture occurs when environmental conditions have little effect

on the propagating crack. This can occur at low temperatures, high frequencies, and high delta K values. Intergranular fracture occurs along grain boundaries which are influenced by complex interactions between many local variables at high temperatures [24]. This complex phenomenon is hard to quantify but the identification of transgranular and intergranular fracture is relatively straightforward by looking at the fracture surface under a microscope.

2.5 Load Interaction – Yield Zone Approach

The influence of load interaction effects has been studied extensively in the works of Willenborg, Engle, and Wood [25] and Wheeler [26] in the early 1970s. Willenborg et al. used an effective stress concept to reduce the overall stress range after an applied overload. The larger plastic zone ahead of the crack tip created a compressive zone that reduced crack growth within the overloaded zone.

Willenborg's effective stress concept was modified in 1974 by Gallagher and Hughes [27]. A study on 4340 steel showed that the yield strength's significance on crack growth could not be ignored. Materials with lower yield strength create larger plastic zones according to the equation for the monotonic plastic zone size.

$$r_p = \frac{1}{\alpha\pi}\left(\frac{K_I}{\sigma_y}\right)^2 \tag{2.5}$$

where r_p is the plastic zone size, α describes the stress state, σ_y is the yield strength, and K_I is the stress intensity factor. Gallagher et al. assumed the same conditions

during the overload and nominal load cycles and devised a modified residual stress intensity relation.

$$K_R^W = K_{max}^{OL}\sqrt{1-\frac{\Delta a}{Z_{OL}}} - K_{max}^{\infty} \tag{2.6}$$

where K_R^W is the residual stress intensity factor, K_{max}^{OL} is the overload stress intensity, Δa is the increment of crack growth through the overload zone, Z_{OL} is the overload zone size, and K_{max}^{∞} is the nominal maximum stress intensity factor. The residual stress intensity factor is the amount of stress intensity that needs to be applied in order for the plastic zone to touch the outer boundary of the overloaded plastic zone. Gallagher's relationship has been used by subsequent crack growth models to account for load interaction effects in variable amplitude load spectrums. A schematic of this parameter is shown in figure 2.9.

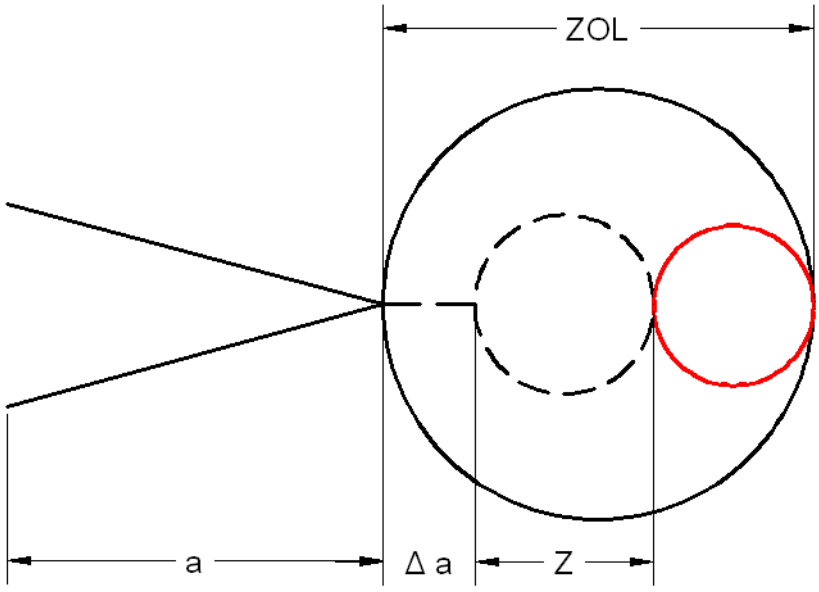

Figure 2.9 - Schematic of Residual Plastic Zone Size (in red)

Johnson [28] published a multi-parameter yield zone (MPYZ) approach to crack growth modeling based on Gallagher's modification to Willenborg's residual stress intensity factor. This semi-empirical model includes factors that influence crack growth based on the amount of overload and underload applied to the crack and predicts crack growth using the Foreman relation, equation 2.7.

$$\frac{da}{dN} = \frac{C_f \Delta K^{n_f}}{(1 - R_{eff})\, K_C - \Delta K} \tag{2.7}$$

where C_f is the Foreman coefficient, n_f is the Forman exponent, R_{eff} is the effective load ratio, and K_c is the fracture toughness. The shut off ratio was included to stop crack growth after an overload was applied that exceeded a predetermined overload ratio. Data shows that crack growth is significantly reduced to the point of crack arrest as the overload to nominal load ratio approaches a "shut off" value. Conversely, there are overload values that are small enough that do not reduce crack growth. Johnson defined this overload to nominal load ratio as the "no retardation ratio." The shut off ratio is between 2 and 2.3 and the no retardation ratio is around 1.3 for the aluminum specimens tested in the validation of the MPYZ model.

In addition to overload effects, the influence of underloads was also considered in Johnson's MPYZ model. An underload is a minimum load applied during cyclic loading which is less than the nominal minimum load from previous cycles. Experimental evidence suggests that underloads decrease the amount of retardation which results from a previous overload [29] and in some cases can also contribute to crack growth

acceleration. The MPYZ model reduced the remaining overload cycles to account for underload effects by utilizing two empirical constants, Y and Z. These two constants provided a linear relationship between underloads that produced no changes in the retardation behavior and underloads that negated all amounts of reduced crack growth caused by overloads.

ASTM Special Technical Publication (STP) 748 outlines different modeling approaches to variable amplitude crack growth predictions and includes Johnson's MPYZ model. To test each model's validity, a variable amplitude load spectrum was applied to test specimens for various flight conditions. These same spectrums were inputs into the different models to determine which had the most accurate and consistent predictions. table 2.1 shows some results from this study.

Table 2.1 - Results from STP 478 Variable Amplitude Load Spectrum Predictions [30]

			Analytical Predictions, cycles; (Npred/Ntest)					
Test No.	**Mission Type**	**Test Life, cycles; (ci to cf, in)**	**JC (1)**	**CMH**	**JN**	**WSJ**	**JR**	**JC (2)**
M-81	Air-Air	115700	140720	246000	115800	137000	213110	168720
	DLS = 20 ksi	(0.16 to 0.501)	(1.21)	(2.13)	(1.01)	(1.18)	(1.84)	(1.46)
M-82	Air-Air	58585	44525	79000	39125	57000	74055	53312
	DLS = 30 ksi	(0.15 to failure)	(0.76)	(1.35)	(0.67)	(0.97)	(1.26)	(0.91)
M-83	Air-Air	18612	14703	25359	11940	19700	25944	17309
	DLS = 40 ksi	(0.15 to failure)	(0.79)	(1.36)	(0.64)	(1.06)	(1.39)	(0.93)
M-84	Air-Ground	268908	302816	395292	396230	342000	496284	368662
	DLS = 20 ksi	(0.158 to failure)	(1.13)	(1.47)	(1.47)	(1.27)	(1.85)	(1.37)
M-85	Air-Ground	95642	73644	99368	84850	90020	131868	91816
	DLS = 30 ksi	(0.144 to failure)	(0.77)	(1.04)	(0.89)	(0.94)	(1.38)	(0.96)
M-86	Air-Ground	36367	23275	29789	23820	30000	45034	29093
	DLS = 40 ksi	(0.153 to failure)	(0.64)	(0.82)	(0.65)	(0.82)	(1.24)	(0.80)
Average (Npred/Ntest)			0.88	1.36	0.89	1.04	1.49	1.07
Standard Deviation			0.23	0.45	0.32	0.17	0.28	0.27

The results for the air-air and air-ground maneuvers show a relatively wide range of predicted lives between all the models. The variability of fatigue analysis makes it difficult to capture all the physics involved in crack growth. However, the MPYZ model (labeled WSJ) shows the closest average prediction to test ratio with a relatively small standard deviation.

2.6 Other Load Interaction Models

Skorupa [31] performed a literature study on different approaches to accounting for load interaction effects in fatigue analysis. Six dominate mechanisms were identified which can be used to explain the crack growth in non-uniform cycles. Those six mechanisms as identified by Skorupa are crack tip blunting, residual stresses ahead of the crack tip, strain hardening ahead of the crack tip, plastically-induced crack closure, irregular crack front, and an occurrence of specific stress/strain conditions ahead of the crack tip.

2.6.1 Crack Tip Blunting

It is postulated that crack tip blunting can lead to retardation in crack growth rates by reducing the local stress concentration at the crack tip [32]. Fleck [33] provides evidence against this theory since it contradicts the existence of delayed retardation after an overload. If crack tip blunting is the main mechanism for retardation, then crack growth delay should occur immediately after the application of an overload. Immediate delay is not supported by experimental evidence; therefore, crack tip blunting is probably not the dominate mechanism for load interaction effects.

2.6.2 Residual Stresses

The residual stress approach accounts for compressive residual stresses ahead of the crack tip, reducing the effective stress ratio. The structure of Johnson's MPYZ model is based on a residual stress concept outlined previously. X-ray diffraction studies performed by Busch and Lebrun [34] on steel specimens showed that the stress distribution ahead of a crack is the summation of the stress prior to the overload and

compressive stress immediately following the overload. The stress distribution ahead of the crack is shown in figure 2.10.

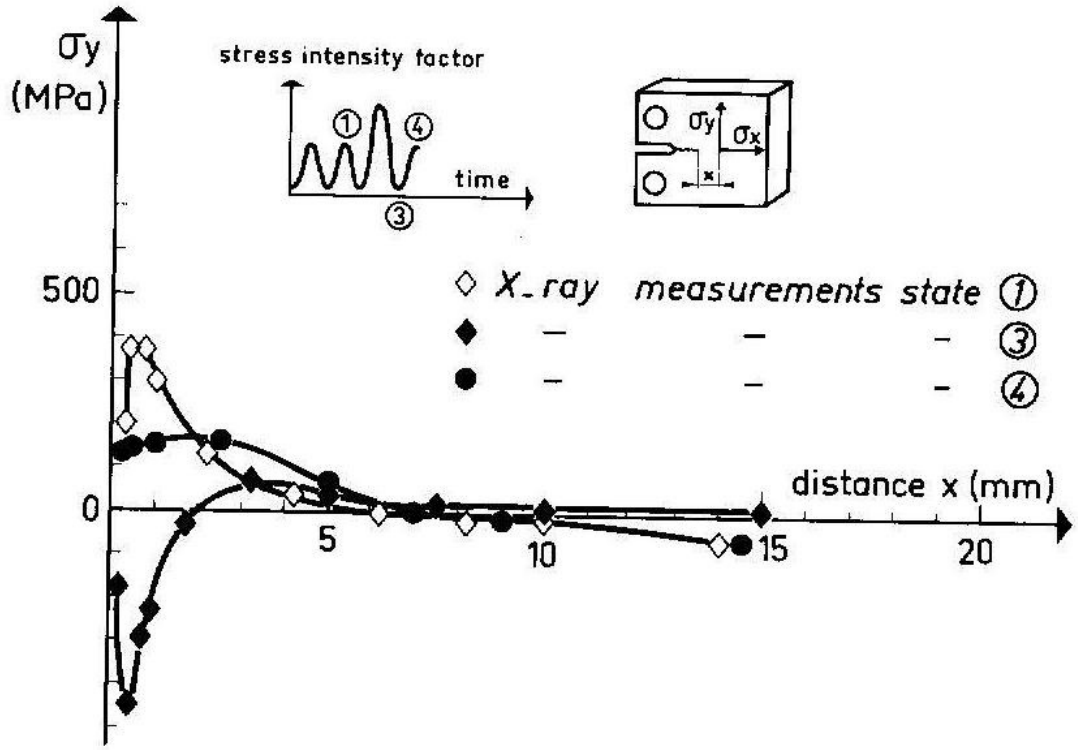

Figure 2.10 - X-ray Diffraction Measurements on the Stress Profile Before and After an Overload [34]

The X-ray diffraction study performed by Busch et al also provided a good indication of the size of the overloaded affected zone. The x-ray depth was only a few micrometers so the distribution shown in figure 2.10 can be assumed to be the plane stress (α=1) condition at a free surface. Using equation 2.4, the size of the monotonic plastic zone was determined to be 5.47 mm. According to figure 2.10, the affected zone size after the overload is approximately 2 mm. This result supports the notion that the cyclic plastic yield zone is a better indication of determining the affected yield zone size, which influences crack retardation behavior. The cyclic yield zone can be approximated as ¼

the size of the monotonic yield zone assuming the compressive yield strength remains the same as the tensile yield strength. Applying a ¼ factor to the 5.47mm monotonic prediction results in a 1.37mm compressive yield zone. In reality, the compressive yield strength increases (becomes less negative) due to the Bauschinger effect which will slightly increases the size of the compressive yield zone. This is a possible explanation for the difference between the 2mm affected zone size shown in figure 2.10 and the 1.37mm zone size obtained from the analytical prediction.

2.6.3 Plastically Induced Closure

Another popular theory, plastically induced crack closure, is caused by an area of compressive residual stresses that follow in the wake of an advancing crack tip. Elber [35] studied crack closure effects resulting from constant amplitude tensile fatigue cycles. It was discovered that even during constant amplitude loading, the crack remained closed for a portion of the cycle. No crack growth is expected to occur while the crack is closed which led to Elber's definition of crack opening stresses and an effective stress concept [36]. The effective stress intensity factor accounts for plastically induced crack closure by reducing the driving force by the stress intensity needed to open the crack, as shown in equation 2.8.

$$\Delta K_{eff} = K_{max} - K_{op} \tag{2.8}$$

where ΔK_{eff} is the effective stress intensity factor and K_{op} is the stress intensity factor needed to open the crack. Using a crack closure approach, damage is assumed to occur only when the crack is open. Newman [37] worked extensively with the crack closure concept to further understand this complicated behavior. An analytical model

was created to predict variable amplitude load spectrums using Dugdale's strip yield plastic zone and incorporating the basics ideas of crack closure to more accurately predict load interaction effects.

2.6.4 Strain Hardening

Jones [38] showed that the level of pre-strain in titanium alloys influences the load interaction effects. Pre-strained alloys exhibited accelerated crack growth compared to a virgin material, especially at large ΔK. Strain hardened materials can actually increase the crack growth rate after applied overloads, contrary to the standard view of load interaction effects due to overloads. Once a material has been pre-strained, the amount of plastic strain before fracture decreases, causing energy to be absorbed by enhanced cracking rather than plastic deformation. Therefore, an overload cycle produces more crack growth for pre-strained materials rather than contributing to a large plastic zone. This result stresses the importance of deformation history as a consideration for influencing crack growth behavior.

2.6.5 Irregular Crack Front

Schijve [39] proposed that crack front irregularities can contribute to load interaction effects. The basis behind this argument lies in the relative amounts of plane stress and plane strain fracture during crack growth. Low ΔK cycles operate mainly under plane strain conditions and the fracture surface is relatively flat. However, high ΔK loading can create shear lips across the fracture surface, which is indicative of plane stress fracture. Schijve argued that the transition between mostly flat fracture and fracture with large amounts of shear lips could have relevance in variable amplitude crack growth.

However, it is difficult to validate crack front irregularities unless isolation of this specific mechanism can be achieved. A few years later, Schijve made a connection between the shear lip width and ΔK_{eff} for materials loaded in plane stress which bolstered the idea that crack closure is a relevant phenomenon [40].

Crack deviations have shown to reduce crack growth and in some cases, cause crack arrest. Boyd-Lee [41] studied fatigue resistance in nickel base superalloys and concluded that cracks which propagate along tortuous paths exhibit longer fatigue lives than cracks with lesser deviation from its nominal path. Obstructions such as grain boundaries and precipitates aid in deflecting cracks into positions that cause crack arrest. This theory has merit since cracks that deviate into positions perpendicular to the loading direction no longer have a driving force to cause crack extension. This effect can explain the non-uniform behavior of small cracks in high cycle fatigue loading.

Suresh [42] also studied the effect of micro-roughness on crack growth. It was argued that plastically induced crack closure is not the primary mechanism of retardation but crack tip branching occurs after an overload which reduces the effective stress intensity at the crack tip. Instead of pure mode one loading of a crack growing perpendicular to the loading direction, small deviations create a mixed mode condition, decreasing the driving force, and slowing the crack growth rate. These conclusions do not disprove the role of plastically induced crack retardation; however, it is suggested that the effect of plasticity is not the leading contributor for load interaction effects.

Suresh, Zamiski and Ritchie [43] devised an alternate explanation for crack closure through the concept of oxide induced crack closure. Corrosion or oxides can add to the

effect of crack closure by forming on the surfaces of a propagating crack. Suresh et al. showed that this build up of oxide debris contributes to crack closure effects and reduces the driving force at the crack tip. This effect was seen on steel specimens tested in moist air and dry hydrogen environments at near threshold loading conditions.

2.6.6 Hybrid Theories

Skorupa referenced many authors who have reexamined the stresses ahead of the crack tip and revised Elber's crack closure theory by assuming that crack growth does not occur if the zone ahead of the crack is in compression [31]. This has lead to revised theories on crack propagation. Toyosada and Niwa [44] assumed that damage does not occur until sufficient stress is available to cause slip ahead of the crack. They proposed a modified driving force that not only account for crack closure but also included the linear elastic portion of the loading cycle. In contrast to Elber's effective stress intensity concept, their stress intensity parameter considers the re-tensile plastic zone, which appears during the loading cycle. The plastic work generated by the continuous reloading of the plastic zone creates damage, which leads to crack growth. Toyosada et al. demonstrated that using the re-tensile plastic zone as a measure for the stress intensity factor led to a linear relationship between stress intensity and crack growth rates in both stage one and stage two crack growth when plotted on a log-log plot.

More recent studies have examined the crack tip cyclic stress-strain field to better characterize crack tip conditions. Modern techniques have allowed the measurement of stress-strain hysteresis loops near the crack tip during propagation. These loops have provided valuable insight into explaining the effects of crack closure. Xiong, Katsuta, Kawano, and Sakiyama [45] studied the hysteresis loops of a fatigue crack subjected to

constant amplitude and spike overload cycles. They were able to relate the morphology of the hysteresis loop to crack closure concepts and better explain acceleration and delayed retardation phenomenon. Xiong et al. [46] later developed a new parameter, ΔK_{drive}, to describe crack tip conditions based on hysteresis curves.

A unified approach is proposed by Sadananda, Vasudevan, Holtz, and Lee [47] to remove some of the ambiguity between the actual phenomenon causing load interaction effects. Their two-parameter approach uses both K_{max} and ΔK as the controlling factors influencing crack growth, contrary to the crack closure theory which only accounts for changes to the stress range. Sadananda et al. minimized the role of crack closure by explaining the manifestations of crack closure through their unified approach. The role of K_{max} was shown to be more significant than ΔK, an indication that yielding ahead of the crack tip could be more important than the compressive zone in the wake of a crack.

The number of different techniques to describe load interaction effects is diverse and no single technique has proven to be superior to the rest. It almost seems like every theory has evidence that supports and contradicts its occurrence, leading to a lack of standard agreement between experts on this subject. This research area continues to grow with the increasing demand to predict structural life under complex spectrums accurately. This leaves the door open for the discovery of an ideal model that correctly captures the physics behind crack propagation and is widely accepted in the engineering community.

2.7 Dynamic Strain Ageing

Dynamic strain ageing as defined by Robinson and Shaw [48] is “the attractive interactions between diffusing solute species in an alloy and mobile dislocations.” Dislocation ageing occurs when dislocation are made immobile by defects in the crystal structure. Mobile solute atoms will congregate to the dislocation while it is locked by a defect and the rate of solute congregation depends on temperature, strain, and strain rate. All of these factors can contribute to serrated or “jerky” flow referred to as the Portevin-Le Chatelier (PLC) effect.

2.7.1 Portevin - Le Chatelier Effect

There are many ways to define the conditions in which the PLC effect is likely to occur. Rodriguez [49] has observed trends of five temperature dependent mechanical properties that indicate the presence of serrated flow, figure 2.11. These five trends are:

- Negative strain rate sensitivity
- Variation in flow stress with temperature
- Variation in work hardening rate with temperature
- Variation in Hall-Petch slope with temperature
- Minimum of elongation with temperature

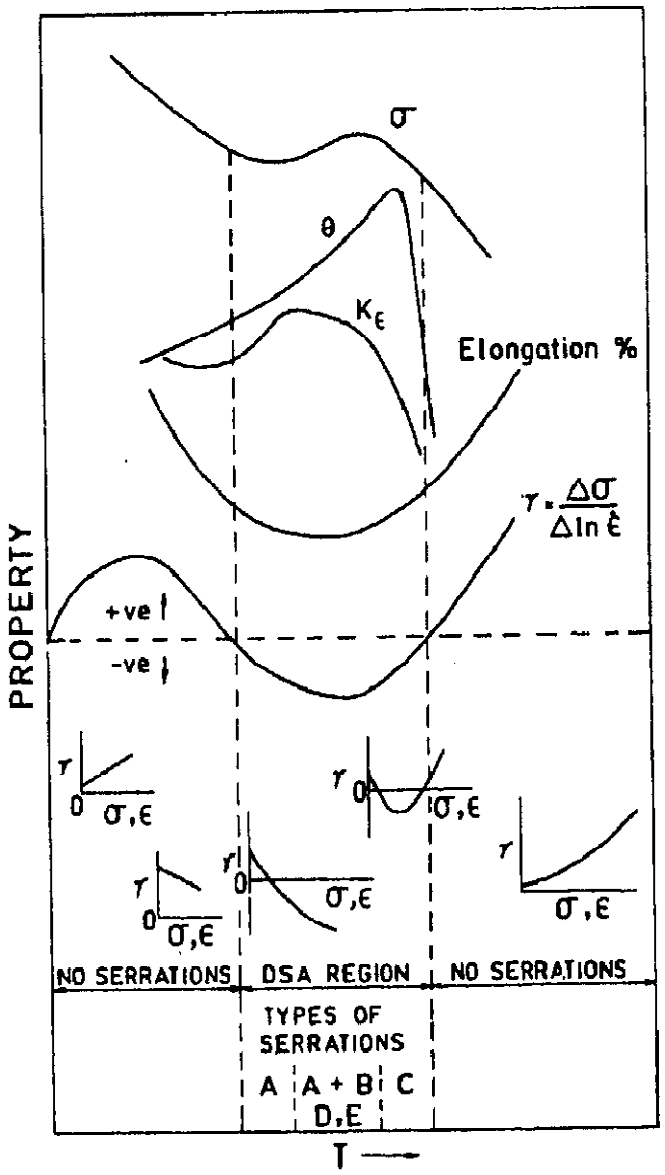

Figure 2.11 - Indications of Conditions Resulting from Dynamic Strain Ageing [49]

The strain rate sensitivity parameter is the most widely used method to explain the conditions needed for serrated plastic flow. The strain rate sensitivity parameter is defined by equation 2.9 which leads to equation 2.10 where σ_1 is the stress corresponding to $\dot{\varepsilon}_1$ and σ_2 is the stress corresponding to $\dot{\varepsilon}_2$, all evaluated at a constant

strain and temperature. Materials that exhibit a decrease in flow stress with an increase in strain rate will have a negative strain rate sensitivity parameter, m.

$$\sigma = C\dot{\varepsilon}^m \tag{2.9}$$

$$m = \frac{\ln\left(\frac{\sigma_2}{\sigma_1}\right)}{\ln\left(\frac{\dot{\varepsilon}_2}{\dot{\varepsilon}_1}\right)} \tag{2.10}$$

Stanford, Sabirov, Sha, La Fontaine, Ringer, and Barnett [50] studied the strain rate sensitivity parameter in magnesium alloys with aluminum and gadolinium solutes. Strain rate jump tests were performed to identify conditions that created a negative strain rate sensitivity parameter. These relatively simple, yet revealing, tests showed a drop in flow stress when the strain rate was increased during the test. Tests conditions that created a decrease in flow stress with increasing strain rate also exhibited serrated plastic flow characteristics.

Atom probe tomography was used to further analyze the PLC effect in the magnesium alloys [50]. Samples were taken from specimens that exhibited serrated flow and it was shown that gadolinium atoms had doubled in concentration around the dislocations while the aluminum solutes did not congregate to the dislocation. This result supports the theory that mobile solute atoms are the primary cause of serrated flow.

The type of serration has been classified by many authors [51-53] and a schematic is shown in figure 2.12. The deformation behavior as shown on a stress vs. strain plot can be divided into five categories: A, B, C, D, and E.

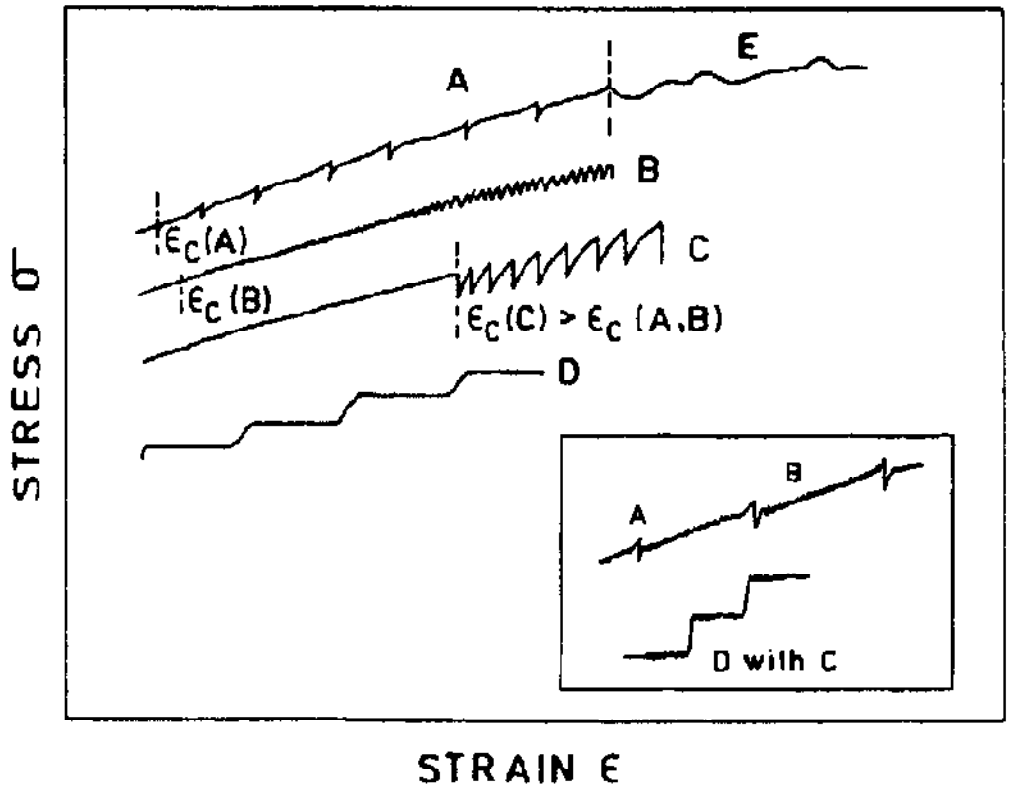

Figure 2.12 - Type of Serrations [49]

Type A serrations are caused by the continuous propagation of deformation bands across the entire width of the specimen. The loads drops are relatively infrequent but continuous. These serrations are considered “locking” serrations in which solute atoms have locked the dislocation from moving until sufficient energy is provided to unlock the dislocation. Type A serrations usually occur at low temperatures or high strain rates [49] so the relative motion between the dislocation and solute atom is maximized. At high strains, type A serrations can turn into type E serrations. Type B serrations occur by the hopping of propagation bands which do not extend across the entire specimen [54]. Oscillation in the stress-strain curve occurs at a general stress level in quick succession [49]. In many cases type A and B serrations appear together [52], especially at higher temperatures. Type C serrations occur below the general stress level due to dislocation

unlocking at higher temperatures than types A and B. Type D serrations exhibit stress plateaus and occur when no work hardening is present [49].

Flow oscillations were studied by Prasad, Sarkar, Ghosal, and Kumar [55] in IN718 at 650°C at various strain rates. Twining was apparent in each of the tests; however, evidence of serrated yielding due to the PLC effect was also apparent at certain strain rates. TEM micrographs illustrated the inhomogeneous nature of dynamic strain ageing by localizing deformation between slip bands. Strain localization is a large reason why the PLC effect is difficult to measure and hard to predict.

Hayes [56] studied the PLC behavior in Waspalloy and compared two different methods to determine the activation energy needed to trigger the thermally activated mechanism needed to lock dislocations in a solute atmosphere. The critical strain method provides a relatively simple way to determine the activation energy using the strain at the onset of serrated flow. The stress decrement method relates the amplitude of serrations to the strain rate to obtain the activation energy. Dislocation arrest time increases as strain increases which provides more time for carbon segregation to the dislocation, causing larger stress drops at higher strains. Hayes concluded that the stress decrement method gave a better approximation of the activation energy for more complex alloys and removed the anomalies associated with the critical strain method.

Hayes and Hayes [57] also discussed the role of carbon pipe diffusion down a dislocation as a possible explanation for the transition between smooth and serrated flow. A carbon atmosphere attaches itself to a moving dislocation, which is eventually arrested at a precipitate. During the arrest time, more carbon atoms congregate to the

dislocation which, given sufficient energy, eventually bows around the precipitate. Carbon is drained from the dislocation into the precipitate and the flow is smooth since the carbon atmosphere is no longer attached. Evidence to support this theory is seen when varying temperature and strain rate. Increasing temperature and decreasing strain rate will usually increase the critical strain for the onset of serrated flow because either faster carbon draining occurs at higher temperatures or more time is available for carbon diffusion at slower strain rates.

Limited research has been done on the effects of PLC behavior on fatigue life. However, Seong-Gu Hong and Soon-Bok Lee [58] performed low cycle fatigue tests on stainless steel specimens at various strain rates and temperatures. The tests that exhibited serrated yielding also had a significant reduction of the crack initiation and propagation lives. It was concluded that inhomogeneous deformation resulted in multiple crack initiation sites and led to more damage than specimens that did not exhibit serrated yielding. This important conclusion suggests that dynamic strain ageing effects should be considered in materials that are deformed at conditions conducive to serrated plastic flow. These conditions can possibly occur within the plastic zone at a crack tip, which can lead to shorter crack propagation lives.

CHAPTER 3: MATERIALS AND TESTING EQUIPMENT

Superalloys have proven to be a versatile and well-suited material for high temperature applications. As such, many variations and significant differences exist depending on the technology at the time of development and the application for which they were designed. Understanding these differences is vitally important in the calibration and verification of any predictive model; therefore, significant research was performed in order to understand specific material characteristics that might influence modeling results. In addition, adequate testing equipment was selected in order to capture the desired material behavior effectively.

3.1 General Inconel 100

Inconel 100 (IN-100) is a polycrystalline nickel based superalloy with a fine-grained structure. The IN-100 alloy used in this research was processed using powdered metallurgy techniques and is classified as a wrought alloy; however, some forms of IN-100 can be manufactured in the cast form [7]. Each of these manufacturing techniques produces different microstructures and varying properties. This makes it essential to know the processing techniques when viewing published data on this alloy. The nominal composition of IN-100 in cast, wrought, and P/M forms is given in table 3.1.

Table 3.1 - IN-100 Composition in Various Forms [7]

Form	IN-100 Composition (%)										
	Ni	**Co**	**Cr**	**Al**	**Ti**	**Mo**	**V**	**Fe**	**C**	**Zr**	**B**
Cast	60.5	15.0	10.0	5.5	5.0	3.0	1.0	--	0.18	0.06	0.01
Wrought	60.0	15.0	10.0	5.5	4.7	3.0	1.0	<0.6	0.15	0.06	0.02
P/M	55.6	18.5	12.5	5.0	4.3	3.2	0.75	--	0.07	0.04	0.02

The composition does not change dramatically between the different processing forms; however, small changes in composition can result in large differences in alloy properties. The powdered metallurgy (P/M) form has lower nickel content and higher cobalt and chromium additions. Cobalt is used to enhance creep rupture life by increasing the volume fraction of secondary precipitates and chromium is added to improve oxidation resistance [7]. Since P/M alloys have a finer grain structure than cast alloys, an improvement in high temperature properties is needed to offset the increased amount of exposed grain boundaries.

Published values of mechanical properties are shown in table 3.2 and physical properties of cast IN-100 are given in table 3.3. A trend characteristic of many superalloys is the increase in yield strength with temperature followed by a drastic decrease in strength as temperature increases further. This trend is evident in data presented in table 3.2. The physical properties shown in table 3.3 are not expected to vary dramatically between cast, wrought, and P/M forms. The density of cast IN-100 is roughly the same as mild steel, which is ironic considering most aerospace structures are designed to minimize weight. The high temperature requirements of turbine components negate the benefits of using lighter, less capable materials.

Table 3.2 - Mechanical Properties of P/M IN-100 [7]

	25℃	649℃	704℃
0.2% Yield Strength (MPa)	940	1080	1065
Ultimate Tensile Strength (MPa)	1130	1290	1270
Elongation (%)	8	16	20

Table 3.3 - Physical Properties of Cast IN-100 [7]

	Density	**Melting Range**	**Specific Heat (J/kg·K)**		**Thermal Conductivity (W/m·K)**	**Mean Coefficient of Thermal Expansion (10^{-6} K)**		
	g/cm^3	**℃**	**538℃**	**1093℃**	**538℃**	**93℃**	**538℃**	**1093℃**
Cast IN-100	7.75	1265-1335	480	605	17.3	13.0	13.9	18.1

IN-100 has a grain size around 3-5 microns. It was originally used as turbine blade materials in the 1960's; however, the increasing temperature limits of turbine blades forced the development of higher temperature materials. The fine-grained nature of this alloy made it susceptible to environmental attack at high temperature. IN-100 is now used as compressor and turbine disk materials, which operate at lower temperatures than blade materials.

3.1.1 Powder Metallurgy

Powder metallurgy is a processing technique used to improve mechanical properties compared to cast or wrought processing. It generally requires fewer steps to

manufacture a P/M component; however, the costs are usually higher because the process is complex and the environmental conditions must be strictly maintained to avoid alloy contamination.

The powder is formed through soluble gas atomization. Molten alloy with the correct chemical composition is injected with a soluble gas and forced at high pressures into a vacuum. The rapid expansion causes the molten metal to solidify as fine droplets which fall into a collection chamber [7]. This process must be strictly controlled in an inert environment since the fine powder can easily attain harmful oxygen and nitrogen atoms by being exposed to air.

After the powder has been formed, it must be consolidated into a useable form. This process is usually done by hot isostatic pressing (HIP). Powder fills stainless steel containers that are preheated and purged of oxygen. High pressures and temperatures are applied to the containers, which consolidates the powder into a solid form. Grain size can be controlled by varying the HIP temperature during this process [7]. These containers usually resemble a near-net shape to minimize the post processed machining.

3.1.2 Microstructure

Superalloy microstructure varies depending on the composition and processing technique. Reed describes three guidelines which materials engineers need to consider when developing a disk alloy [59].

- The γ' precipitates must be uniformly distributed with a volume fraction between 40-55%.
- The factors dictating grain size should include yield strength, crack initiation and propagation life, and creep strength. Common grain sizes range from 30-50 μm.
- The use of carbon and boron elements at the grain boundary can be used to increase creep and crack initiation resistance.

The γ' phase is the most important strengthening addition to a superalloy and is created by the alloying additions of aluminum, titanium, and niobium [59]. Precipitation can be controlled by specific heat treatments and thus the γ' phase can be engineering to the desirable size and distribution. Slight additions of boron and carbon are beneficial to the cohesion strength at the γ/γ' interface, leading to improvements in creep rupture strength, creep ductility, and low cycle fatigue behavior [59].

Grain size is another important consideration. Fine grained structures exhibit good strength and low cycle fatigue life at the expense of creep properties and crack propagation rates [59]. A compromise between these factors must be reached to maximize the overall benefit as shown by several researchers [60]. Figure 3.1 shows a typical microstructure from a P/M superalloy. The γ matrix embedded with evenly distributed spherical γ' particles is shown in figure 3.1a. The shape of the γ' particles are influenced by the ageing time during processing [61]. A higher magnification image, figure 3.1b, shows the secondary γ' particles within the matrix. In some cases, the secondary γ' precipitates are more uniform than the larger, primary γ' precipitates and can possibly be the main strengthening source in the alloy.

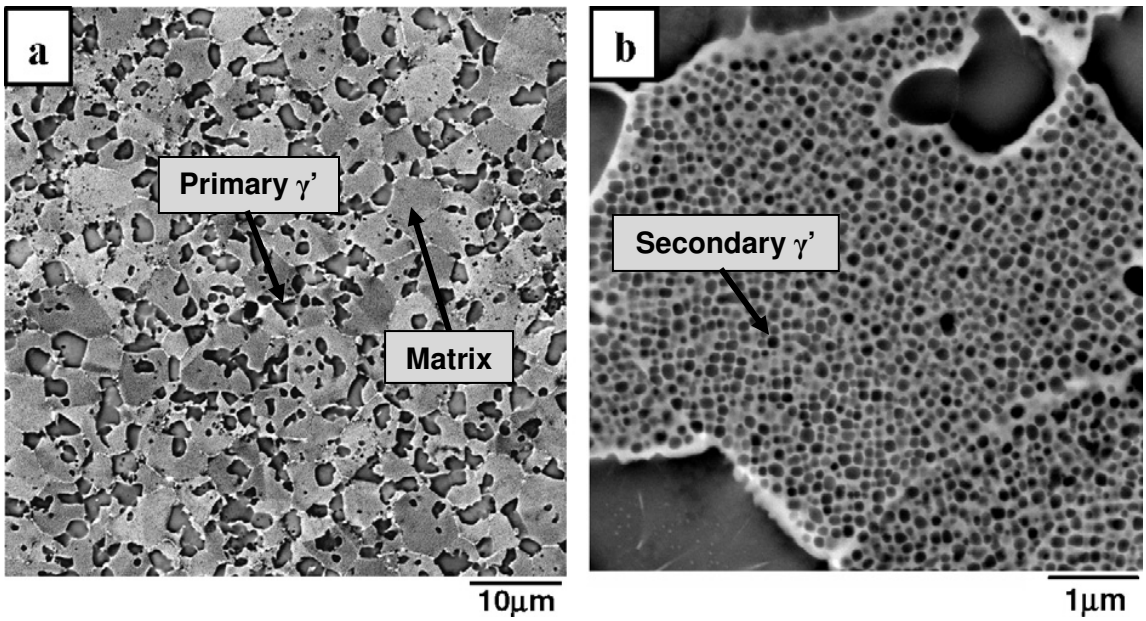

Figure 3.1 - Microstructure from a General P/M Superalloy [62].

3.3 IN-100 Disk Material

A turbine disk was supplied by Pratt and Whitney for the use of obtaining test specimens from an "as processed" material. Ideally, laboratory specimens manufactured for small scale testing should have the same properties as the final structure. However, creating a perfectly homogeneous material with complex geometries and thick cross sections is a difficult task. Testing material cut from a turbine disk removes any discrepancies between specimens manufactured for laboratory tests and the actual product. The turbine disk used for specimen generation is shown in figure 3.2 and its composition is listed in table 3.4.

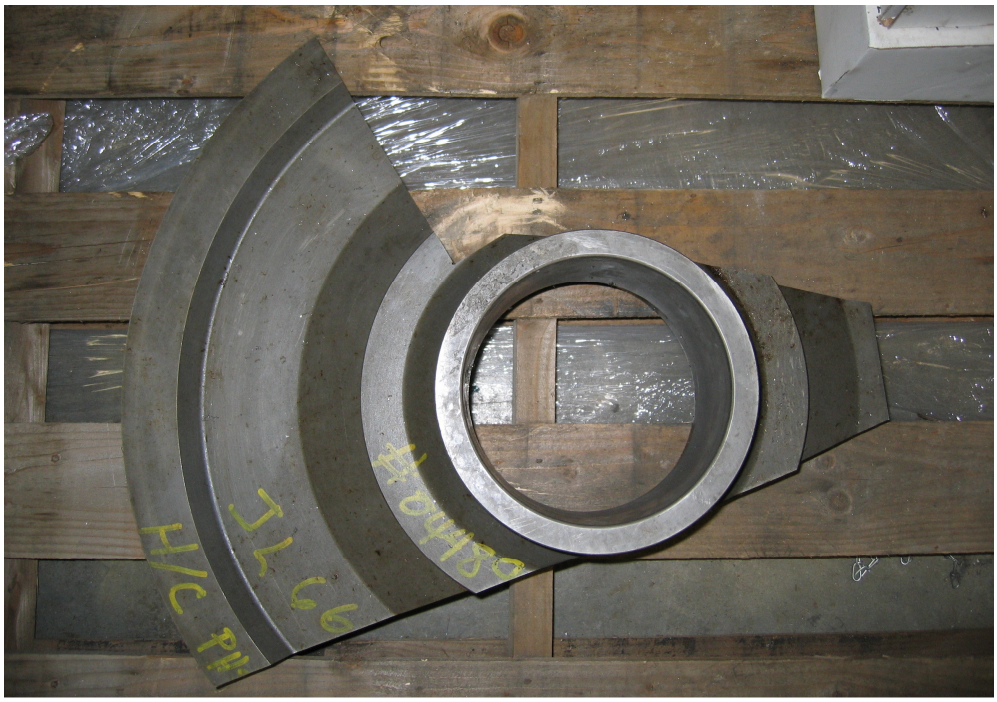

Figure 3.2 - IN-100 Turbine Blade Disk from which Specimens were Obtained

Table 3.4 - Composition of Supplied IN-100 Disk Material

	IN-100 Composition (%)										
	Ni	**Co**	**Cr**	**Al**	**Ti**	**Mo**	**V**	**Fe**	**C**	**Zr**	**B**
IN-100 Disk	56.5	18.2	12.1	4.9	4.22	3.22	0.7	--	0.07	0.07	0.02

The heat treatment for this disk material occurred in a three step process in order to obtain a homogenous grain size and precipitate density. The first step was a 2090°F firing followed by an oil quench. Secondly, the disk was reheated to 1800°F for one hour, and then underwent forced air cooling. Lastly, an eight hour, 1350°F annealing process was performed after which the disk was left to cool at room temperature. This process produced an average grain size of 3-5 microns and a 36% precipitate volume fraction as shown in figure 3.3.

a)

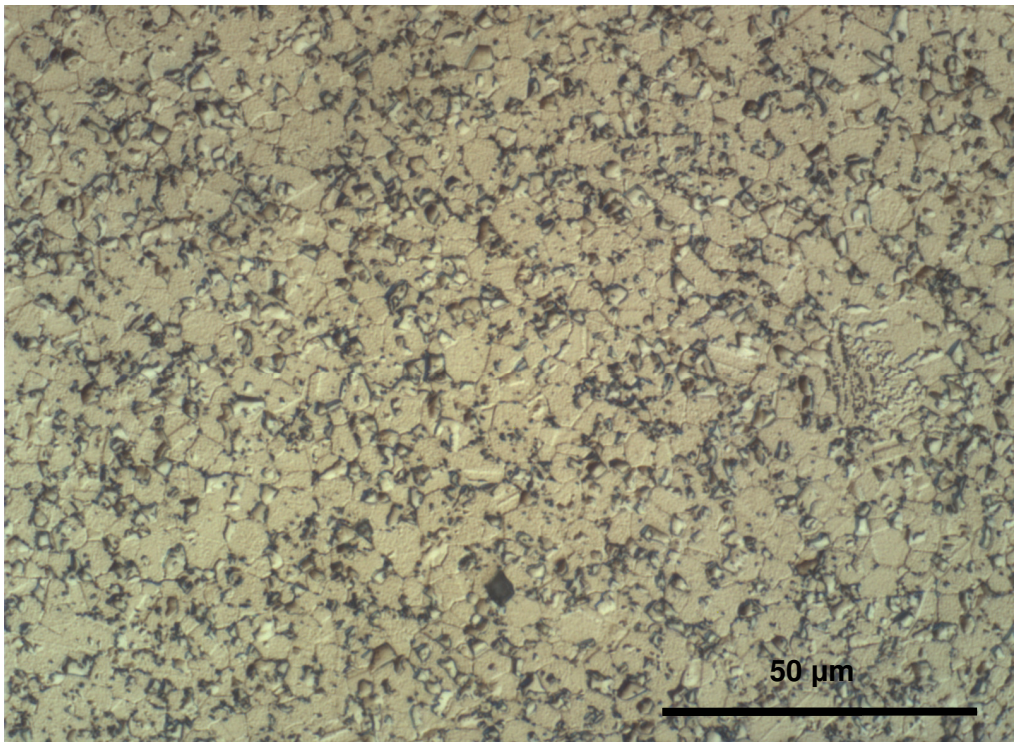

b)

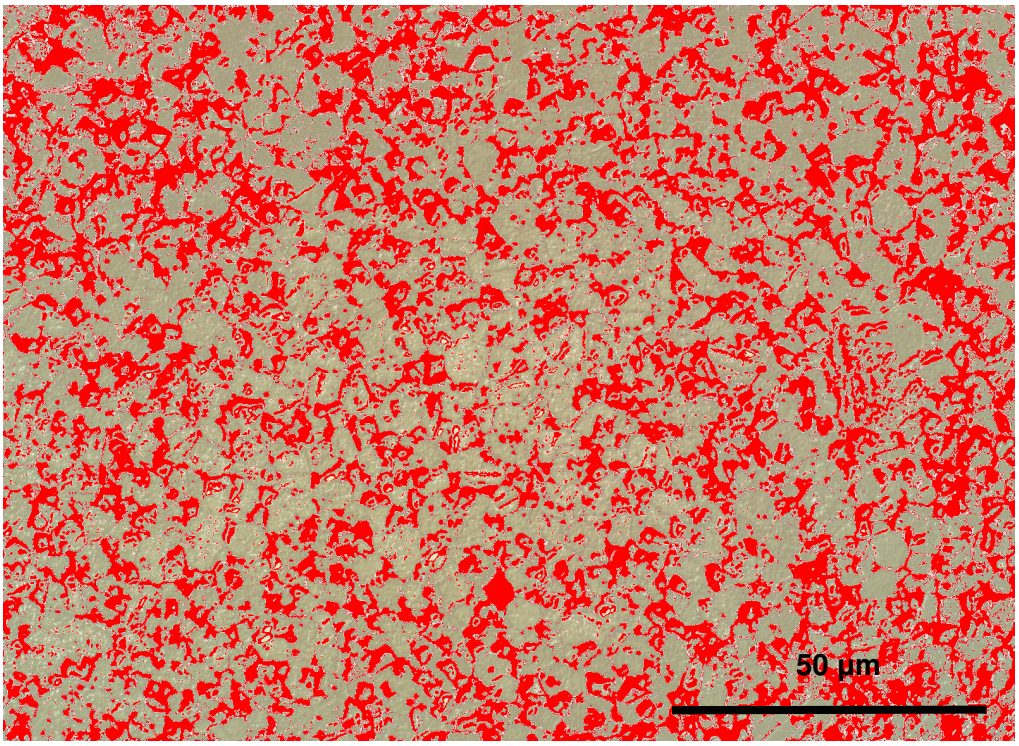

Figure 3.3 - a) Optical Microscope Image of IN-100 Microstructure; b) Precipitates Highlighted in Red to Determine Volume Fraction

Scanning Electron Microscopy (SEM) was also used to help characterize this specific microstructure of the IN-100 disk alloy. Higher magnification images show a clear distinction of the grain size as well as the γ'' particles within the γ matrix as shown in figure 3.4.

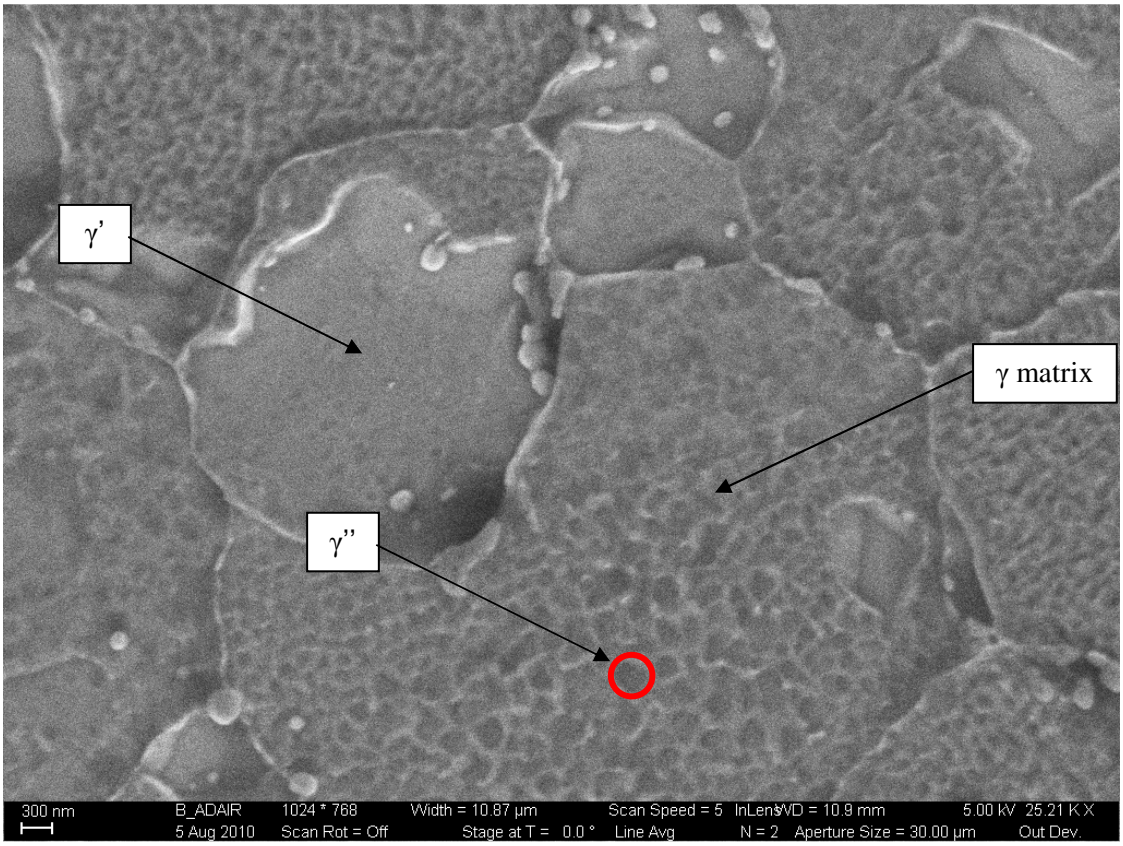

Figure 3.4 - SEM image of IN-100 Microstructure [63]

SEM analysis offers the ability to study the IN-100 microstructure at high magnifications that are unattainable with optical microscopy. The secondary γ' particles are visible in figure 3.4 and have a sponge-like appearance within the γ matrix. It is believed that the smaller secondary γ' particles are responsible for giving this alloys its high temperature strength. Grain boundaries are also clearly visible in figure 3.4 and contain spherical particles, which are most likely carbides or borides. These particles can contribute to

favorable high temperature properties such as increasing the creep rupture strength if available in small amounts [7].

3.4 Testing Equipment and Specimen Geometry

High temperature tensile testing requires many hardware and software components to work in unison in order to obtain useful and repeatable data. Many options are available to customize the test setup to fit the needs of each individual test. Table 3.5 lists all the components used for the IN-100 tensile testing.

Table 3.5 - List of Equipment and Instrumentation Used for Testing

Component	Manufacturer	Model Number	Notes
Load Frame	SATEC	Uniframe TC25	N/A
Load Cell	MTS	661.20E-03	98 kN Capacity
Hydraulic Wedge Grips	MTS	647	20.6 MPa Grip Pressure Capacity
Induction Heater	Cycle Dyne	A-30	3 kW output
Control Software	MTS	TestStar IIs	N/A
Extensometer	Epsilon	3448-0100-010	25.4 mm Gage Length; ±10% range

Induction heating was employed because it can quickly heat a specimen to very high temperatures. This method is ideal for TMF testing because heating and cooling must be done quickly in order to mimic real world turbine engine conditions. The drawback to induction heating is the intricate coil design that must be modified to fit the high temperature extensometer rods. Several coil design iterations were needed in order to

find one that had enough tolerance for the extensometer rods but also provided a uniform heat distribution across the specimen's gage section. Figure 3.5 shows the coil design used for the IN-100 testing.

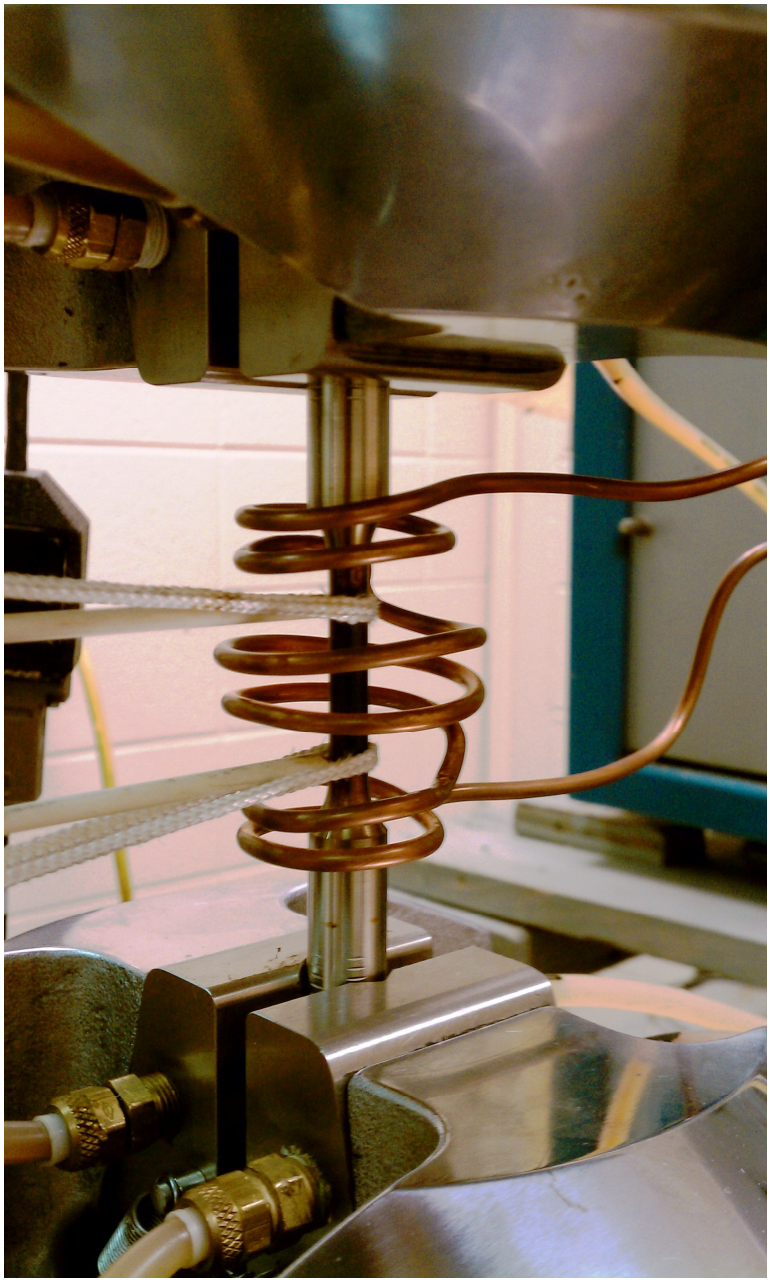

Figure 3.5 - Test Setup Including Induction Heater Coil and Extensometer Attached to Specimen

Water-cooled, hydraulic wedge grips were used due to their ability to whisk away heat from a cooling specimen quickly. Flow regulator valves adjusted the amount of water flowing into the grips and were another means of controlling the temperature distribution along the specimen's gage section. In addition to temperature control, the specimen tolerances for round wedge grips are not as tight as for collet grips. For hard materials, the grip diameter must be within a tolerance of 0.002" to ensure that the specimen will not slip in the grips. Using wedge grips decreased the change for grip slippage of undersized specimens and allows for larger tolerances in specimen dimensions. Figure 3.6 shows the wedge grips used in the experimental set-up.

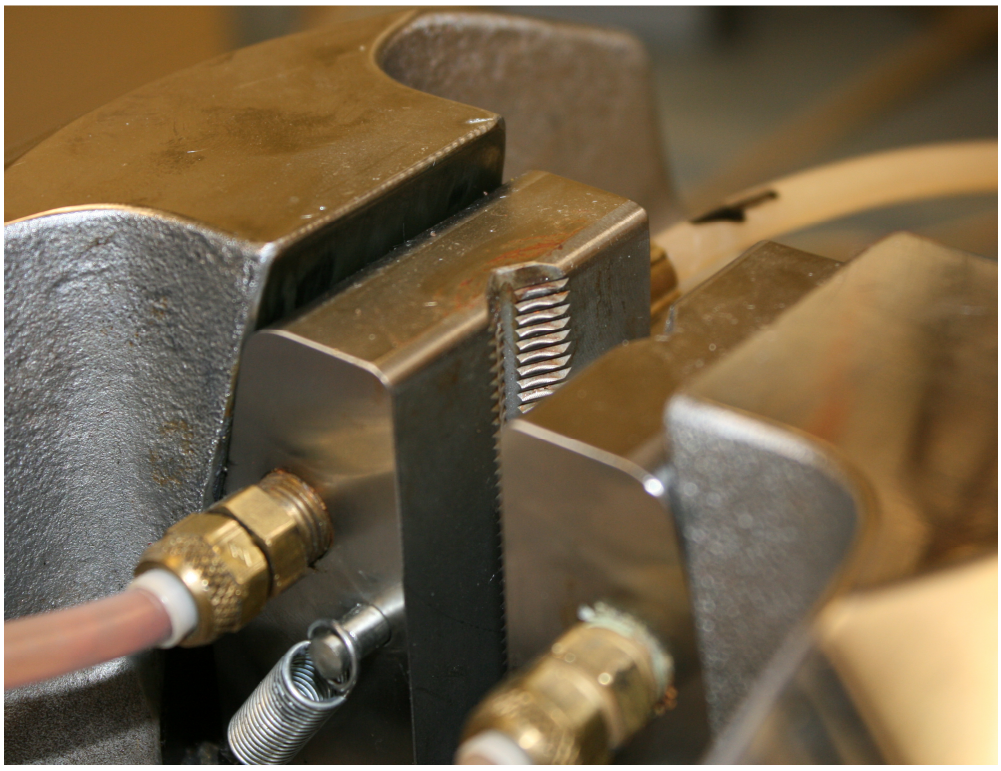

Figure 3.6 - Hydraulic Wedge Grips used in High Temperature Tests

The grooves within the wedges deform the specimen in the grip section to ensure a tight grip. The grip pressure was set to 9.6 MPa to provide adequate grip pressure while minimizing the deformation in the grip section.

Specimens were machined by MAR-TEST and included threaded connections, as shown in figure 3.7.

Figure 3.7 - Specimen Used for High Temperature Tensile Tests

The grip diameter was 12.700 mm, gage diameter 6.325 mm with a gage length of 31.750 mm. The threaded connections were not utilized since the specimen was secured in the machine by wedge grips.

Tensile tests were conducted in stroke control based upon the actuator's displacement. Flow instabilities under specific test conditions made it difficult to control the specimen's strain rate. This phenomenon is related to the Portevin-Le Chatelier effect, which results in serrated yielding at certain temperature and strain rate combinations. To alleviate any potential oscillations in the control mode, tests were conducted under displacement control while measuring strain.

CHAPTER 4: TESTING RESULTS AND DISCUSSION

Modeling must be validated by rigorous testing in order to ensure confidence that the model is correctly predicting the desired phenomenon. Without verification, modeling results are subject to interpretation and could be grossly inaccurate. Testing confirms predictions within the bounds of the model and increases the certainty outside of those bounds.

Several tests were conducted to validate the crack growth model discussed in the previous chapter. These tests fall under two categories:

- High temperature yield strength testing
- Cyclic yielding/changing temperature testing

The application between testing results and modeling inputs will also be discussed.

4.1 High Temperature Tensile Tests

High temperature yield strength values are very important inputs into a load interaction yield zone model. Material strength is temperature dependent, even for high strength Ni-base superalloys. In addition, the size of the plastic zone ahead of a crack tip is strongly depended on the yield stress. Therefore, changing temperature influences the yield strength, which influences the plastic zone size. Load interaction effects are subsequently affected by changing temperature during crack growth.

Cylindrical IN-100 specimens were tested in stroke control to determine high temperature yield strength values as well as hardening coefficients to further characterize this material. Table 4.1 shows the testing rates for these tests.

Table 4.1 - Test Conditions for High Temperature IN-100 Tensile Tests

Test Number	Temperature (°C)	Displacement Rate (*10^{-5} m/s)	Elastic Strain Rate (*10^{-5}/s)	Plastic Strain Rate (*10^{-5}/s)
1	315	0.4	2	8
2	315	30.2	207	594
3	482	0.3	2	7
4	482	33.5	238	685
5	649	0.4	2	10
6	649	35.8	249	824

Two strain rates and three temperatures led to six total tests. Stroke control was chosen because of instabilities that existed during plastic flow. Interactions between diffusing solute atoms and mobile dislocations created serrated flow, which caused difficulty in controlling a constant strain rate. As a result, displacement rates were chosen to provide a similar elastic strain rate at each temperature. Figure 4.1 shows the stress vs. strain graph for all six tests.

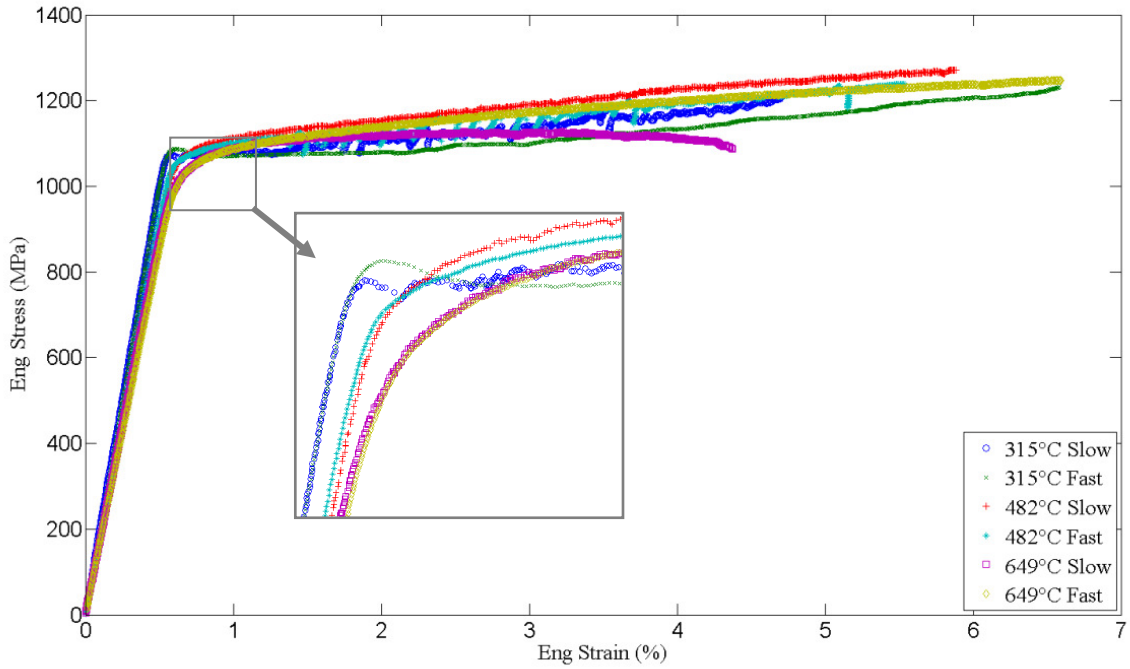

Figure 4.1 - Overall Stress vs. Strain Response for All Temperatures and Strain Rates

The maximum strain for these tests was approximately 6%. The total elongation was limited by the range of the extensometer and the amount of space available between the coils used for induction heating. However, enough plastic strain is present in order to compare rate and temperature effects on the plastic behavior of IN-100.

Fracture occurred on the 649℃ slow rate test at the location of the thermocouple. This was an unexpected result since the total elongation of IN-100 is expected to be around 16% [7]. The probable cause of premature failure could have been a result of initial damage induced by the thermocouple weld since failure propagated from this location.

4.1.1 Yield Strength Determination

Overall, increasing temperature decreased the yield strength and strain rate had a marginal effect on the magnitude of the yield stress. Figure 4.2 shows the 0.02% offset yield strength as a function of temperature for all six high temperature tests.

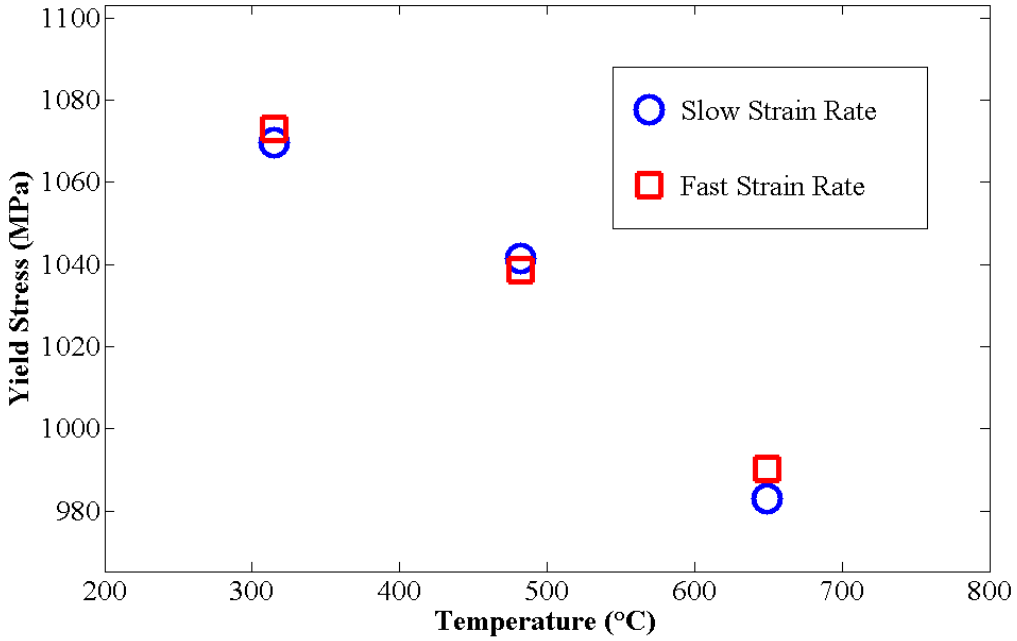

Figure 4.2 - IN-100 Yield Strength as a Function of Temperature with a 0.02% Offset

Increasing temperature decreases the yield stress of IN-100. This trend is common to most metals since the higher temperatures increase the atomic vibration frequency and increases the probability that atoms will break bonds and dislocation can slip at a lower amount of mechanical energy. However, an important characteristic of superalloys is their ability to maintain their strength at high temepratures. This discrepancy exists due to the methods used to define the yield strength.

A significant, and sometimes overlooked, variable in determining yield strength is the amount of strain offset used to determine the yield stress. The most widely used offset published in literature is 0.2% strain. This relatively large offset ensures that global yielding has occurred across the entire specimen. However, using such a large offset includes hardening effects, which may skew the data trends. For example, figure 4.3 shows the yield strength dependency on temperature with an added 0.2% offset.

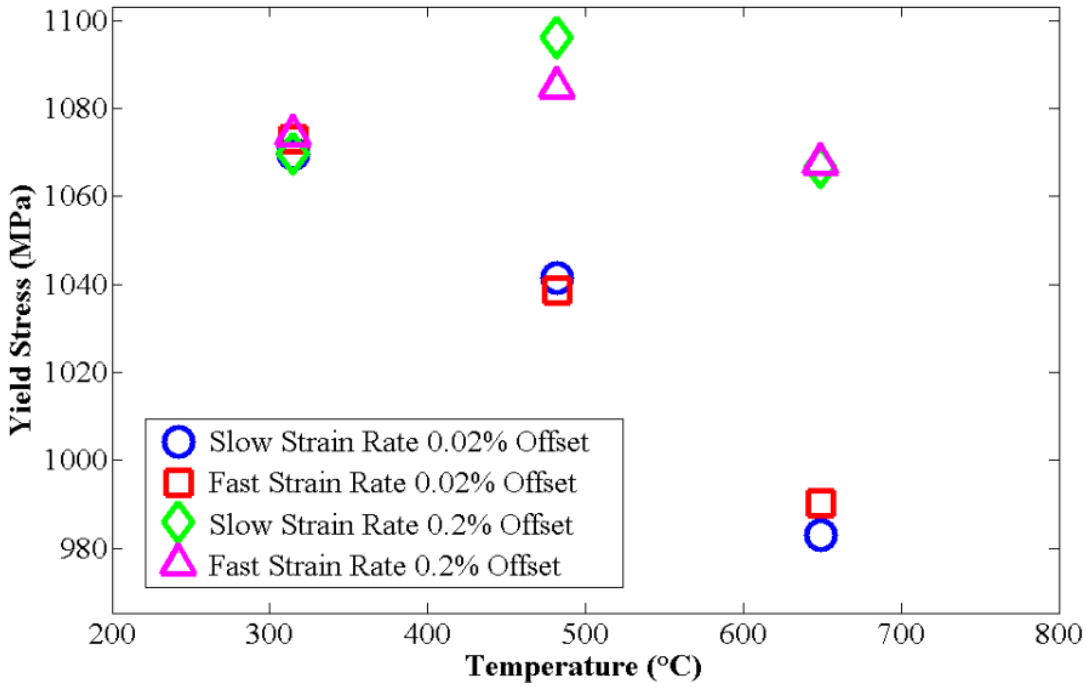

Figure 4.3 - Yield Strength Dependence on Temperature with 0.02% and 0.2% Offsets

The 0.2% offset exhibits higher yield strengths and a lower temperature dependence as compared to the 0.02% offset. It also matches closer to currently published data [7]. This difference in yield stress is attributed to the different hardening behavior at different temperatures. The 315℃ specimens had a well-defined local maximum and relatively little hardening immediately after yield, leading to small changes in the yield strength

between the 0.2% and 0.02% offsets. On the other hand, the higher temperature tests did not have a local maximum and a smooth transition occurred from the elastic to plastic regimes, resulting in larger changes in the yield strength as a function of strain offset.

This discrepancy leads to the question: What offset should be used in analysis? The answer depends on the application for which it is used. In the case of crack growth, small scale yielding occurs over a few grains, resulting in a relatively small amount of yielding. Favorable grain orientations are more likely to yield first, at the lower end of the yield strength spectrum. In addition, cracks grow along the path of least resistance, increasing the probability that the affected plastic zone will consist of grains oriented in favorable directions. This results leads to the conclusion that a small, 0.02% strain offset should be used in crack growth analysis.

4.1.2 Influence of Strain Rate and Temperature

Rate dependent characteristics are assessed by plotting the individual temperature tests on the same plot as shown in figure 4.4.

a)

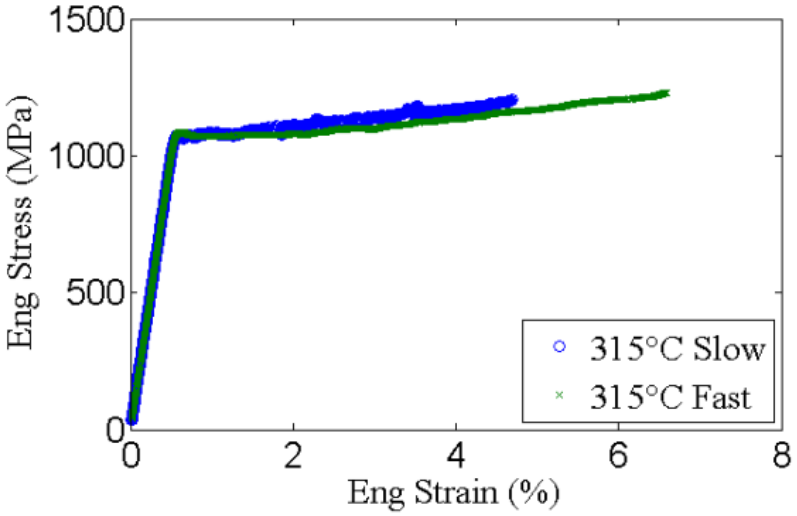

b)

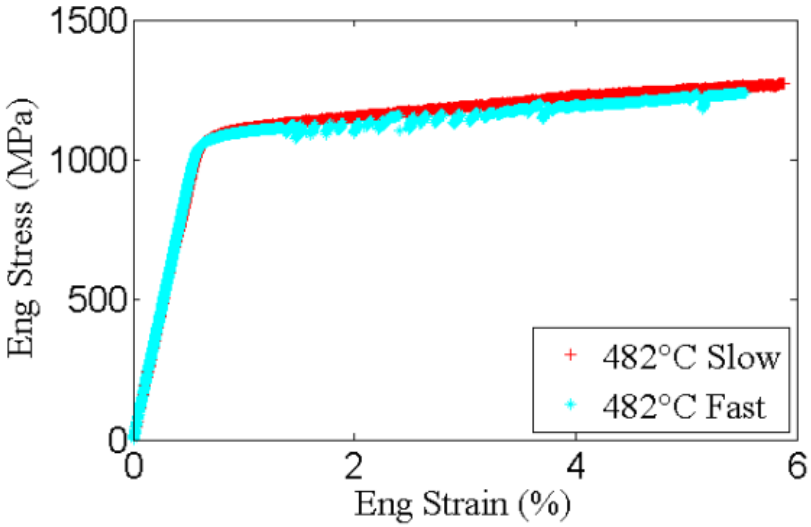

c)

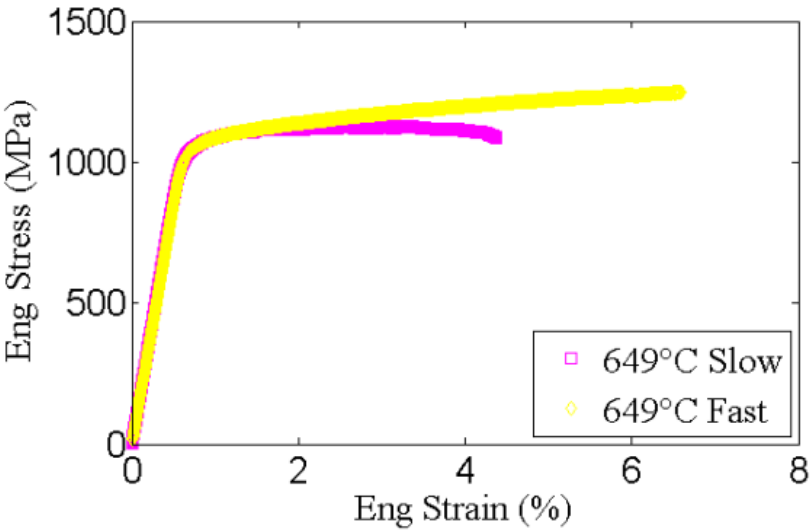

Figure 4.4 a-c - Individual Temperature Results Showing Rate Characteristics: a) 315℃, b) 482℃, c) 649℃

As stated previously in table 4.1, the “slow” strain rate corresponds to an elastic strain rate around $2.5x10^{-5}$ s^{-1} and the “fast” strain rate corresponds to an elastic strain rate around $2.5x10^{-3}$ s^{-1}. For the 315°C and 482°C tests, the slow strain rate had slightly more overall hardening effect than the fast strain rate. The 649°C tests show increasing hardening with increasing strain rate. At this temperature, creep plays an important role in the apparent hardening behavior. Creep strain accumulation is more apparent on the slower tests since the specimen is at a high temperature for a longer time, reducing the overall hardening effect as seen on the stress vs. strain curve. Visual comparison can be misleading because it includes transitional effects between the elastic and plastic regimes. Some specimens exhibit perfectly plastic flow for a small portion of plastic strain while other specimens gradually harden after yielding. This creates difficultly when trying to compare hardening rates between specimens optically.

A more detailed view of IN-100 high temperature hardening characteristics can be shown by plotting true stress vs. true plastic strain, figure 4.5.

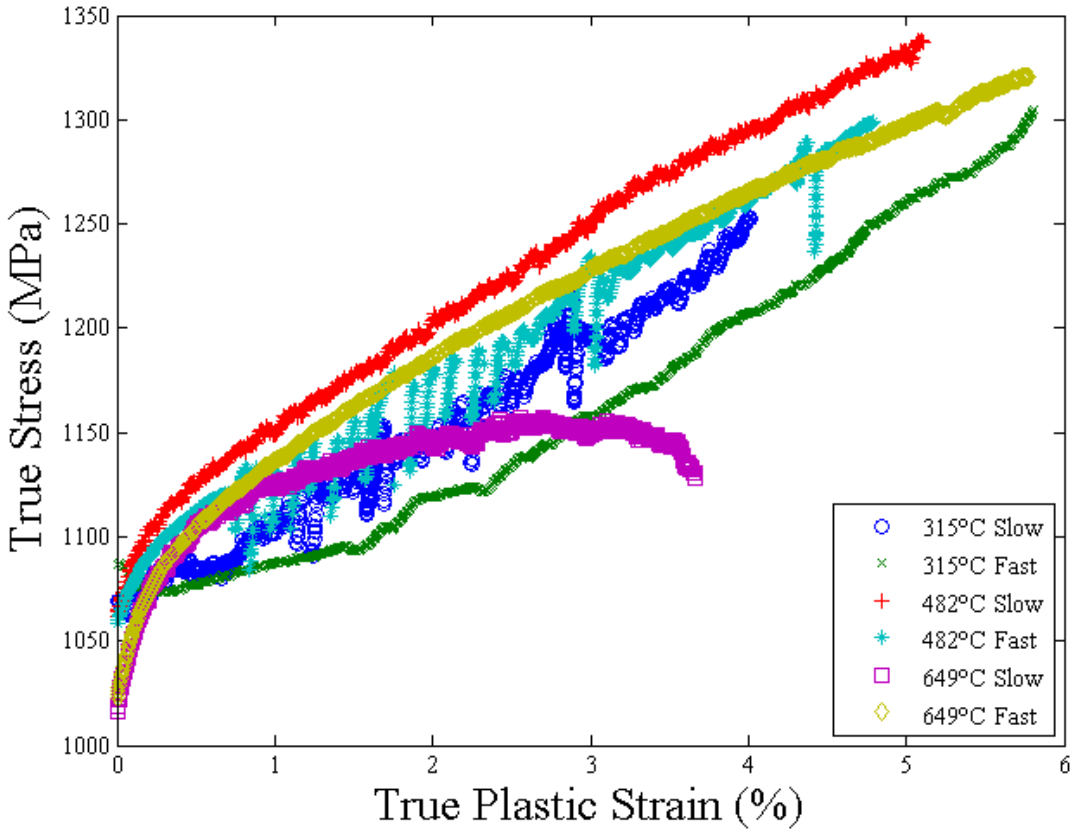

Figure 4.5 - True Stress vs. True Plastic Strain

True stress and true strain were determined from equations 4.1 and 4.2, respectively.

$$\sigma_t = \sigma_n(1 + \varepsilon_n) \tag{4.1}$$

$$\varepsilon_t = \ln(1 + \varepsilon_n) \tag{4.2}$$

where σ_t is the true stress, σ_n is the nominal stress, ε_t is the true strain, and ε_n is the nominal strain. True stress should continue to increase until the material fails; however, the 649℃ slow tests did not exhibit this behavior. A few different explanations can be concluded from this result. Firstly, the incompressibility assumption used in the derivation of equation 4.1 may not be valid for this material tested at high temperatures

and slow strain rates. Classical theories of plasticity assume that materials are incompressible during plastic deformation and this assumption has been experimentally verified. Therefore, this conclusion is disregarded as a possible explanation. Material defects could be a second explanation, especially since this test failed at the thermocouple weld. However, another specimen was tested under these same conditions and exhibited the same type of softening behavior without failure. Thirdly, signal interference could exist in the test setup for prolonged tests at high temperatures, which could affect the results. This is possible, but unexpected since the load cell, displacement LVDT, and extensometer are located sufficiently far from the heated specimen as not to be affected by temperature. It cannot be determined if this effect is true material behavior or if there are some experimental errors. Further research is needed to understand this result better.

Most tests exhibited a stabilized linear hardening rate after 1% plastic strain that persisted until the end of the test. The only anomaly was the 649°C slow test in which failure occurred before 4% plastic strain. A linear regression analysis was conducted on the stabilized portion of each test to better understand and compare the hardening between tests, shown in figure 4.6.

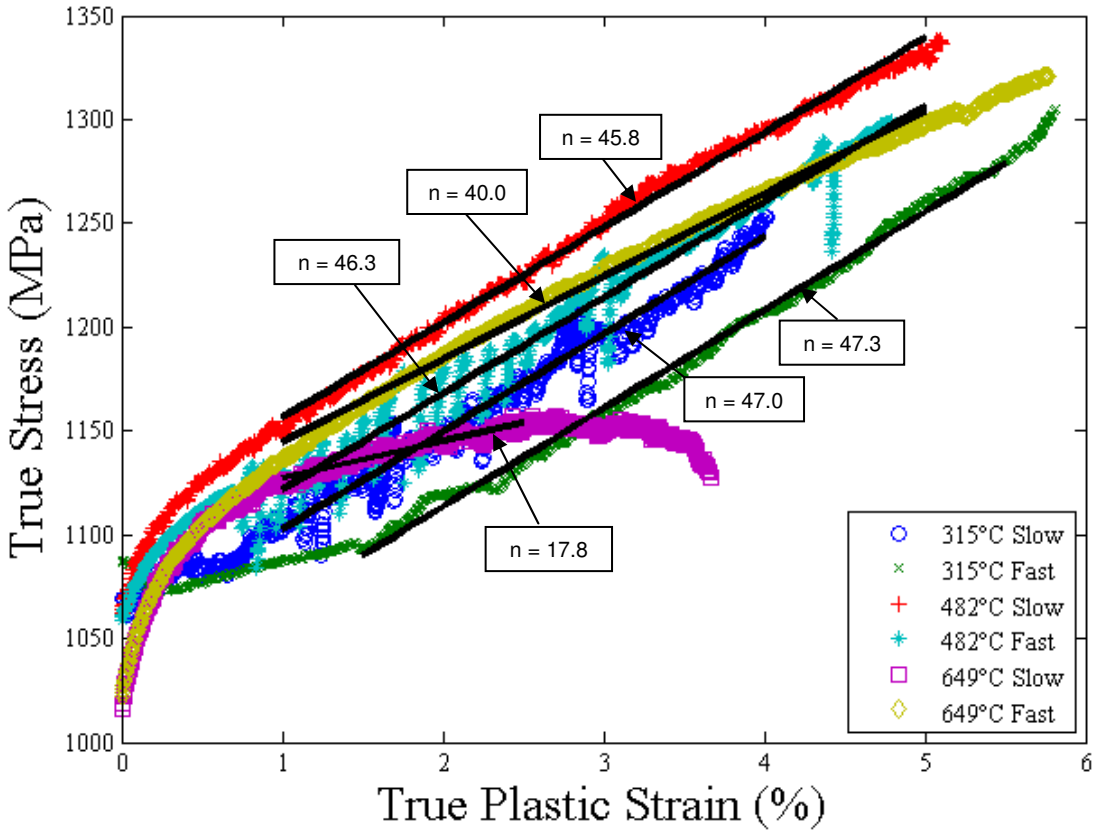

Figure 4.6 - Linear Fit to Stabilized Portion of Tests

From the linear regression results, the overall trends between hardening rate and strain rate are better understood. For every temperature, the stabilized hardening rate is higher for the faster strain rates than the slower strain rates. This result is consistent with the well-established fact that increasing strain rate will increase the hardening rate since faster rates inhibit dislocations from passing around obstacles. Also, the linear hardening rate decreases with temperature since the thermal vibrations allow for easier dislocation motion.

Four out of the six tests exhibited power law behavior. Therefore, these four tests were fitted to a power law curve using equation 4.3.

$$\sigma_y = \sigma_{y,i} + \alpha\left(1 - e^{-\beta\epsilon_p}\right) \quad (4.3)$$

where ε_p is the plastic strain and α and β are fitting parameters. The low temperature, 315℃, specimens did not have typical power law behavior and were not included in this analysis. Figure 4.7 shows the power law prediction for the 482℃ and 649℃ tests.

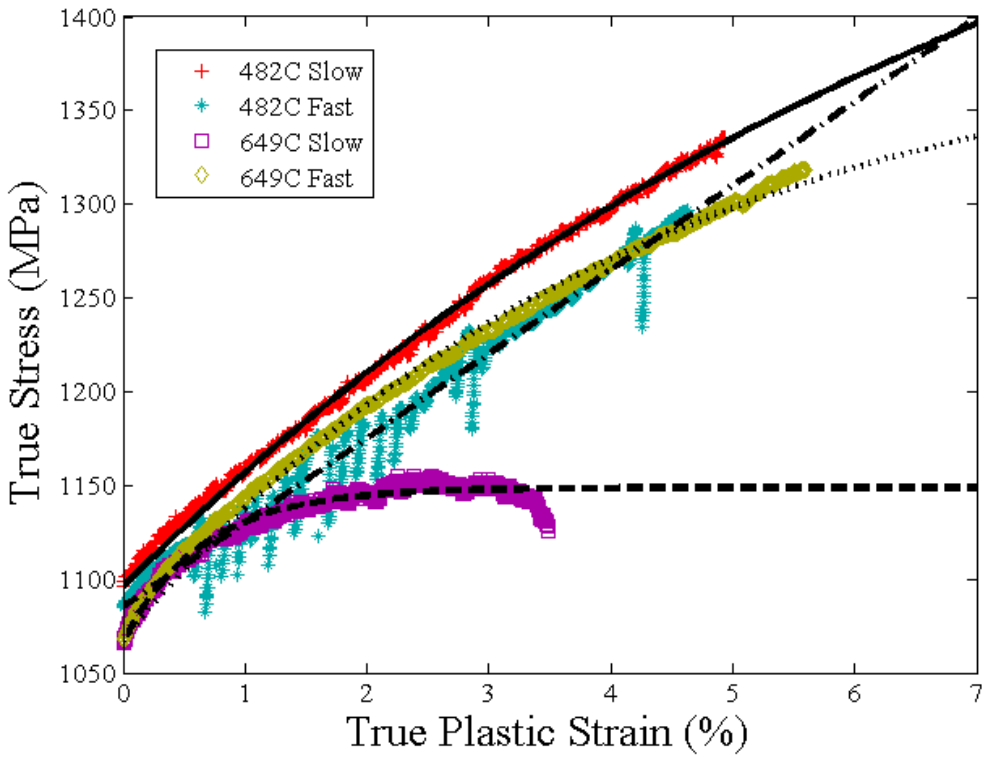

Figure 4.7 - True Stress vs. True Plastic Strain with Power Law Fit

The results from the power law analysis show similar trends as seen in the linear fitting. Overall, the faster strain rates and lower temperatures have a larger hardening rate. Table 4.2 shows a numerical comparison between the hardening rates of each specimen.

Table 4.2 - Numerical Comparison of Linear Hardening Rates

Temperature (°C)	Plastic Strain Rate (*10^{-5}/s)	Linear Hardening Slope (n)	Power Law α (MPa)	Power Law β (*10^{-3})
315	8	47.0	N/A	N/A
315	594	47.3	N/A	N/A
482	7	45.8	513	125.7
482	685	46.3	37,898	1.2
649	10	17.8	82	1,512.2
649	824	40.0	331	237.7

Serrated yielding is evident in two of the six tests. The 315°C slow and 482°C fast tests showed signs of a dynamic strain ageing phenomenon in which mobile solute atoms interacted with moving dislocations to create serrated plastic flow. This type of behavior is referred to as the Portevin-Le Chatelier effect and is common in many substitutionally strengthened alloys.

In summary, the monotonic tests reveal a decrease in the 0.02% offset yield strength with temperature. Also, increasing the strain rate leads to a slight increase in the linear hardening rate of the stress strain curve and increasing the temperature results in a decrease in the linear hardening rate.

4.2 Cyclic Yielding Changing Temperature Test

An important parameter in the modeling of load interaction TMF crack growth is the evolution of the plastic zone ahead of the crack tip. From a yield zone perspective, this area of residual compressive stress in front of a crack controls the amount of reduced crack growth due to periodic overloads. It has been determined that the yield strength varies with temperature; therefore, it is important to understand how the plastic zone changes per cycle, especially in a TMF environment. A test was devised which modeled an entire IN-100 cylindrical specimen as the plastic zone in front of a crack loaded in tension. Cyclic yielding was performed on this single specimen in displacement control while changing the temperature every cycle. The temperature ramped up in three consecutive cycles: 315°C, 482°C, and 649°C; then it ramped back down to 482°C and 315°C. This process was repeated 64 times before the specimen failed. Figure 4.8 shows the overall stress vs. strain results from this test.

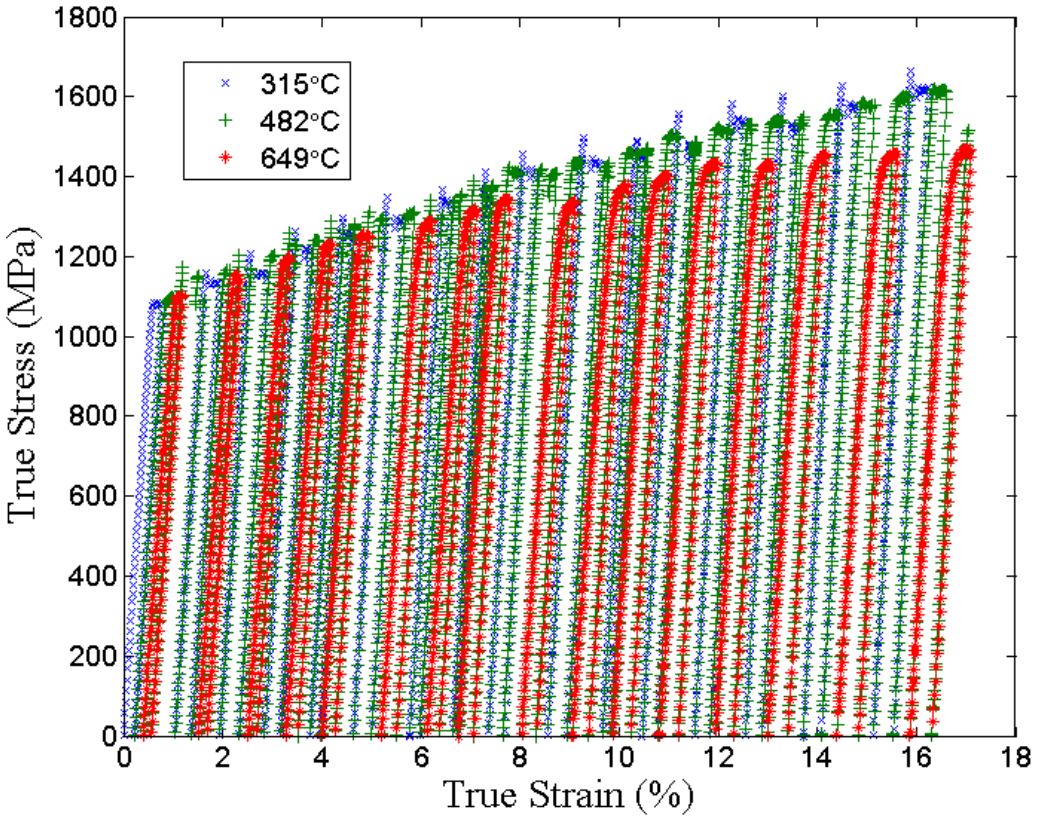

Figure 4.8 - Cyclic Tension, Changing Temperature Stress vs. Strain Response

A better representation of the inelastic stress-strain behavior is shown by plotting only the plastic strains as shown in figure 4.9.

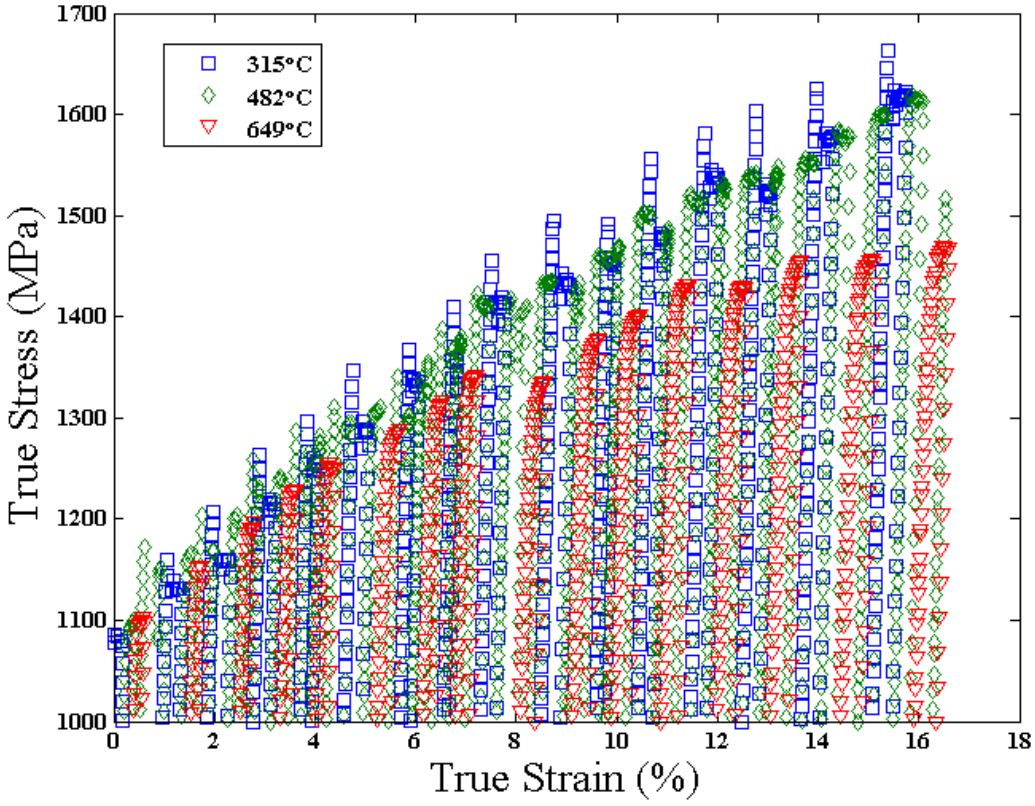

Figure 4.9 - Plastic Region of Changing Temperature Yield Tests

In general, the material increases in flow stress with increasing cycles due to accumulated hardening and dislocation interaction. It is interesting to note the differences in hardening behavior between the temperatures. The lower, 315°C cycles had a much higher hardening behavior than the higher temperature tests. In addition, the 482°C cycles also had a more hardening than the 649°C cycles. More insight into this behavior is shown by adding a three parameter monotonic fit to the cyclic temperature tests, figure 4.10.

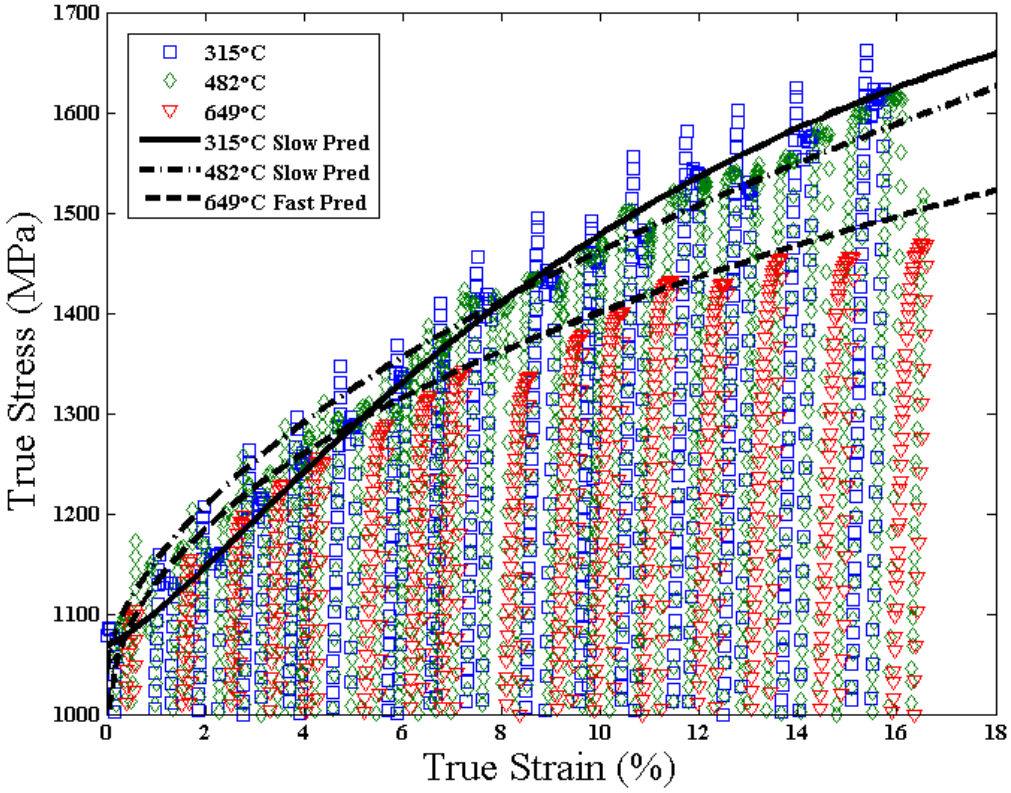

Figure 4.10 - Plastic Region of Changing Temperature Yield Tests with Monotonic Fits

Equation 4.4 was used to obtain these monotonic fits by adding an exponent to the exponential fit discussed previously. This exponent created a near perfect fit to the monotonic data and provided more confidence in extending this fit past 6% strain.

$$\sigma_y = \sigma_{y,i} + \alpha\left(1 - e^{-\beta\epsilon_p}\right)^{\omega} \tag{4.4}$$

where ω is a third fitting parameter along with α and β. It is apparent in figure 4.10 that the 315℃ and to a lesser extent the 482℃ cycles had more hardening than what is predicted from the monotonic data. The 649℃ cycles remained fairly constant when compared to the monotonic prediction throughout the entire strain range. Another

interesting note is the consistent strain bursts that occurred in most of the 315°C cycles and some of the 482°C cycles. The material would harden past the expected yield point, and then suddenly increase in strain causing the load to drop down to the expected flow stress values. This release of energy was accompanied by an audible "ping" emitting from the specimen during the test.

Cailletaud and Chaboche [64] saw similar behavior in IN-100 low cycle fatigue tests at high temperatures. They cycled IN-100 specimens in fully reversed loading while observing the effects of changing temperature. Their tests consisted of constant amplitude loading at temperature, T_0, then a load hold at a higher temperature, T_1, followed by continued cycling at T_0 between the previous load levels. They observed a decrease in the strain amplitude for cycles immediately following a heating cycle, a result indicative of hardening caused by the prior temperature change. It was concluded that higher temperature cycles create microstructural changes within the material that would manifest itself as increased strength when the temperature decreases. Cailletaud et al. went on to include this effect in constitutive models that independently accounted for hardening due to plastic flow and the inherent microstructural changes that occur during overheating.

A similar argument can be presented for the effects seen in figure 4.10. However, microstructural changes seem to suggest a permanent effect that would persist even after the initial hardening. The flow stress decreases once the initial hardening occurs and any transient effects caused by the overheating cycles are no longer apparent. In addition, this effect occurs almost every cycle that the temperature decreases; therefore,

the effect of high temperature cycles could be attributed to a dynamic strain ageing phenomenon.

In summary, the cyclic yielding changing temperature test results in more hardening for the 315°C and 482°C cycles than what is predicted using the monotonic stress vs. strain data. The PLC effect is also apparent in the results of this experiment. A possible explanation for this increase in yield strength is an interaction between solute atmospheres and dislocations. The dislocations become locked when the temperature decreases and subsequent dislocation motion must overcome the energy barrier formed by the solute atoms.

4.3 Dynamic Strain Ageing in IN-100

Dynamic strain ageing has manifested itself in the form of serrated plastic flow in IN-100 at certain temperature and strain rate combinations. This type of stress-strain response is known as the Portevin – Le Chatelier effect and arises due to the complex interactions between diffusing solute atoms and mobile dislocations. Figure 4.11 shows the stress vs. strain response of monotonic tension IN-100 specimens tested at different temperature and strain rates.

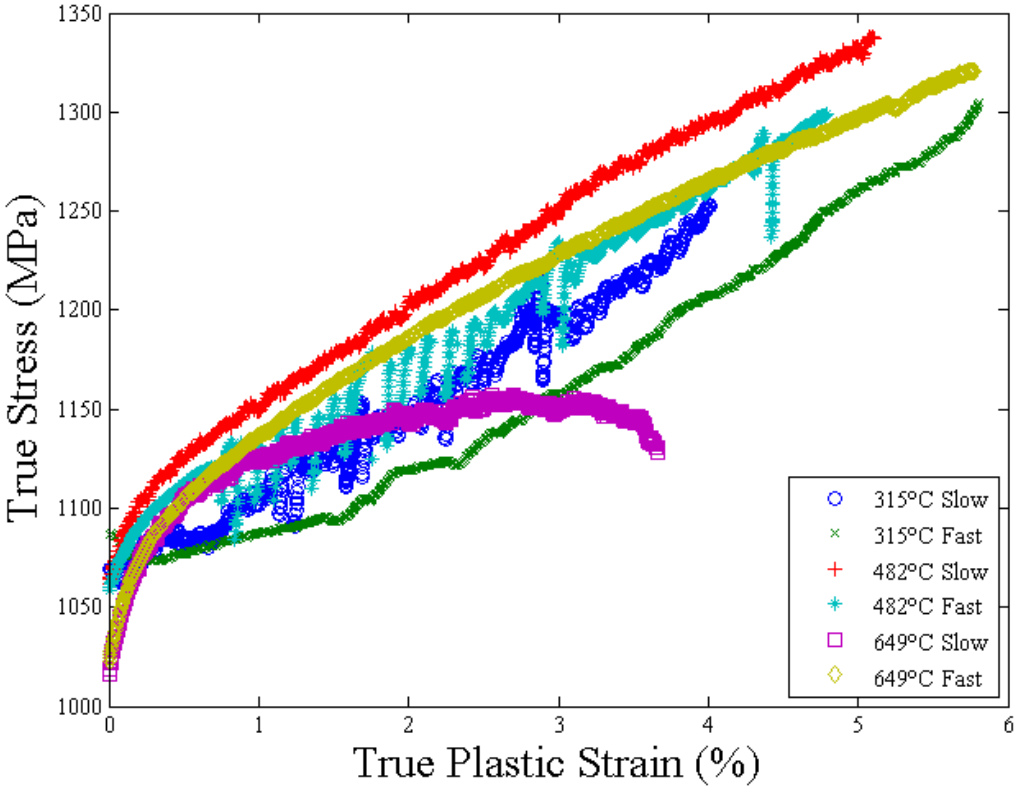

Figure 4.11 - Plastic Region of Monotonic Tests Showing Stable and Unstable Plastic Flow

The slow and fast rates correspond to elastic strain rates around $2x10^{-5}$ and $2x10^{-3}$ s^{-1}, respectively. These tests were performed in displacement control due to the instabilities inherent in strain-controlled tests in the regime where serrated plastic flow is apparent. In some cases, the plastic flow was so unstable that keeping the extensometer firmly attached was a difficult task. The plastic strain rates varied from the elastic strain rates since these tests were displacement controlled, as shown previously in table 4.1. From the data shown in figure 4.11, two out of six tests exhibited relatively large stress drops while the other four tests remained smooth with no serrations. These two tests were the 315℃ slow and the 482℃ fast tests.

4.3.1 Negative Strain Rate Sensitivity Parameter

It is a well-established fact that a negative strain rate sensitivity (SRS) parameter is a direct manifestation of the dynamic strain ageing phenomenon. In many materials, increasing strain rates will result in an increase in flow stress. Materials tend to be "harder" or "stronger" when deformed at faster rates due to the time dependent nature of dislocation motion. Slower strain rates allow dislocations to move around strong obstacles but faster strain rates can cause particle cutting and increase the hardness. This common occurrence is not apparent in the PLC deformation regime as materials become softer with increasing strain rate. A way to quantify this behavior is through the strain rate sensitivity parameter, defined previously in equation 2.10. A schematic of the strain rate sensitivity is shown in figure 4.12.

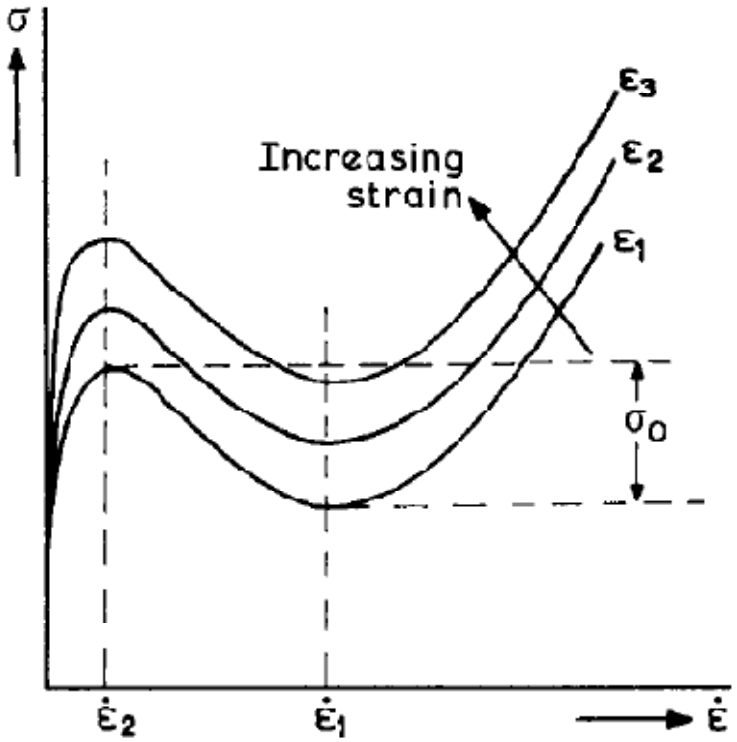

Figure 4.12 – Schematic of Strain Rate Sensitivity and the Flow Stress Dependence on Strain Rate [65]

The flow stress has a negative dependence on strain rate between $\dot{\varepsilon}_2$ and $\dot{\varepsilon}_1$. It should be noted that this is not the same as strain softening. Strain rate sensitivity is a measure of how the hardening behavior changes with strain rate; therefore, a minimum of two tests at different strain rates is needed to determine a material's strain rate sensitivity.

The values of flow stress and strain rate are used to determine the strain rate sensitivity parameter at a constant strain and temperature. This method will identify a result of a dynamic strain ageing process but will not provide an indication of the boundaries within which the PLC effect occurs. Table 4.3 shows the values of the strain rate sensitivity parameter for each of the three temperatures tested.

Table 4.3 - SRS Comparison Between Tensile Test Data

Temperature	Evidence of Serrated Yielding	Average SRS: $m = \frac{\ln(\frac{\sigma_2}{\sigma_1})}{\ln(\frac{\dot{\varepsilon}_2}{\dot{\varepsilon}_1})}$
315℃	Yes	-0.0071
482℃	Yes	-0.0055
649℃	No	+0.0118

As expected, testing conditions that exhibited serrated flow had a negative SRS parameter and tests without serrated yielding had a positive SRS parameter. Further research is needed to better understand this behavior, predict the conditions that cause this effect, and determine its relative importance on crack growth rates.

CHAPTER 5: VARIABLE TEMPERATURE LOAD INTERACTION MODEL

The focus of this thesis is to create a crack growth prediction model that considers the variables associated with temperature change as well as their impact on load interaction effects. Based upon industry experience, many current crack growth models do not explicitly consider temperature changes but apply “knock down” factors to account for higher temperature crack growth. This method is easy to implement; however, it is highly empirical and can result in very conservative life estimates. A better approach to consider temperature changes during crack growth is to study the effect of changing temperature on crack tip conditions. How does the material respond to a large change in temperature? What effect does temperature history have on a propagating crack? How significant are frequency and dwell time effects at high temperatures? These types of questions that are addressed in this chapter.

5.1 Model Physics

The first step in creating a practical variable temperature load interaction model is to define the physics behind crack growth under variable amplitude loading. This model identifies the following physical interactions that are believed to be important factors influencing crack growth.

1. Crack Growth Rate as a Function of ΔK
    - It is a well-established hypothesis that cracks growing in metals can be described by the linear elastic stress intensity parameter, ΔK, if the size of the plastic zone is small in relation to the crack length. Crack growth rates are directly related to the applied ΔK and are dependent on other external variables such as environment, load ratio, and loading frequency.
2. Specimen Geometry
    - Understanding the application of specific geometrical correction factors to the corresponding flaw geometries is critical for accurate model predictions.
3. Stress State
    - Plane stress and plane strain loading conditions result in variability within the plastic zone size. The relationship between plastic zone size and specimen thickness determine the relative amounts of plane stress and plane strain fracture
4. Load Interaction – Crack Growth Retardation and Acceleration
    - Accounting for crack growth retardation and acceleration due to load history is an important consideration in variable amplitude loading situations.
    - Multiple overload effects have been shown to create more retardation than the accumulation of single overloads acting alone.
    - Underload effects serve to reduce the overall effect of an overload.
5. Temperature Interaction – Frequency, and Dwell Effects

- Changing temperatures is common in all TMF spectrums and has been shown to negatively influence crack growth rates due to oxidation and/or material evolution.
- Loading frequency and dwell time can contribute significantly to changes in crack growth rates through specific time and temperature dependent mechanisms.

5.1.1 Crack Growth Rate as a Function of ΔK

Constant amplitude crack growth coefficients were obtained from experimental data obtained by Benjamin Adair at Georgia Institute of Technology [63]. Single edge notched tension (SENT) specimens were cyclically loaded to determine Paris and Foreman coefficients describing crack growth rates as a function of stress intensity range. These tests were conducted at three temperatures: 315°C, 482°C, and 649°C. Figure 5.1 show the results from these constant amplitude tests.

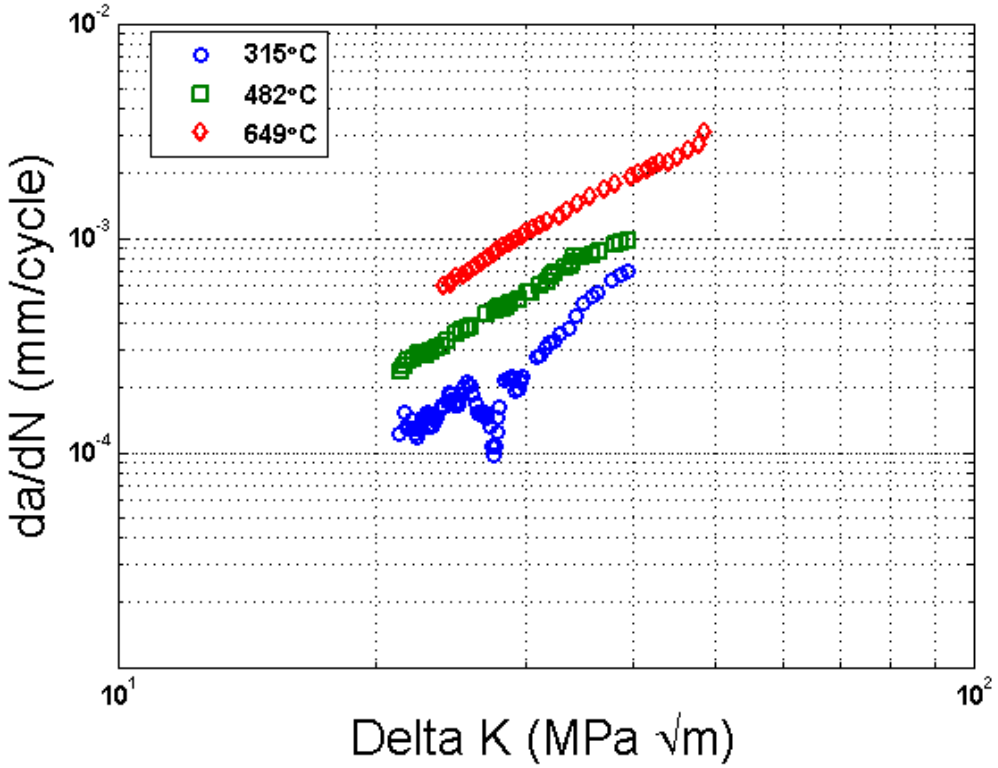

Figure 5.1 - IN-100 Constant Amplitude Crack Growth Rates [63]

The general trends of this data show that higher crack growth rates occur as temperature increases. This is expected since time dependent mechanisms such as creep and oxidation occur at higher temperatures and lead to faster growth. Crack growth coefficients were determined by fitting the data to the Paris Correlation and Foreman Equation, equations 5.1 and 5.2, respectively.

$$\frac{da}{dN} = C_p \Delta K^{n_p} \tag{5.1}$$

$$\frac{da}{dN} = \frac{C_f \Delta K^{n_f}}{(1 - R_{eff}) K_{IC}{}' - \Delta K} \tag{5.2}$$

Table 5.1 shows a list of the fitting coefficients and figure 5.2 shows how well these coefficients correlate to the test data.

Table 5.1 - Crack Growth Coefficients of IN-100

	Paris Coefficients		**Foreman Coefficients**		
Temperature	C_p	n_p	C_f	n_f	K_{IC}' (MPa $m^{1/2}$)
315°C	0.358E-7	2.623	1.595E-5	2.210	140
482°C	1.309E-7	2.441	6.942E-5	1.858	110
649°C	4.433E-7	2.267	24.31E-5	1.658	110

a)

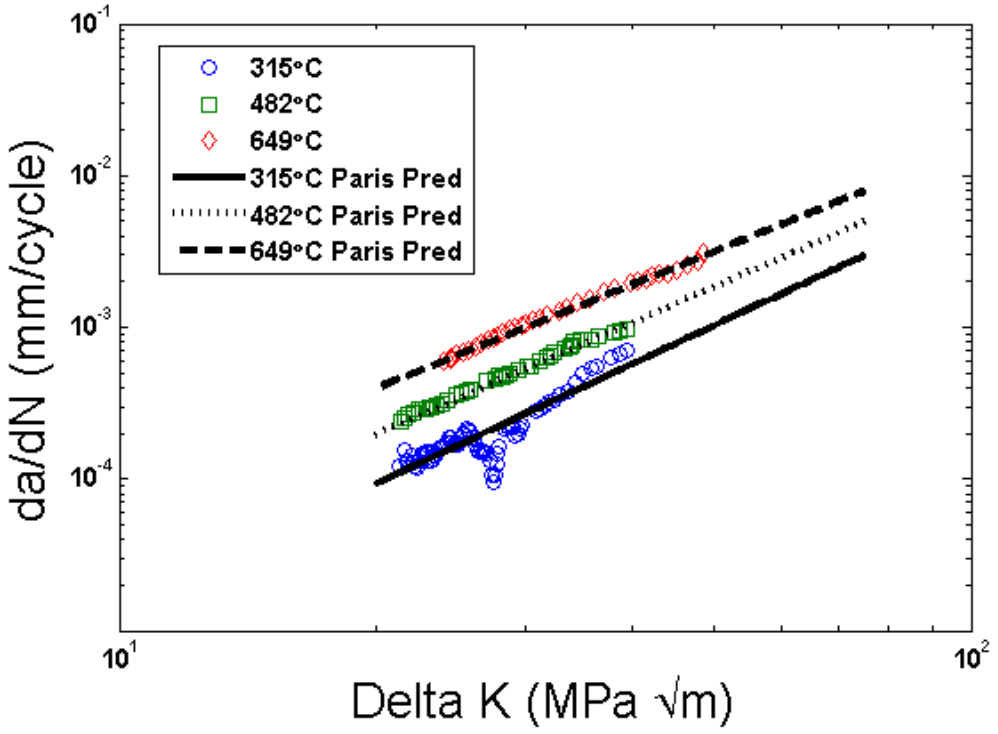

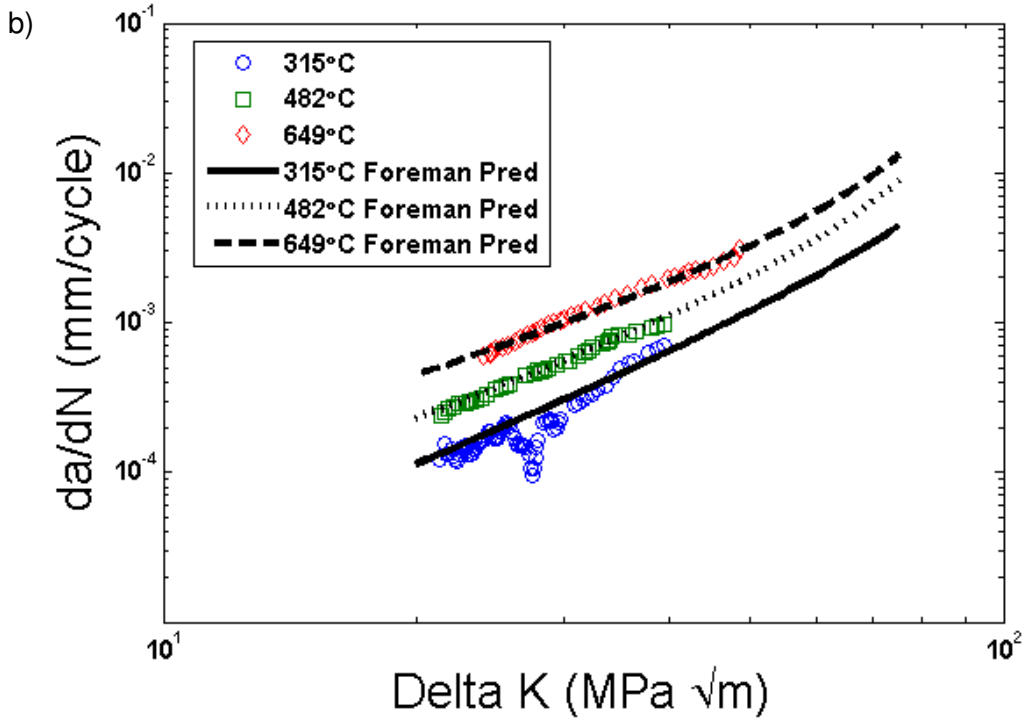

Figure 5.2 - a) Constant Amplitude Crack Growth with Paris Prediction; b) Constant Amplitude Crack Growth with Foreman Prediction

Other researchers have performed crack growth studies on IN-100, which have led to the identification of subtle differences between the testing results based upon testing conditions and material processing. Macha [66] performed crack growth studies on Gatorized™ IN-100 and several years later Larsen, Rosenberger, Hartman, Russ, and John [67] determined crack growth rates on a P/M form of IN-100. Their respective results are shown in figure 5.3a and figure 5.3b.

a)

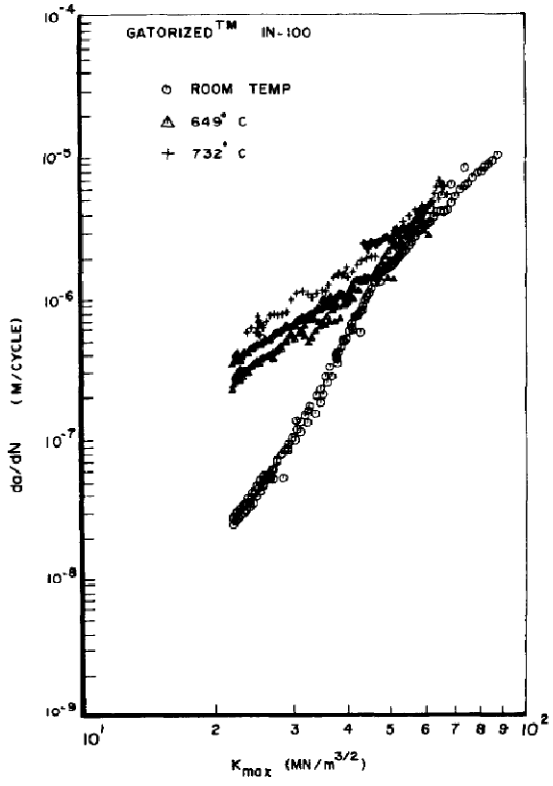

b)

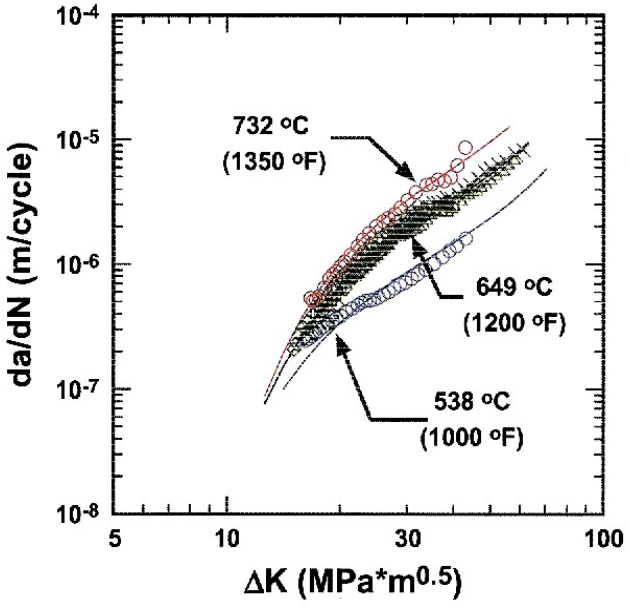

Figure 5.3 - a) Macha's IN-100 Crack Growth Rates [66] b) Larsen et al. IN-100 Crack Growth Rates [67]

Despite testing the same nominal material, there are subtle differences between each of the three tests results that warrant explanation. There is a clear convergence in Macha's data in the crack growth rates at high ΔK and this temperature independent behavior is not seen in figure 5.1 or figure 5.3b. The most probable explanation for this behavior is the differences in testing frequencies. Macha's testing frequencies was 2.5 Hz while Adair's and Larsen's testing frequencies were 0.33 Hz and 0.17 Hz, respectively. High frequency crack growth testing reduces the influence of oxidation, especially at high ΔK and the effect of temperature diminishes causing a convergence in the dadN vs. ΔK curve. Smaller differences between the testing results could be attributed to differences in specimen thickness, processing techniques, and crack length measurement techniques, but the results are fairly consistent between all three authors despite the convergence of Macha's data at high ΔK.

If no load interaction is present, the model determines crack extension per cycle using either the Paris or Foreman equation at the appropriate delta K. The user has the ability to select either a Paris or Foreman prediction prior to calculating crack growth. The predictions in figure 5.2 are extrapolated past the stress intensity limits of the data obtained from the constant amplitude crack growth experiments. This is necessary since crack growth continues until the maximum load exceeds the material allowable to cause instabilities, which lead to fracture. No extrapolation is taken outside the temperature range, 315°C – 649°C. However, if the cycle temperature is within these values, a linear interpolation is performed between the temperature boundaries to determine the crack growth rate. For temperature inputs below 315°C, the model conservatively uses crack growth data at 315°C.

Fracture toughness is used to determine at which point the crack growth will become unstable and the component will fracture. ASTM E399 is the current standard used to determine the linear elastic plane strain fracture toughness in metals. This standardized test can be used at high temperature; however, it has its limitations. Materials that exhibit large amounts of plasticity are not as easily characterized using the stress intensity factor. Increasing temperature also increases the ductility, making this standard less useful at higher temperatures. ASTM E1820 should also be considered if large amounts of plasticity are present. No standardized tests were conducted to determine the high temperature fracture toughness of IN-100 and no data was found in the literature. Therefore, careful estimates were used based on the K_{max} at fracture during the constant amplitude crack growth tests.

5.1.2 Specimen Geometry

Specimen geometry is an important consideration in any versatile crack growth model. Structural components are susceptible to cracking at any location and orientation with its structure; therefore, it is important to provide the necessary tools to determine propagation life in a variety of situations. The current model, which will be presented in section 5.2, allows the user to choose from five common crack geometries with the ability to add more options in future add-ons. These five geometries are:

1. Single Edge Notched Tension
2. Single Edge Notched Bending
3. Center Cracked Tension
4. Double Edge Notched Tension
5. Compact Tension

These standard geometries have well defined stress intensity solutions and are commonly used in traditional crack growth testing. Adding more options such as cracks growing from holes and surface flaws are suggestions for future work.

5.1.3 Stress State

The plastic zone size is not only a function of the stress intensity factor and yield strength, but it also depends on the stress state and the relative amounts of plane stress and plane strain fracture. A measure of plane stress and plane strain fracture can be determined by looking at the fracture surface. Plane stress fracture results in 45° angled planes called shear lips, which form on the outer surfaces of thick specimens. Plane strain fracture is relatively flat and perpendicular to the loading direction. In many cases, there exists a transition between plane strain and plane stress fracture. At large ΔK, the fracture becomes predominantly plane stress since the plastic zone becomes large in relation to the specimen's thickness.

The following convention has been implemented within this model to account for variable stress states during crack growth and is based upon the variable stress state parameter used by Wang and Blom [68] for a strip yield zone model. If the plastic zone is less than $1/6^{th}$ of the thickness of the specimen, plane strain conditions dominate in which $\alpha=3$. If

the plastic zone is more than half of the thickness, plane stress conditions dominate and α=1. A transition region exists for plastic zone sizes between 1/6 and 1/2 which follows a power law relationship to gradually transition into plane stress fracture. An iteration technique is used to determine the plastic zone size since it is a function of the stress state and the stress state is dependent on the plastic zone size.

5.1.4 Load Interaction – Retardation and Acceleration

There are several approaches to account for loading history during variable amplitude loading, but the two main theories are the crack closure and yield zone approach. Crack closure considers a compressive wake behind the growing crack tip that closes the crack, even when far field tensile loads are applied. This theory has been verified experimentally by observing actual crack closure at minimum stresses greater than zero [35]. The yield zone approach utilizes the plastic compressive zone ahead of the crack to reduce the overall stress range experienced at the crack tip and this effect has also been proven experimentally [34]. Both of these models account for load interaction in two distinct ways and both have been experimentally verified.

The yield zone approach was selected as the basis for considering load interaction effects in the variable temperature load interaction model. This decision was made for two reasons. Firstly, a theory was presented which states that the size of the plastic zone ahead of a crack tip changes with temperature. This is because the yield strength of a material is a function of temperature; therefore, changing temperature also influences the size of the plastic zone. The yield zone approach utilizes the relative sizes of the overload plastic zone and current yield zone to determine load interaction effects, so this theory can be modified to consider temperature changes during variable

temperature crack growth. Secondly, the original code for the MPYZ model was available and could be used as a reference during its reproduction as working software [28].

5.1.4.1 Determination of Plastic Zone Size

The plastic zone ahead of a crack tip is the main driver for load interaction effects in any yield zone model. It is what determines the relative amounts of retardation and acceleration. Thus, it is very important to understand which factors influence the size and morphology of the plastic zone. Irwin's approximation to the size of the plastic zone is directly dependent on the yield strength, which changes with temperature. To complicate things further, history effects may have a significant effect on the size of the plastic zone subjected to cyclic loading. Both of these factors must be considered when determining how the plastic zone behaves in a TMF environment. Equation 5.3 calculates the size of the plastic zone for a given stress state, applied K, and yield strength.

$$r_p = \frac{1}{\alpha\pi}\left(\frac{K_I}{\sigma_y}\right)^2 \tag{5.3}$$

It can be seen from equation 5.3 that increasing the plastic zone size is accomplished through either increasing the applied stress intensity factor, decreasing the yield strength, or growing cracks in thin sheets where plane stress conditions dominate (α=1). This model incorporates all three of these variables when determining the plastic zone size.

The morphology of the plastic zone is more difficult to apply to the model. Several recent studies have looked more closely at the stress-strain response ahead of an advancing crack and related it to the effects of crack closure [44-46]. This type of data is useful for characterizing yield zone morphology; however, obtaining this data can be difficult. Therefore, the following results on the residual stress intensity factor will aid in the modeling of yield zone behavior under cyclic loading.

5.1.4.2 Determination of Residual Stress Intensity Factor

The residual stress intensity factor controls the magnitude of retardation based upon the relative sizes of the overload and nominal plastic zone. During the development of this model, it was discovered that Gallagher's residual stress intensity parameter needed to be modified to capture the yield zone change as a function of temperature. Gallagher's derivation assumed the yield strength did not change for both the overload and nominal load cycles. This assumption is valid under isothermal conditions but a new derivation of the plastic zone size is needed to account for variable temperature conditions. The new derivation leads to equation 5.4 and includes the yield strength as well as the "α" parameter, which signifies plane strain or plane stress conditions.

$$K_R^* = \sigma_y \sqrt{(Z_{OL} - (\Delta a + Z))\pi\alpha} \tag{5.4}$$

where K_R^* is the temperature dependent residual stress intensity factor and Z is the plastic zone of the current cycle. Using equation 5.4, the remaining stress intensity factor needed to reach the outer boundary of the overload plastic zone can be determined at any yield stress and for different stress states. The crack transitions from a plane strain to a plane stress state as the crack length increases because a higher

delta K creates a larger plastic zone relative to the thickness of the specimen. The variation in plastic zone size is not only a function of the applied stress, but also depends on the state of stress and the relative amounts of plane stress or plane strain conditions. An iterative process is used to solve for the plastic zone size since the size of the plastic zone is a function of α and α depends on the relationship between the plastic zone size and the specimen thickness.

5.1.4.3 Single Overload Retardation

Crack growth retardation has a significant influence on the lifetime of components under variable amplitude loading. Not including the effects of retardation can result in extremely conservative lifetime estimates. Accounting for retardation effects will save money by decreasing the maintenance costs and increasing the service lifetime of structural components.

From a yield zone perspective, retardation is caused by the compressive stresses ahead of a crack tip loaded in tension, reducing the mean stress of subsequent cycles. Compressive stresses occur upon unloading since the yield zone has been permanently deformed and contains positive strains. Surrounding elastic material closes around the yield zone, placing it in a state of compression. The magnitude of compression can be very high and can cause compressive yielding near the crack tip, resulting in a smaller yield zone known as the cyclic yield zone. Retardation is apparent in specimens that receive a spike overload cycle and generate a large plastic zone. Future cycles at a lower mean stress grow slower since the compressive stresses in the overloaded plastic zone are high. In some cases, large overloads can cause crack arrest and inhibit crack growth under conditions that would usually permit sustained growth. Figure 5.4 shows

the difference between the crack closure and yield zone approach to account for retardation.

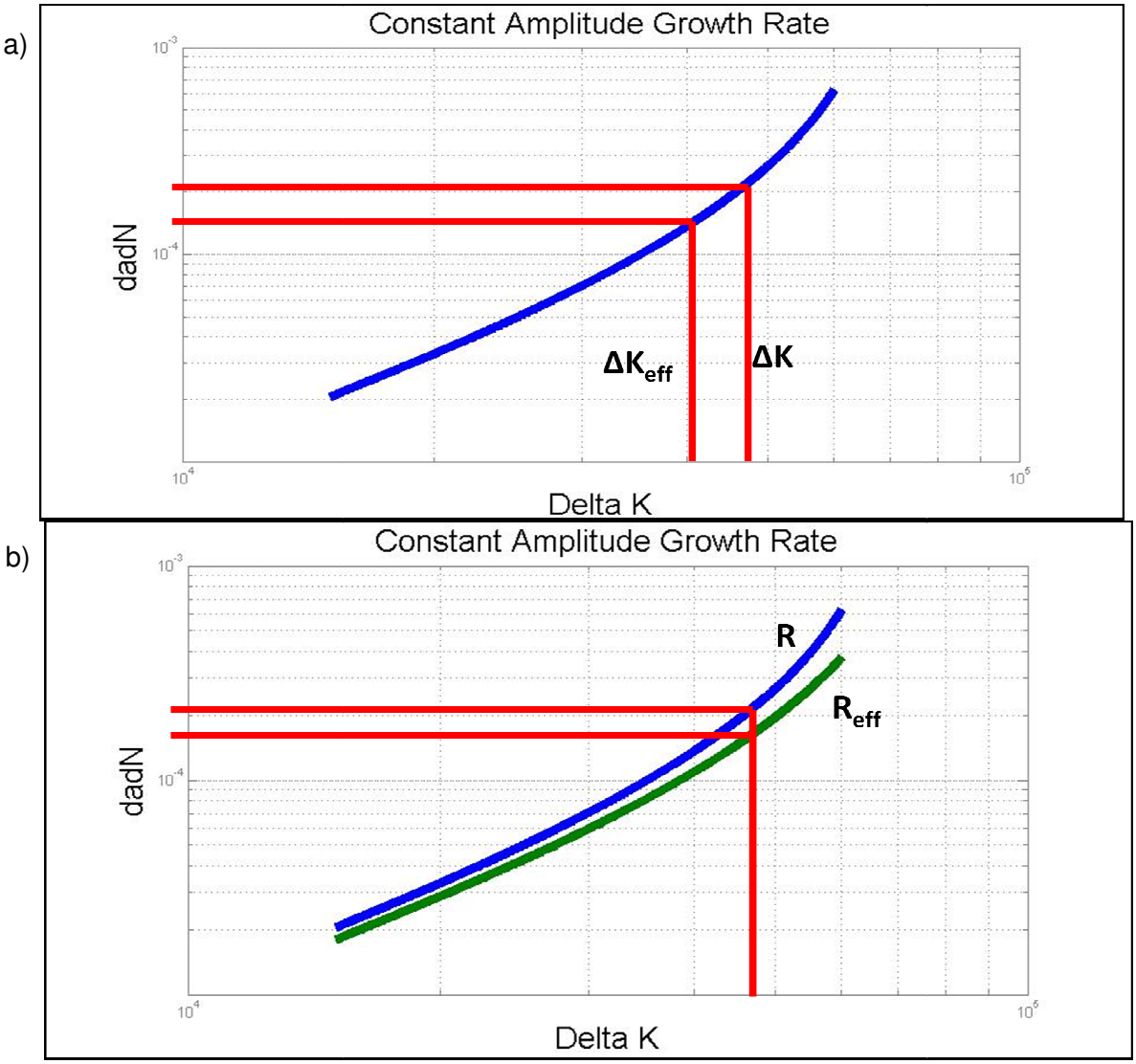

Figure 5.4 - a)Crack Closure Approach to Retardation b) Yield Zone Approach to Retardation

Since retardation in a yield zone model is controlled by decreasing the mean stress of subsequent cycles, an effective R ratio is implemented while keeping the full stress

range, ΔK, constant. Equation 5.5 shows the method used for determining crack growth retardation.

$$R_{eff} = C_1 \left(\frac{1}{\frac{K_{OL}}{K_{max}} - \frac{B}{A}} \right) K_R^{*C_2} + \frac{K_{min}}{K_{max}} \tag{5.5}$$

Two fitting parameters, C_1 and C_2, are used to calibrate the amount of retardation to experimental results. This model includes the same retardation parameters, A and B, as the MPYZ model [28]; however, these terms have been defined to be temperature dependent. The two parameters, A and B, control the level of retardation from a given overload. Parameter A controls the overload to nominal ratio that results in no changes to constant amplitude crack growth rates. In some instances, small overloads do not create a noticeable change in reducing crack growth rates. Therefore, parameter A is identified as the "no retardation ratio." Conversely, parameter B is the overload to nominal load ratio that causes crack arrest. This value is known as the "cut-off ratio." If a component survives an overload that is at or above the cut-off ratio, future crack growth will be nonexistent if the load levels remain at or below nominal values. A linear relationship is assumed to exist between the no retardation ratio and the cut off ratio and any overload in between will have partial retardation. Experimental evidence suggests that the cut-off ratio is a function of temperature; therefore, the model allows for changes to the cut-off ratio depending on the temperature of the overload cycle. Crack growth per cycle is calculated by substituting equation 5.5 into equation 5.2. A flow chart summarizing the method to determine the amount of retardation caused by a single overload is shown in figure 5.5.

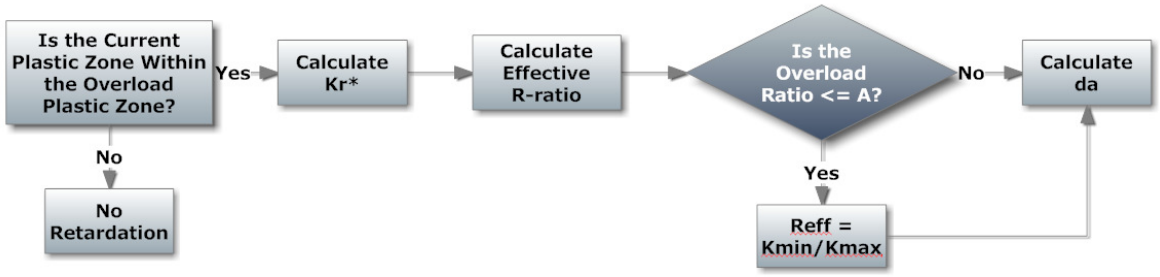

Figure 5.5 - Flowchart of Retardation Analysis

5.1.4.4 Multiple Overload Retardation

Experimental evidence suggests that increasing the number of overloads will increase the amount of retardation [69]. Evidence presented in section 5.5 will also suggest that multiple overloads will have greater retardation than the summation of non-interacting single overloads. Therefore, the effects of multiple overloads are governed by a different physical phenomenon than single overloads.

The thought process behind accounting for multiple overloads is as follows:

1. If an overload occurs, check to see if it is in the range to be considered an isolated single overload or a multiple overload. If the crack grows more than two times the overload zone size, then a single overload is assumed.
2. Determine what percentage of uncracked overload zone size remains after a subsequent overload is applied.
3. Reduce crack growth based upon the percentage of overload zone remaining and a material specific saturation value determined from experimental testing. The saturation value creates a lower limit on the reduction in crack growth; otherwise, the crack growth rates will continue to decrease to zero.

Using this proposed theory, maximum retardation occurs when applying multiple overloads in succession, reducing crack growth to the predetermined saturation value. The effect of multiple overloads is very important for engine spectrum loading since most growth occurs in the influence of multiple overloads applied during take-off and high thrust maneuvers.

5.1.4.5 Underload Effects

Minimum loads that are lower in magnitude than nominal minimum loads have shown to alter the stress field in front of a crack and reduce the retardation formed from previous overloads. The current yield zone model incorporates the underload factor by reducing the overload zone by a factor proportional to the magnitude of the underload. For example, large underloads will negate the effects of retardation more than small overloads. The parameter β, shown in equation 5.6, controls this behavior and is used to define a new overload stress intensity factor, equation 5.7.

$$\beta = \frac{K_{pr} - K_{UL}}{K_{eff}^{OL} - K_{UL}} \tag{5.6}$$

$$K_{max}^{OL} = \frac{\left(K_{eff}^{OL} - K_{max}\right)}{(Z - Y)}(Z - \beta) + K_{max} \tag{5.7}$$

where K_{pr} is the minimum stress intensity factor of the overload cycle, K_{UL} is the minimum stress in the underload cycle, and K_{eff}^{OL} is the effective overload ratio. The extent of reducing the overload is controlled by two parameters, Y and Z. The first underload parameter, Y is the value of β that causes no changes to the retardation

behavior. This will occur when the underload is the same as the nominal minimum load, so Y is usually close to zero. In contrast, the parameter Z is the value of β that completely negates all overload effects. No underload data is available in literature for IN-100; therefore the underload parameters, Y and Z are kept the same as in the original MPYZ model [28]. More experimental research is needed to fully understand the underload effects in IN-100.

5.1.4.6 Acceleration

Crack growth acceleration has been reported by numerous authors [33, 70, 71] who studied the effect of compressive loading on fatigue behavior. Traditionally, compressive loads have been viewed as non-damaging and insignificant since the crack faces remain closed in compression. However, evidence suggests that large compressive loads can accelerate crack growth by creating a zone of residual tensile stresses ahead of the crack tip. This has the opposite effect as tensile overload creating a residual compressive zone, leading to crack growth retardation. Compressive underloads cannot be neglected because of their influence on increasing crack growth rates.

Acceleration can also occur as the plastic zone reaches the outer boundary of the overload plastic zone due to the balance of stresses under the assumptions of the yield zone theory. The reversed plastic zone is the area near the crack tip in compression. Between this area and the monotonic plastic zone, there is an increase in tensile stresses. As the crack approaches this area, the growth rates can increase and quickly return to the non-affected rates under constant amplitude loading.

In addition, crack growth acceleration can occur through the means of oxidation embrittlement of the crack tip in a TMF environment. High temperature crack growth has combined influences of fatigue, oxidation, and creep. These are irreversible processes that can affect crack growth rates, even at lower temperatures. As an example, high temperature cycles create a thermally affected zone in front of the crack tip. Upon lowering the temperature, the crack front remains weakened by the high temperature cycles and the crack will grow faster than expected through this thermally affected zone. Temperature interaction effects are used to describe this behavior.

5.1.5 Temperature Interaction – Frequency, and Dwell Effects

The model uses the testing frequency and the number of cycles at specific test conditions to determine the size of the thermally affected zone in front of the crack tip. It is assumed that this zone increases with time following a functional form similar to a short term oxidation growth equation developed by Reger and Remy [23], shown in equation 5.8.

$$x = \mu\sqrt{t} \tag{5.8}$$

where χ is the size of the thermally affected region, μ is a fitting coefficient similar to the diffusion coefficient, and t is time. This oxidation model was developed for course grained, cast IN-100 at temperatures around 1000℃. Its direct application to the variable temperature model would be misleading since the P/M specimens are fine-grained and the experimental temperature range is well below 1000℃. In addition, visual inspection does not show appreciable oxide depth for this alloy at 649℃. However, it is verified through experimental data outlined in chapter 4 that significant

microstructural changes do occur when cooling these specimens in the range of 315°C to 649°C and these changes lead to an acceleration of crack growth. With this in mind, the thermally affected zone is determined by equation 5.8 with μ being a linear function of temperature and encompasses more than isolated oxidation effects but also includes a measure of microstructural variability within the thermally affected zone. The crack growth rates return to nominal constant amplitude values once the accelerated crack growth exceeds the thermally affected zone.

5.2 Model Development

This section is divided into three parts: programming overview, sequence of events, and input file. A discussion about the programming language selection is followed by an outline of the top-level calculation steps involved in the model. Lastly, a detailed description of the material and loading input files is given.

5.2.1 Programming Overview

C++ is the programming language chosen for this model. MATLAB was also considered, but C++ is a more versatile language that can be used across multiple platforms. It has a vast knowledge base since it is a common language used by many people and has very fast computation times. A drawback to using C++ is its complexity, as it is not as user friendly compared to other languages. It also does not have the built-in mathematical capabilities like standard MATLAB software. However, the advantages of using C++ outweighed the disadvantages making it a viable option for this project.

5.2.2 Sequence of Events

The original MPYZ model was reproduced first and then other features were added. A flow chart that describes the top-level calculation steps is shown in figure 5.6.

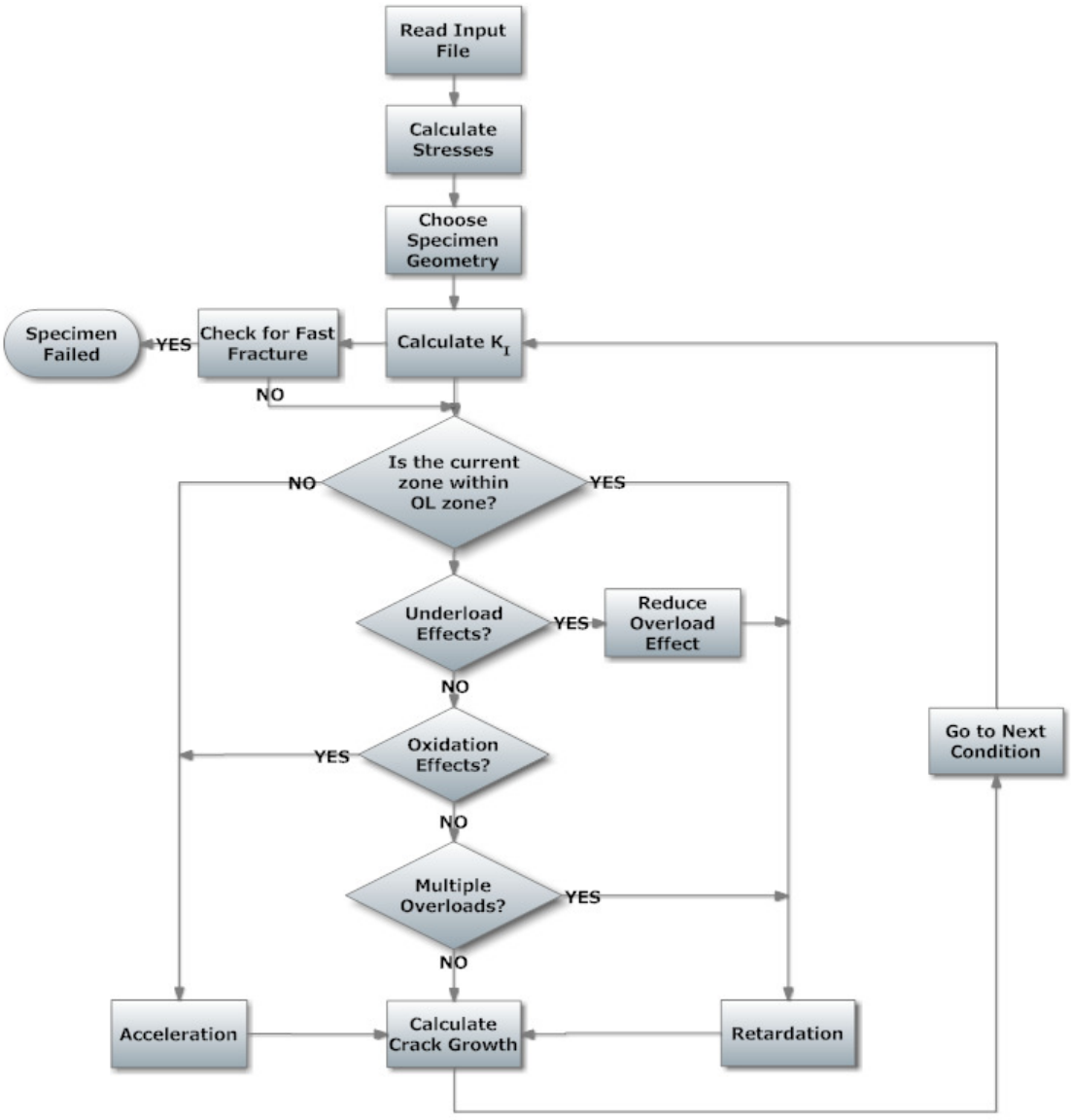

Figure 5.6 - Flow Chart Showing the Basic Calculation Steps Used in this Model

The program begins by reading in the input file containing material information and the load file containing the spectrum. Initial load inputs are combined with the specimen geometry to determine stresses, which are converted into a stress intensity factor dependent on the crack length. The plastic zone size is calculated every cycle and compared to the overload zone size, which may or may not exist. Underload effects are applied if underload conditions are present which decrease the apparent retardation. Oxidation effects are also applied if the temperature change warrants an acceleration to crack growth and multiple overload effects are also considered to increase retardation if multiple overload conditions are satisfied. All of these factors combine to calculate crack length on a cycle-by-cycle basis, checking every cycle to determine if the conditions are right to cause instability and subsequently, fast fracture. The overall procedure did not vary much from the original MPYZ model, but the details for determining the amount of crack growth, load interaction, and temperature interaction effects did change.

5.2.2 Input File

Many initial parameters must be known before any calculations can be made. These input parameters include:

- Specimen Geometry
    - Width
    - Thickness
- Crack Geometry
    - Initial crack length
    - Type of crack (single edge notch, compact tension, etc.)
- Applied Loads
- Cycles at Loading Condition

- Temperature at Loading Condition
- Loading Frequency
- Constant Amplitude Crack Growth Coefficients*
- Yield Stress as a Function of Temperature*
- Fracture Toughness*
- Threshold Stress Intensity Range*
- Overload and Underload Parameters*
- Diffusion Coefficient*

The last six items (marked by an asterisk) listed must be experimentally determined properties. The first five items are input parameters that are conditions associated with the current prediction and are material independent. All of these inputs are stored into one of two writable text files. The first input file contains material and geometry data and the second file contains the load spectrum values. Figure 5.7 shows the material input file.

```
Specimen Geometry
width = 38.7516
thickness = 2.5908
initial crack length = 15.1917

Temperature Values
Temp1 = 315
Temp2 = 482
Temp3 = 649

Material Strength vs Temperature Coefficients (2nd Order Poly)
YSvTa = -3.998e-4
YSvTb = 1.315e-1
YSvTc = 1.070e3
Ultimate Strength = 1378.951456


Paris Coefficients
CP1 = 3.58389839e-8
CP2 = 1.30878043e-7
CP3 = 4.43286702e-7
nP1 = 2.6230
nP2 = 2.4407
nP3 = 2.2667

Foreman Coefficients
CF1 = 1.59473734e-5
CF2 = 6.94187361e-5
CF3 = 2.43113400e-4
nF1 = 2.2103
nF2 = 1.8576
nF3 = 1.6576
Kcp1 = 140
Kcp2 = 110
Kcp3 = 110

Fracture Toughness
Kc1 = 75
Kc2 = 77
Kc3 = 79
Threshold DK = 0

Load Interaction Parameters
A = 1.0
B_a = 3.85e-4
B_b = 1.99
Y = 0.0
Z = 0.5

Diffusion Coefficient at 1000C
Diff_Coeff = 4.4e-5
```

Figure 5.7 - Input File Containing Material and Geometrical Parameters

The current version of the variable temperature load interaction model only allows three temperature points to define material properties. In this case, material data was gathered at 315°C, 482°C, and 649°C. The yield strength as a function of temperature is determined using a polynomial fit in the form shown by equation 5.9.

$$\sigma_y = aT^2 + bT + c \tag{5.9}$$

The coefficients *a*, *b*, and *c* are identified as YSvTa, YSvTb, and YSvTc in the input file. The polynomial fit must be determined from data plotted in MPa vs. degrees Celsius. Specific units must be used in the input file in order to get meaningful results. Lengths must be in millimeters and forces must be in Newtons. Other data, such as the Paris and Foreman coefficients must be determined from data plotted in units of mm/cycle vs. MPa-$m^{1/2}$. It is important to note that there is a space character after each equals sign before the value of each parameter. This space is necessary due to the method used to read data into the crack growth program. The software code reads data by searching for a "=" character in each row, then moves two characters to the right before it begins storing information. Not including the space character after the equals sign will result in the first digit being excluded from the intended value.

Load interaction parameters were described in the previous section. It is important to point out that there are two values for the cut-off ratio identified as B_a and B_b. These values are defined to be the coefficients of the cut-off ratio as an increasing linear function of temperature. Equation 5.10 shows the determination of the cut-off ratio as used in the model.

$$B = B_a * T + B_b \tag{5.10}$$

The threshold stress intensity range determines the lower limit of ΔK for which no crack growth will occur. Small stress oscillations can have little influence on crack growth and can act like a dwell load, which does not propagate cracks under pure fatigue loading.

In this research, the threshold stress intensity range was not experimentally determined; therefore a conservative assumption of $\Delta K_{th} = 0$ was used in all analysis.

The load spectrum input file contains five columns of data separated by a tab character, figure 5.8. The five columns are identified as minimum load, maximum load, cycles, temperature, and frequency. New rows can be appended to the load spectrum depending on the number of conditions the user wishes to include.

Pmin	Pmax	Cycles	Temp	Freq
756	15124	1	649	0.33
756	7562	3000	649	0.33
756	7562	2000	482	0.33
756	15124	1	500	0.33
756	7562	3000	649	5.00
756	7562	5000	315	0.33

Figure 5.8 - Sample Input Load Spectrum

For the example spectrum shown in figure 5.8, the first condition is a single cycle at 649°C with a minimum load of 756 N and a maximum overload of 15124 N. The second condition has a lower maximum load of 7562 N that cycles 3000 times. Next, the temperature is lowered to 482°C and the same nominal stress level is cycled another 2000 times at the same frequency. Another 2.0x overload is applied during condition five, but this overload is at 500°C. Next, the nominal stress level is applied for 3000 cycles at 649°C but at 5 Hz instead of the previous 0.33 Hz cycles. Finally, the temperature is decreased to 315°C and the frequency is decreased to 0.33 Hz for 5000 cycles. All of these inputs are valid, if the temperature of each condition falls within the range specified in the material input file. For example, figure 5.7 shows a lower and

upper temperature bound of 315°C (T1) and 649°C (T3), respectively. The program will recognize if the user attempts to specify a condition outside of these bounds and a warning will appear during the crack growth analysis. It is recommended that all conditions fall within the temperature range provided in the material input file.

5.3 Experimental Calibration and Validation

Experimental calibration and validation is needed in order to confirm or deny the proposed physics behind the variable temperature crack growth model. These experimental results have been obtained from previous studies performed on IN-100.

5.3.1 Single Overloads

Macha [66] performed high temperature overload studies on IN-100 to quantify the effect of temperature and overload ratio on the number of delay cycles. This analysis provided enough information for the calibration and verification of the retardation subroutine. The constants, C_1 and C_2, were obtained through careful analysis of Macha's data.

Constant amplitude crack growth rates were given for three different temperatures, room temperature, 649°C, and 732°C, as shown previously in Figure 5.3a. and Paris and Foreman coefficients were approximated through the data. These coefficients are shown in table 5.2.

Table 5.2 - Approximated Crack Growth Coefficients

	Paris Coefficients		**Foreman Coefficients**		
Temperature	C_p	n_p	C_f	n_f	K_{IC}' (MPa $m^{1/2}$)
Room Temp	7.59E-11	4.36	4.35E-8	3.98	200
649°C	5.65E-7	2.17	2.62E-4	1.84	200
732°C	2.30E-6	1.86	1.03E-3	1.54	200

The 649°C results are comparable with the constant amplitude crack growth data shown previously in table 5.1. The room temperature and 732°C coefficients are outside of the range of data presented in table 5.1, but the trends show the expected results, giving confidence in the applicability of these coefficients. The only difference between the coefficients presented in table 5.2 and those in table 5.1 is the apparent fracture toughness. This variable is used as a fitting parameter in the Foreman equation in order to match testing results and has no bearing on the actual fracture toughness, which controls failure. Theoretically, this value would be material specific and manifest itself as the asymptotic stress intensity factor in stage III crack growth; however, it is difficult to capture stage III crack growth since the crack is growing very fast and crack tip deviations can lead to invalid test results. The importance of the fracture toughness shown in table 5.1 and table 5.2 is to obtain good fits to crack growth data and does not provide a means for determining failure thresholds.

In order to determine approximate measures of single overload retardation, Macha's single overload data needed to be incorporated into a useable form that could be recognized by model inputs. This required the conversion of delay cycles (as presented by Macha) into an effective R-ratio, which could be used in the model. This task was

difficult since there is not an analytical connection between delay cycles and R_{eff}. Fortunately, some of the terms in equation 5.5 could be obtained from Macha's work including the modified residual stress intensity factor (K_R^*) and the cut-off ratio (B) as a linear function of temperature, figure 5.9.

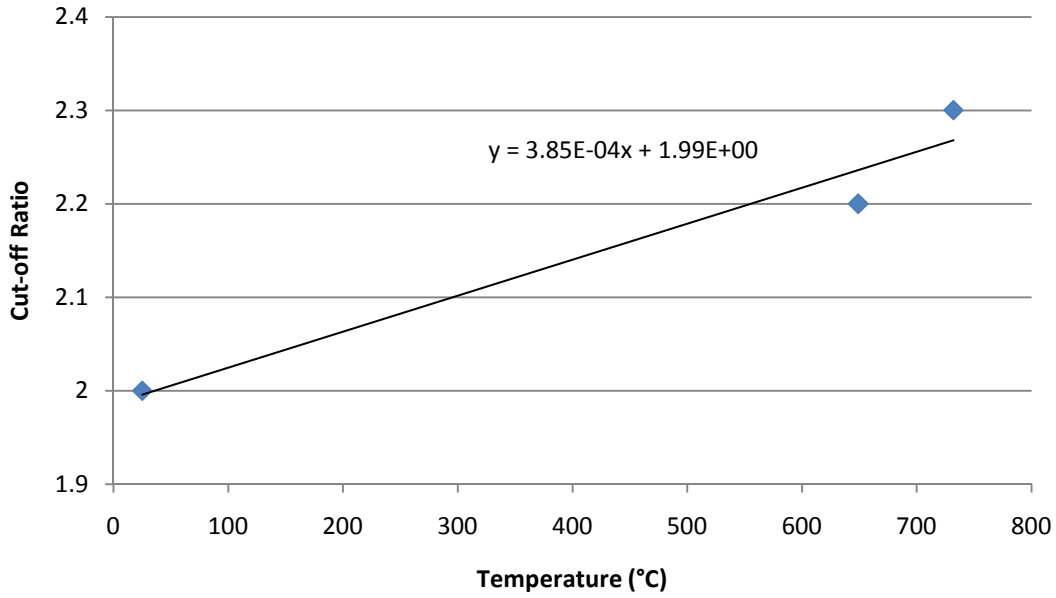

Figure 5.9 - Cut-off Ratio as a Function of Temperature

The fitting constants, C_1 and C_2, were determined through extensive iteration of the model to determine the delay cycles following a specified overload. The first fitting parameter, C_1, controls the magnitude of retardation across the entire plastic zone. The second parameter, C_2, controls the shape of the R_{eff} vs. K_R^* curve, dictating the change of retardation through the plastic zone. For example, the delay cycle vs. overload ratio curve exhibits a power law relationship resulting in much higher delay cycles for larger applied overloads as seen in figure 5.10. From this data, it is assumed that C_2 must be greater than one to increase the delay cycles at high overload ratios and decrease the

delay cycles at low overload ratios. From the iterative analysis, the following values for the fitting parameters were determined: C_1 = 8.5E-5 and C_2 = 2.3.

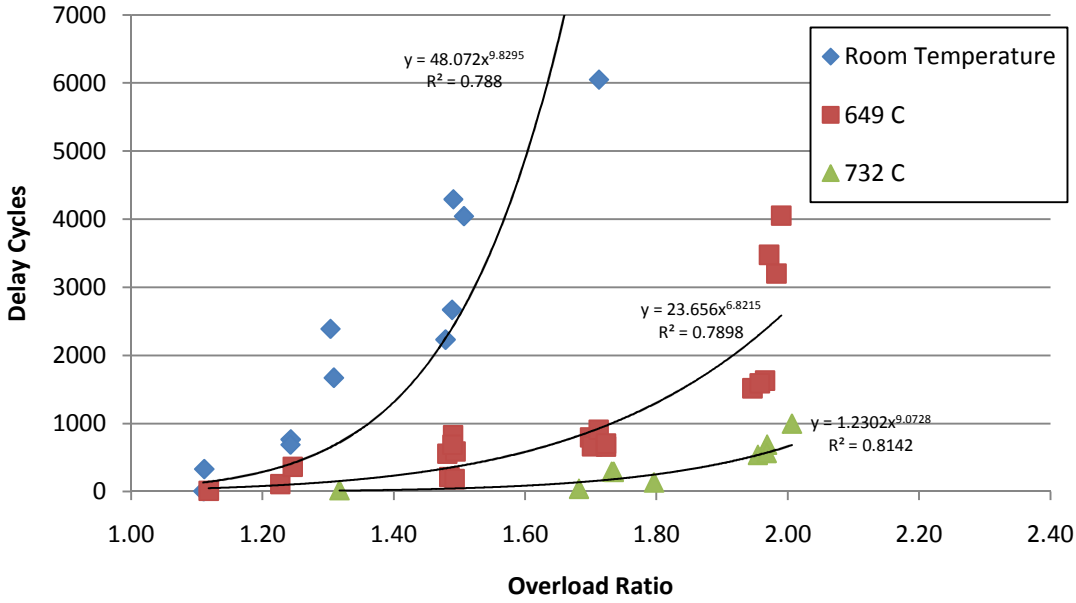

Figure 5.10 - IN-100 Delay Cycles vs. Overload Ratio [66]

Predictions to the overload data were obtained once the fitting parameters were determined, as shown in figure 5.11. The model predictions show the correct trends of decreasing retardation with increasing temperature. This is the result of two competing mechanisms: a larger yield zone due to lower yield strengths at higher temperatures and a higher cut-off ratio at increasing temperatures. In general, a larger yield zone should impart larger compressive stresses and increase the amount of retardation. However, the complex interactions between fatigue, creep, and oxidation negate that effect at higher temperatures. Increasing the cut-off ratio is an indirect measure of oxidation and creep, which affect the post overload crack growth rates. This factor has a bigger

influence on retardation than the size of the yield zone, thus reducing the amount of retardation at higher temperature.

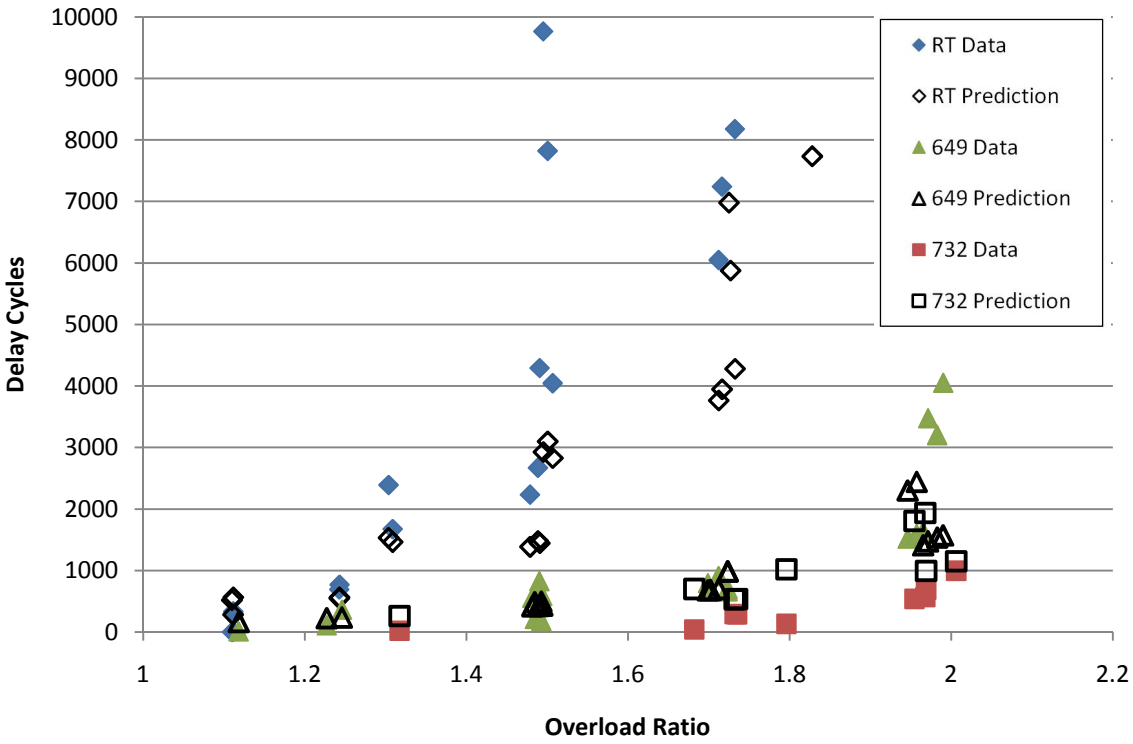

Figure 5.11 - Data from Macha's Results along with Model Prediction

There is wide scatter in the delay cycles vs. overload ratio, which is usually inherent in any fatigue experiment. This makes it difficult to be fully confident in any life predictions. Room temperature predictions are conservative while the 732°C predictions are nonconservative. Modifying the fitting parameters to give conservative estimates in all cases decreases the accuracy of the predictions. Therefore, care should be taken when applying the model for temperatures around 732°C since they may result in nonconservative lifetime estimates.

A parametric study was performed to assess the numerical differences between the overload magnitude and resulting decrease in crack growth for various temperatures. A 2.0X and 1.6X overload were applied for 315°C, 482°C, and 649°C. The results of this study are presented in table 5.3.

Table 5.3 - Numerical Comparison of the Retardation between 1.6X and 2.0X Overloads

	1.6X Overloads			2.0X Overloads		
	315°C	**482°C**	**649°C**	**315°C**	**482°C**	**649°C**
dadN Before*	0.24	0.50	0.98	0.23	0.49	0.95
dadN After*	0.18	0.38	0.75	0.05	0.14	0.35
% Reduction	27%	25%	23%	78%	70%	63%

*Represents Nominal Values

The numerical results shown in table 5.3 confirm the trends shown in Macha's single overload experiments. Increasing the overload has a more significant effect than changing the temperature and increasing the temperature leads to a diminished overload influence. In addition, the percent reduction range increases with overload size, which is a result of the cut-off ratio's dependence on temperature.

5.3.2 Multiple Overloads

The effect of multiple overloads on crack growth behavior has been shown to increase the amount of apparent retardation [69]. This effect is explained through crack closure considerations by amplifying the compressive residual stresses in the wake of an advancing crack. Adair [63] performed multiple overload studies on IN-100 by applying

overloads every 800 cycles. The results from this study and the influence of multiple overloads are shown in figure 5.12.

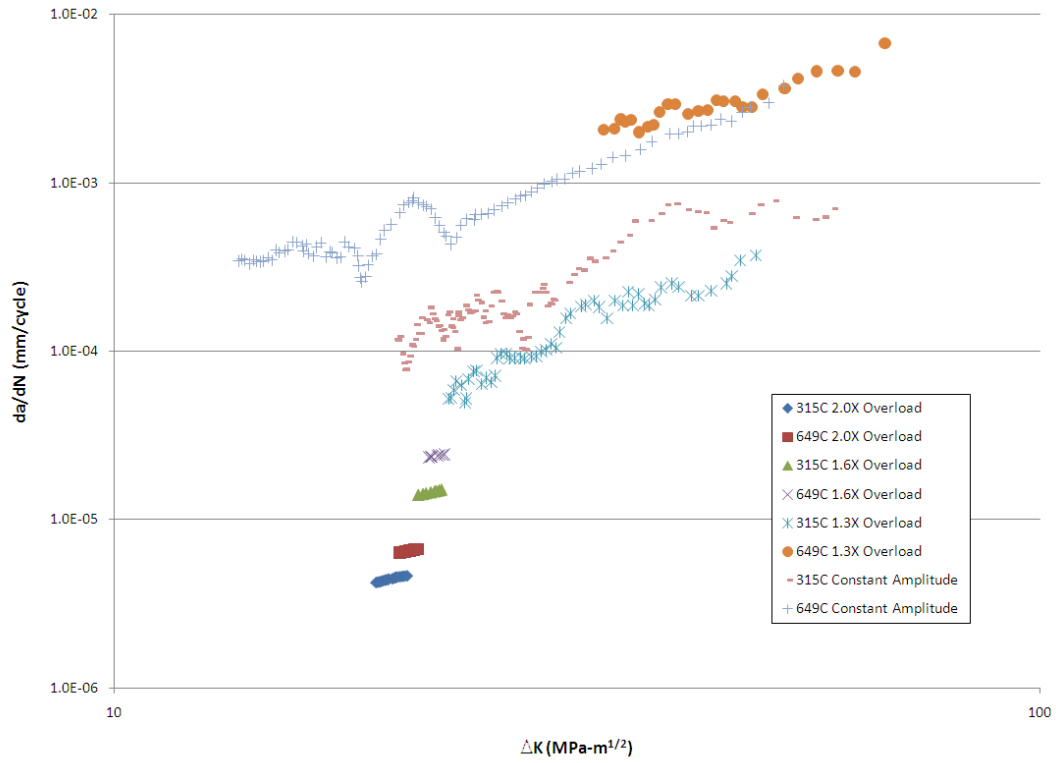

Figure 5.12 - dadN vs. ΔK Representation of the Multiple Overload Data

Multiple 2.0X overloads reduce the constant amplitude crack growth rates by as much as 100%. This is lower than the 63% maximum reduction from a single 2.0X overload shown previously in table 5.3. To add to the disparity, the data shown in figure 5.12 is an average reduction across 800 cycles; therefore, the maximum retardation due to multiple overloads could actually be greater than the calculated 100% reduction. Multiple overloads of this magnitude and frequency are rare in turbine disk spectrum loading; however, it is possible for overloads to interact and cause a higher amount of retardation than what would be expected from a single overload case.

The variable temperature model calculated predictions without accounting for the reduction in crack growth rates due to multiple overloads. The results of this study are shown in figure 5.13.

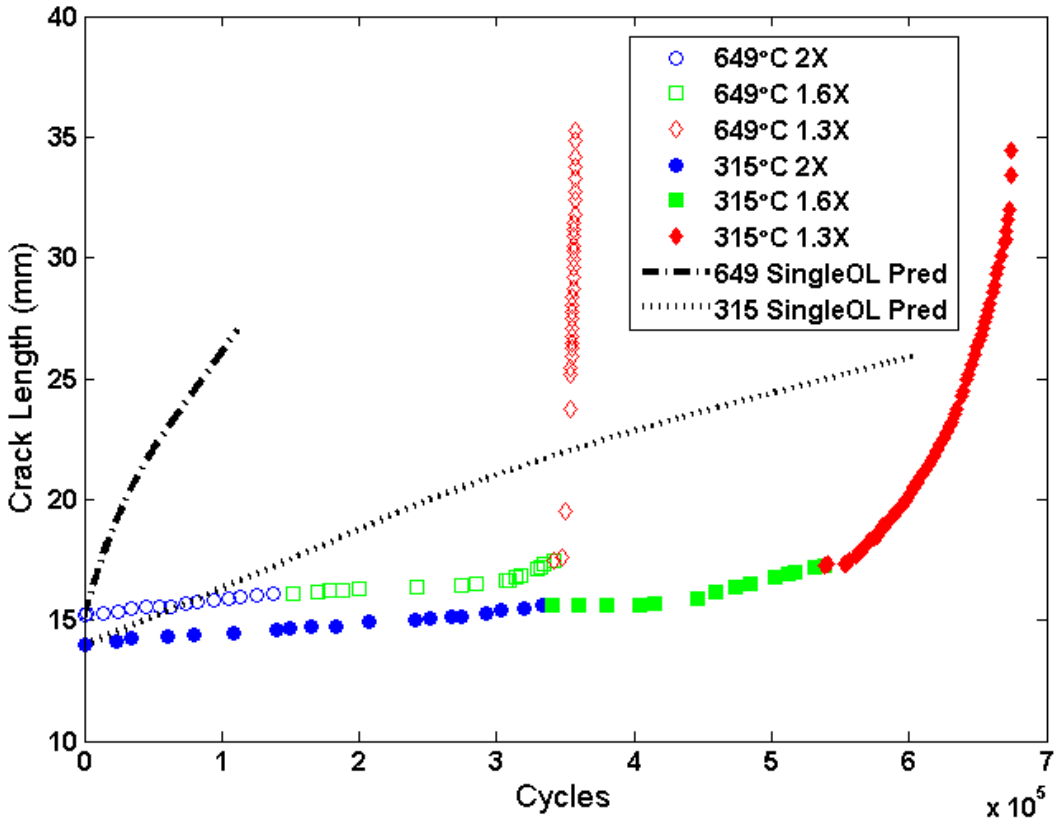

Figure 5.13 - Multiple Overload Data with Single Overload Predictions at 315°C and 649°C

Both the 315°C and 649°C predictions show faster crack growth than what is apparent in the multiple overload data. This result supports the conclusion that a yield zone model that does not account for multiple overloads can lead to very conservative life estimates. It also suggests that the crack closure phenomenon has credibility and can have significant contributions to load interaction effects.

Another possible explanation for the discrepancy between the model predictions and overload data could be in the differences between Macha's overload tests and Adair's tests. As previously stated in section 5.1.1, there are differences between the two materials and the way the tests were performed. Macha tested Gatorized™ IN-100 and grew cracks at a constant ΔK. Adair had a P/M form of IN-100 and tested at an increasing ΔK. These differences in materials and testing procedures could produce the variations seen in applying a model calibrated to Macha's single overload data to Adair's multiple overload tests.

Another important observation from figure 5.13 is the slight change in slope of the prediction around 20 mm. This is caused by the variable α-parameter controlling the relative amounts of plane strain and plane stress fracture. At low ΔK, the crack growth is predominantly plane strain resulting in a smaller plastic zone size. At higher ΔK, the crack growth transitions into plane stress fracture with larger plastic zone sizes. The larger plastic zones of the overload cycle increases the amount of retardation, which decreases the slope of the crack length vs. cycles curve.

The multiple overload sub-routine was added into the model because of the inability for single overloads to predict the enhanced retardation formed by multiple overloads adequately. Figure 5.14 shows the same overload data as figure 5.13, except with predictions accounting for multiple overloads.

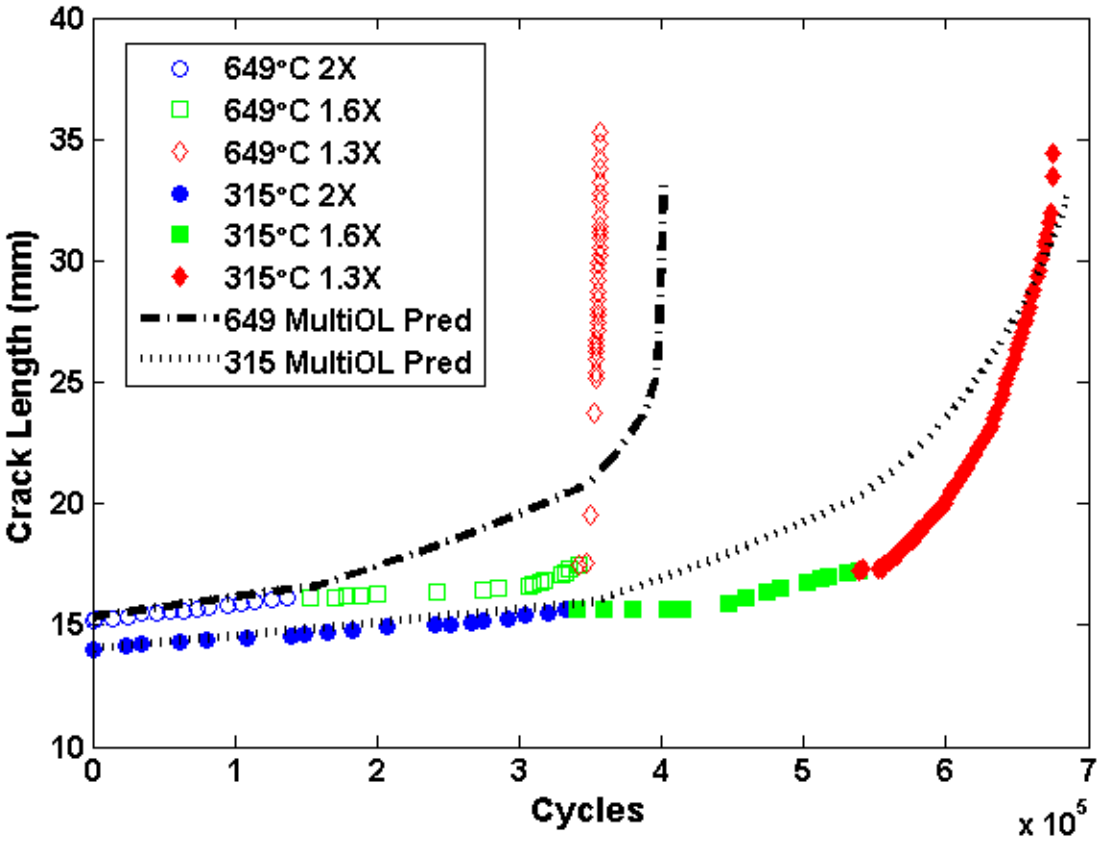

Figure 5.14 - Multiple Overload Data with Multiple Overload Predictions

The multiple overload contribution provides a more accurate prediction than the accumulation of single overloads. However, the transition regions between the 2.0X, 1.6X, and 1.3X overloads are not fully captured by the model. The 2.0X overloads are predicated well, but the 1.6X overloads experience crack arrest for a period before they resume growth. This transition period is believed to be caused by the interaction between the final 2.0X overload and the 1.6X overload growth region. Once the crack grows out of the influence of the 2.0X overload zone, the rate of crack growth during the last portion of the 1.6X region is closer to what is predicted by the model. This transition period is also seen to a lesser extent between the 1.6X and 1.3X overloads. The model

does predict a transition region; however, subsequent work is needed to increase the model's accuracy in the transition region.

5.3.3 Variable Temperature

Additional test data gathered by Adair [63] included constant amplitude crack growth tests with the temperature changing between 315℃ and 649℃. Three different conditions were studied on a single specimen by changing the temperature every 1, 10, and 100 cycles. Figure 5.15 shows the results of this study along with the temperature interaction and non-interaction predictions.

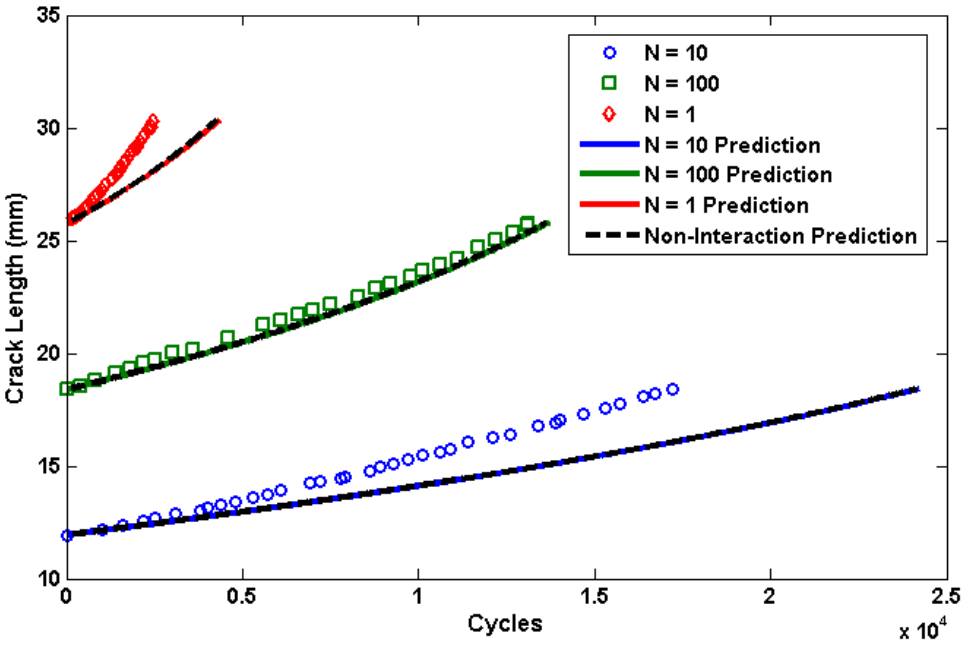

Figure 5.15 - Changing Temperature Data with Temperature Interaction and Non-Interaction Predictions

It is immediately apparent that the temperature interactions do not deviate much from the non-interaction predictions. If the resolution were to be increased, one would see a

slight increase in the crack growth rate of the non-interaction prediction. This is due to the larger yield zone created by lower yield strength at higher temperatures. This effect is minimal in nickel base superalloys, but it can be a significant contribution in materials with large temperature dependencies on yield strength.

Temperature interaction effects are the primary cause of the differences in behavior between the prediction and experimental results. The higher temperature cycles create a thermally affected zone consisting of oxidation and microstructural evolution, which increases crack growth in the subsequent lower temperature cycles. This effect is most prevalent in the case where temperature changes every cycle (N=1) and every 10 cycles (N=10). The case where temperature changes every 100 cycles (N=100) has less of an effect than the previous two cases because the lower temperature growth exceeds the heat effected zone in the first few cycles and continued growth occurs at the nominal constant amplitude crack growth rates. In order to quantify the effect of temperature embrittlement, a subroutine was added to the model to account for increases in crack growth due to cracks growing in regions previously heated to high temperatures. Figure 5.16 shows the results that consider enhanced thermally affected crack growth rates.

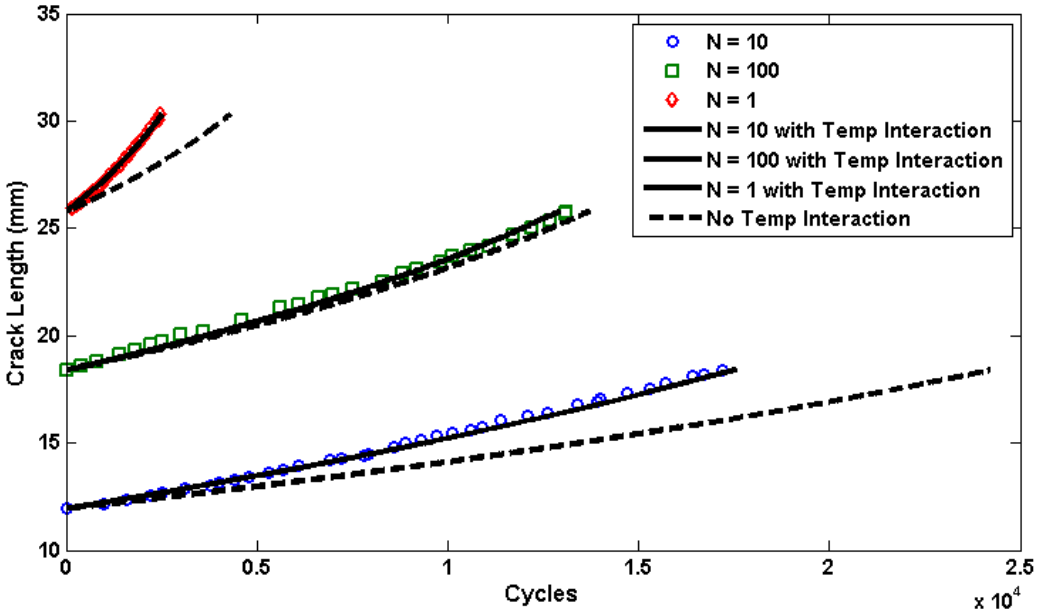

Figure 5.16 - Results of Changing Temperature Crack Growth Test with Temperature Interaction Predictions

The predictions closely match test data by assuming that crack growth in the thermally affected zone grows four times faster than the non-temperature interaction crack growth rates. The difference between the temperature interaction and non-interaction predictions decreases with the number of cycles between temperature changes since the thermally affected zone is very localized and it only takes a few cycles to exceed the boundary. Temperature interaction effects are less pronounced at faster crack growth rates since growth through the thermally affected zone occurs quickly.

It is assumed that the thermally affected zone consists of oxygen affected material along with changes in the material's internal structure which is less resistant to fatigue cracking compared to virgin material. Oxide growth is visually apparent on the surface of the specimen, but an appreciable amount of oxide depth was not seen through optical microscopy. Therefore, it is determined that other changes to the material's

microstructure contribute to the thermally affected zone. As seen previously in section 4.2, yielding material that was previously deformed at higher temperatures resulted in increased hardening followed by an unstable strain burst. This phenomenon was explained through a dynamic strain ageing process and could be occurring at a smaller scale within the yield zone at a crack tip. The studies performed by Jones [38] showed accelerated crack growth in pre-strained titanium alloys due to energy dissipation occurring through cracking rather than plastic deformation (see section 2.6.4). This can also occur in IN-100 within a zone of hardened material created by diffusing solute atoms at high temperatures. Considering these factors, it is concluded that high temperatures create a zone of weakened material more susceptible to fatigue cracking at subsequent lower temperatures.

5.4 Parametric Study

5.4.1 Temperature Interpolation

A parametric study was conducted to better understand the influence of several parameters on crack growth predictions. Constant amplitude crack growth predictions within the allowable temperature range is a good indication that the model is correctly predicting the right crack growth rates at a given ΔK and temperature. Figure 5.2 already provides a MATLAB fit to the constant amplitude data at the three experimental temperatures, but it is important to ensure a consistent trend for predictions made at temperatures between experimental data. Therefore, constant amplitude predictions were made at 400°C and 565°C, as shown in figure 5.17. As expected, the 400°C

prediction falls between the 315°C and 482°C data and the 565°C prediction falls between the 482°C and 649°C data.

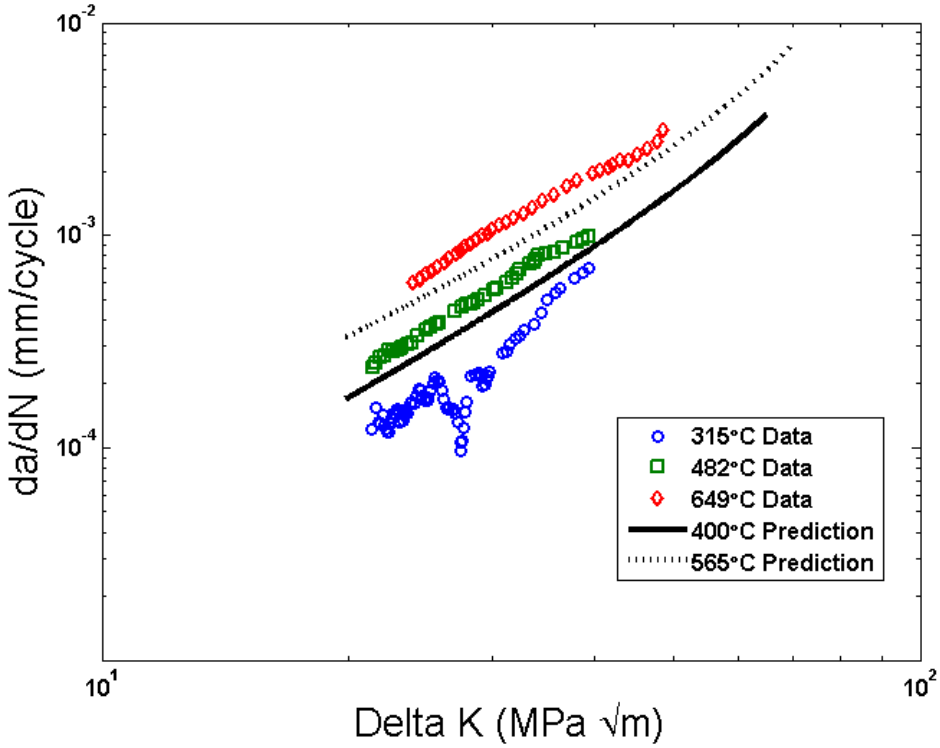

Figure 5.17 - Constant Amplitude Predictions at 400°C and 565°C

5.4.2 Single Overload Effects

The influence of temperature on retardation behavior can be seen by performing a single spike overload at three different temperatures. In this case, a 1.6X overload was applied at 315°C, 482°C, and 649°C. The normalized results are shown in figure 5.18.

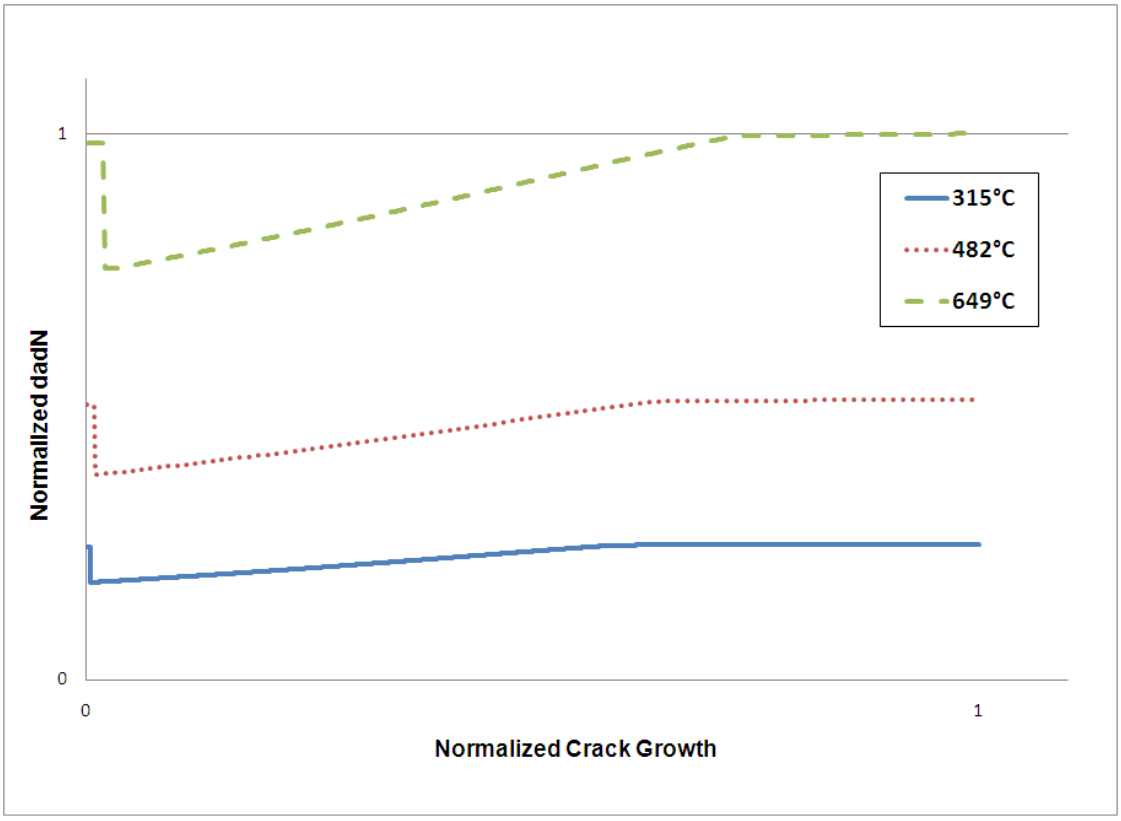

Figure 5.18 - Normalized Crack Growth Rates after a 1.6x Overload

A few observations can be made from the data presented in figure 5.18. First, increasing temperature increases the overall amount of crack growth. This is expected due to the faster constant amplitude crack growth rates at higher temperatures resulting from enhanced oxygen embrittlement at the crack tip. This result is also consistent with the IN-100 overload analysis performed by Macha, shown in section 5.3.1. The second observation is the increasing amount of relative retardation as temperature increases. Yield strength slightly decreases as temperature increases, creating a larger plastic zone which equates to more compressive residual stresses at the crack tip. Although the relative retardation increases with temperature, the overall crack growth rates are still higher given a 1.6x overload. As the overload ratio increases, the amount of retardation

at each temperature also increases. Figure 5.19 shows a 2.0x overload and its effect at different temperatures.

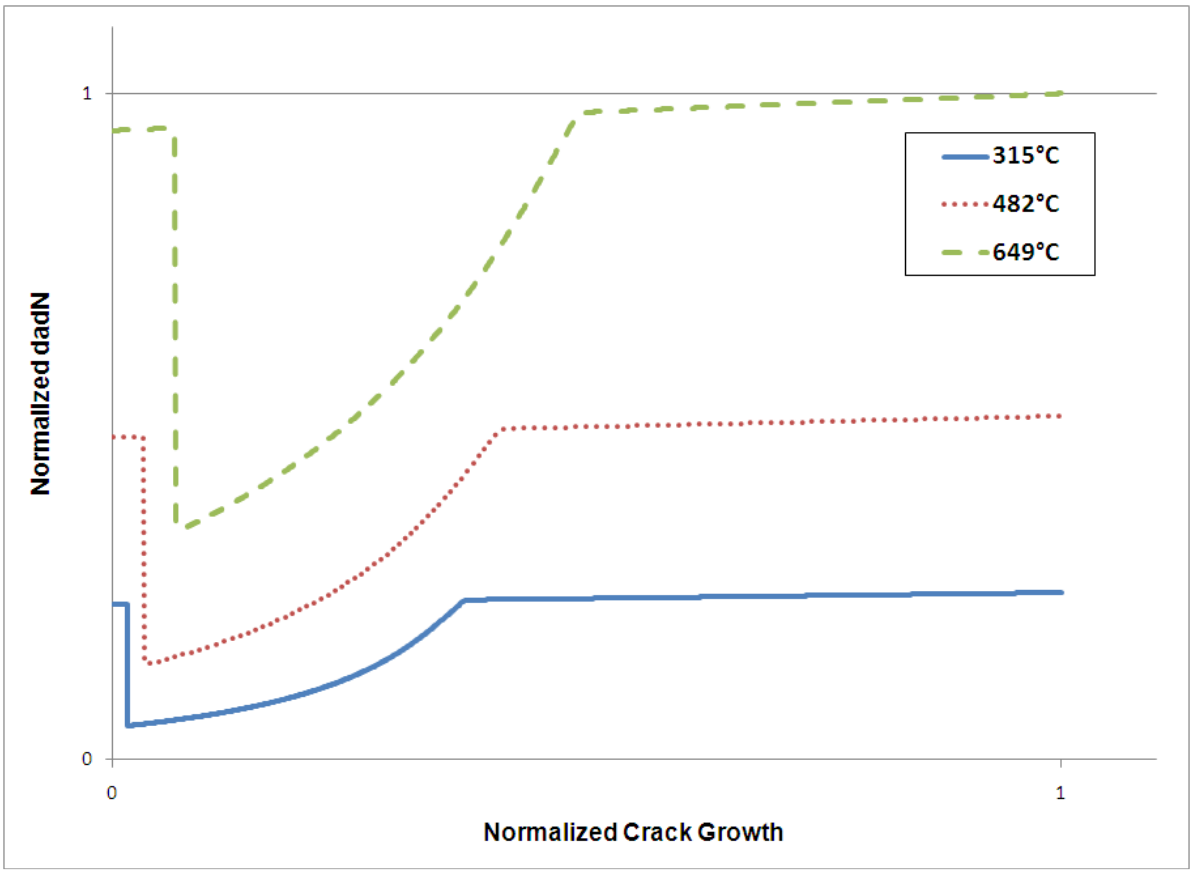

Figure 5.19 - Normalized Crack Growth Rates after a 2.0x Overload

As expected, the 2.0X overloads give considerable more reduction in crack growth rates. Experimental evidence shows the amount of retardation increases exponentially as the overload ratio approaches the cut-off ratio as discussed previously in figure 5.10. It is also apparent that the spread of reduction between temperatures increases at higher overloads, a direct result of the variable cut-off ratio. At high overloads, the retardation difference between temperatures is magnified since lower temperature overloads approach the cut-off ratio before higher temperature overloads.

Another observation from figure 5.18 and figure 5.19 is the increase in retardation distance with temperature. This result is due to the changes in yield strength with temperature, creating larger plastic zone sizes at higher temperatures.

5.4.3 Sample Spectrum

The functionality of this model goes beyond crack growth predictions for specific materials. In addition, this model can be used as a design tool to understand the effects of loading conditions and environment to aid in the material selection and sizing process. A schematic for a turbine engine loading spectrum [67] was converted into actual loads and temperatures which were used as inputs into the model. Figure 5.20 shows a typical schematic for turbine engine components in a TMF environment.

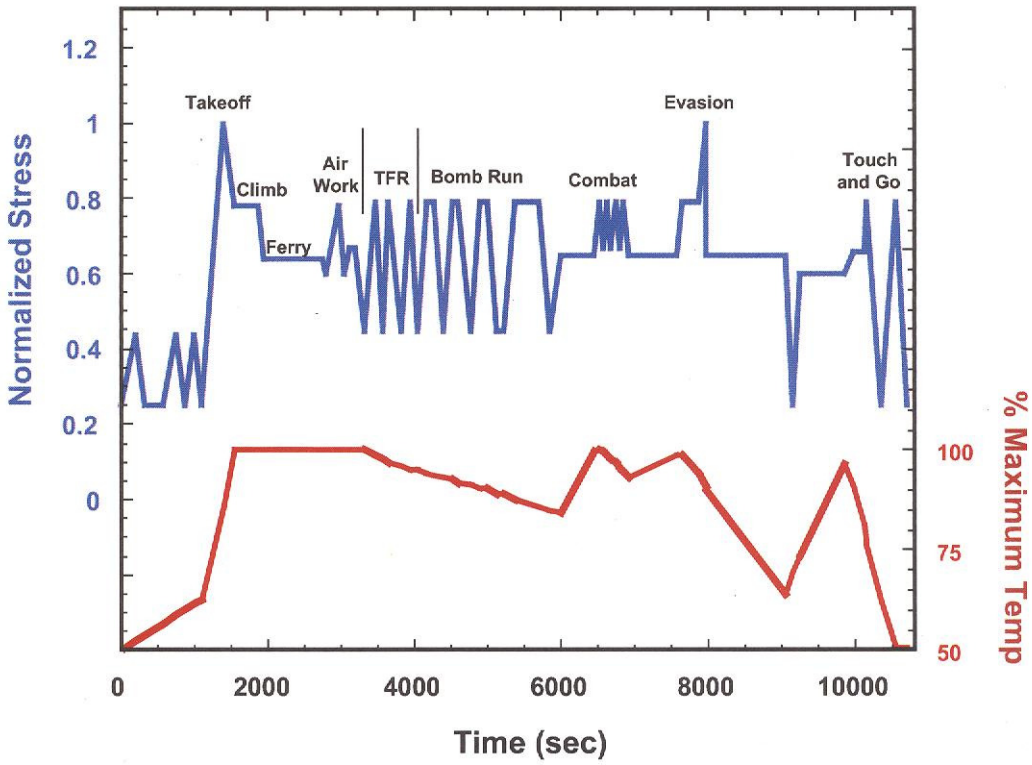

Figure 5.20 - Schematic of a Typical High Temperature Engine Spectrum [67]

Assumptions were made to convert the normalized values of stress and temperature into realistic model inputs. This parametric study assumed a 0.5 mm initial flaw size as the starting crack length. As stated in the background section 2.1.3, centrifugal stresses are the main loading component in turbine disks and the design stresses are between 137-207 MPa [6]. The nominal maximum stress for this spectrum was approximated from the design stress of a turbine disk and the maximum temperature was set at 649°C, the highest temperature used to determine the material properties.

A baseline was established which included all of the model's influencing factors, such as load interaction effects, temperature interaction effects, underloads, multiple overloads,

etc. Figure 5.21 shows the baseline analysis along with predictions showing the influence of each individual factor.

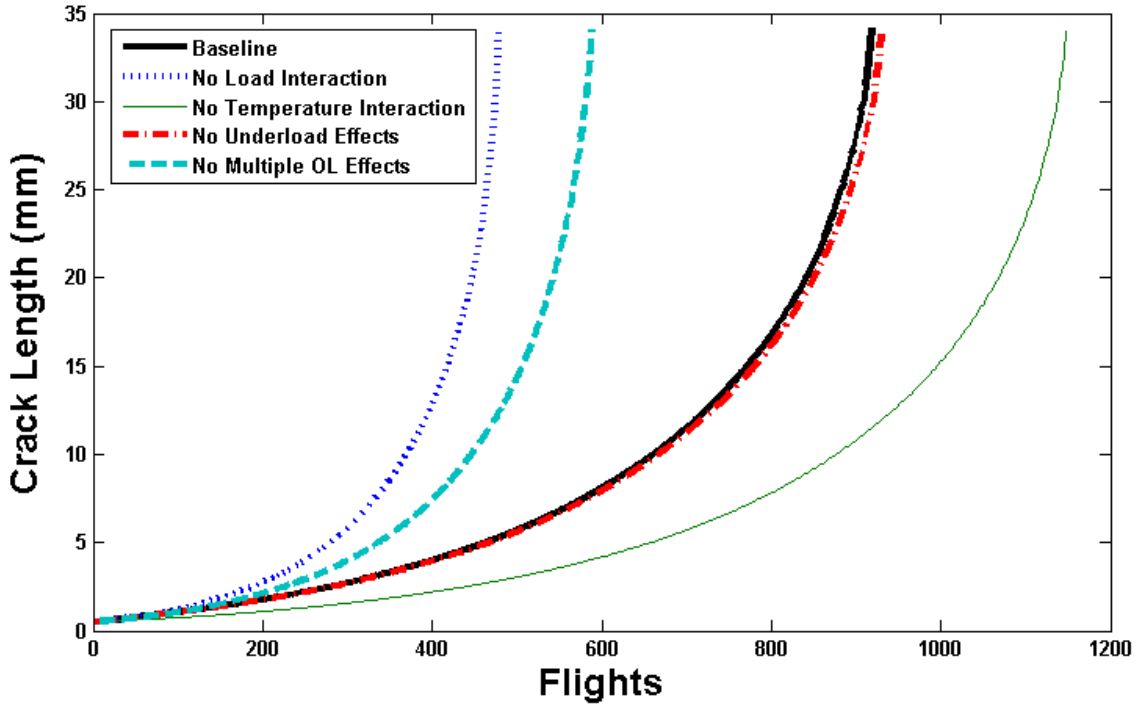

Figure 5.21 - Model Predictions Showing the Influence of Various Parameters

As expected, load interaction effects have significant influence on the lifetime predictions. A 48% reduction in lifetime is attributed to neglecting load interaction effects and ignoring multiple overload effects account for a 36% reduction in lifetime. Turbine engine components experience high loads during take-off, combat maneuvering, or any other event that requires high thrust; which leads to crack growth in areas predominantly controlled by multiple overloads.

Ignoring underload and temperature interaction effects increases the predicted lifetime by 1% and 25%, respectively. This is also expected since underloads negate overload

effects and temperature interaction effects accelerate crack growth in the thermally affected zone, both resulting in faster crack growth. A parametric study was also performed to assess the role of shifting the maximum load and temperature, as shown in figure 5.22.

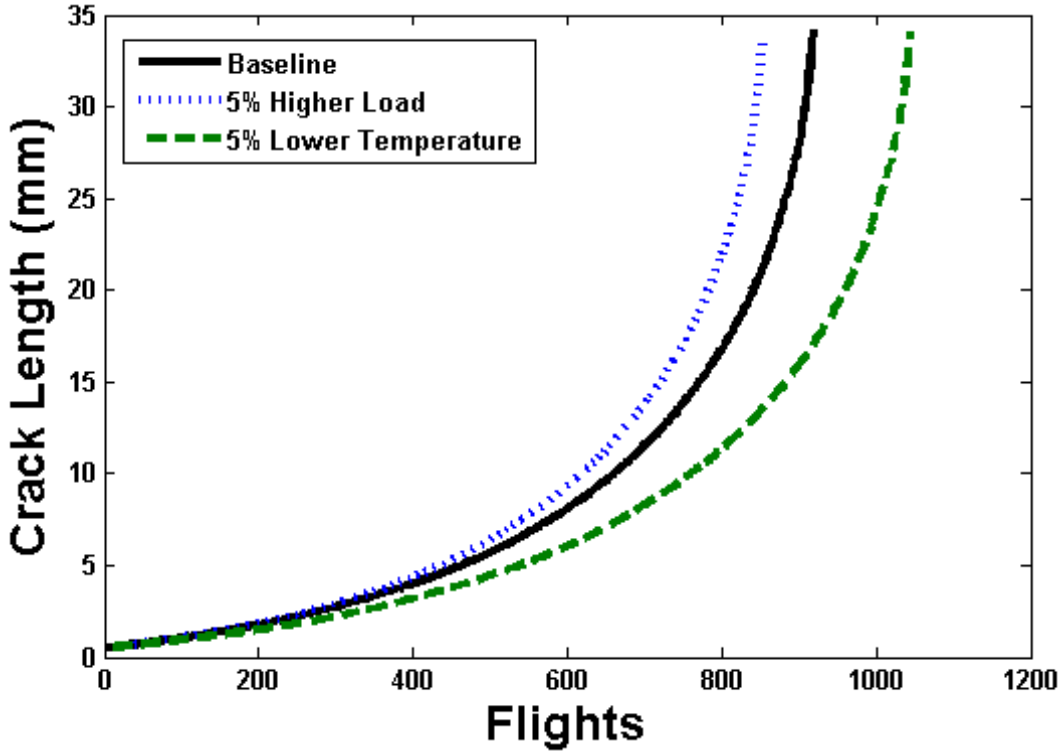

Figure 5.22 - Influence of Increasing Load and Decreasing Temperature on Lifetime Estimates

Increasing the maximum stress profile by 5% results in a 7% reduction in the predicted lifetime. Conversely, reducing the maximum temperature profile by 5% leads to a 14% increase in lifetime predictions. These trends follow the intuition that decreasing the maximum stress and temperature profile is beneficial to increasing the allowable lifetime of engine components. Table 5.4 shows a numerical summary of the model predictions along with the relative change in lifetime compared with the baseline analysis.

Table 5.4 - Numerical Model Predictions of Parametric Study

Factor	Predicted Lifetime (Flights)	Percent Change
Baseline	919	---
5% Higher Loads	853	-7%
5% Lower Temperature	1044	14%
No Load Interaction	479	-48%
No Temperature Interaction	1148	25%
No Underloads	930	1%
No Multiple Overloads	589	-36%

The magnitude of change for each variable is highly dependent on the type of loading spectrum and material. For example, spectrums with more underloads will show a greater dependence on the underload factor and most likely influence the other load interaction factors as well. In addition, different materials will respond differently to load and temperature interaction effects. To represent actual component behavior correctly, the load spectrum and material properties are as crucial as the crack growth model. All three must work together to provide value to the end user.

CHAPTER 6: CONCLUSIONS AND FUTURE WORK

The objective of this research was to create a robust crack growth prediction model that captured the first order effects of TMF crack growth. The proposed physical interactions between the variables influencing crack growth in an engine environment is validated through extensive experimental testing and data analysis. Although it is understood that not all of the physical phenomenon can be captured in a single model, this model serves as a step forward in a relatively undiscovered field of high temperature crack growth predictions in a complex spectrum environment.

6.1 Conclusions

The conclusions of this thesis are divided into two sections: modeling conclusions and experimental conclusions. Since modeling is based upon experimental results, many conclusions drawn from this study are relevant in both cases.

6.1.1 Experimental Conclusions

- Yield strength, with a 0.02% offset, slightly decreases with temperature. This results in larger plastic zones at higher temperatures but not large enough to cause considerable differences in lifetime estimates. Materials with a stronger temperature dependence on yield strength will have greater changes in lifetime predictions.

- Serrated yielding is apparent in the 315°C slow and 482°C fast tensile tests. The Portevin-Le Chatelier effect is the most probable explanation for this behavior in which the solute atoms congregate to the mobile dislocations and cause flow oscillations at specific temperature and strain rate combinations.
- In general, increasing the strain rate or decreasing temperature results in higher values for hardening coefficients. This effect is not immediately apparent by looking at the stress vs. strain curves due to the differences in behavior at the onset of yielding. Some tests exhibited perfectly plastic behavior for a portion of inelastic flow while other tests hardened immediately.
- Enhanced hardening followed by localized strain bursts occurred under certain conditions at the yield point for the changing temperature/cyclic yielding test. This effect was most pronounced when the material would yield after a higher temperature cycle and is most likely a result of a dynamic strain-ageing phenomenon.

6.1.2 Modeling Conclusions

- A yield zone model was used to account for load interaction effects by changing the crack growth rate based upon the relative size difference between the overload plastic zone and nominal plastic zone ahead of the crack tip.
- The residual plastic zone size was derived to be a function of temperature by modifying Gallagher's modification to Willenborg's residual stress intensity factor to include a variable yield stress. This new relationship is:

$$K_R^* = S_y\sqrt{(Z_{OL} - (\Delta a + Z))\pi\alpha} \quad (5.1)$$

- Overload induced retardation was determined to be a function of temperature and overload ratio. This led to a variable cut-off ratio that increases linearly with temperature. The room temperature cut-off ratio is 2.0 and the cut-off ratio at 732℃ is 2.27.
- Multiple overloads create more retardation than single overloads by generating additional compressive fields in the wake of an advancing crack. Realistically, load interaction effects are not limited to a single type of model, i.e. crack closure or yield zone. Experimental evidence supports theories from both models; therefore, it is plausible to combine the effects of both into a single model. This model assumes that overloads applied before the crack grows two times the previous overload zone size will result in additional retardation attributed to multiple overloads. A saturation value determines the lower limit of crack growth retardation due to multiple overloads. The physics behind the multiple overload phenomenon are the result of one set of experimental data. More data is needed to further develop this theory.
- The plastic zone size is not only a function of temperature but also depends on the stress state. Plane stress conditions allow for a larger plastic zone, which can lead to increased retardation. This model compares the overload zone size with the specimen thickness to determine the relative contributions of plane stress and plane strain.
- The thermally affected zone is a region in front of a crack tip that has been weakened by high temperatures. This area is weakened by oxidation and material evolution following high temperature loading cycles. Material evolution

could be caused by a dynamic strain ageing process in which diffusing atoms congregate to dislocations at high temperatures. When the temperature decreases, dislocations become locked by a cloud of solute atoms and this energy barrier must be overcome to cause further dislocation motion. Materials in this state can more easily dissipate energy through cracking rather than plastic deformation.

- Temperature interactions can increase crack growth in areas previously affected by high temperatures and oxide embrittlement. This model calculates the thermally affected zone in front of the crack using a one dimensional diffusion relationship and accelerates subsequent crack growth four times through this region.
- A TMF crack growth prediction code, MPYZ-TMF, has been developed and exercised using a sample engine spectrum to assess the sensitivity of crack growth variables due to single overloads, multiple overloads, underloads, temperature changes, stress profile changes, and temperature profile changes.

6.2 Suggestions for Future Work

Inevitably, with any research project there will be more questions than answers. As is the case with this thesis, there are a few suggestions for future work that will be beneficial to better understand all of the complex mechanisms of TMF crack growth. This list is by no means exhaustive but serves at a starting point for considering future work in the area of modeling high temperature crack growth under the influence of random spectrums.

- Underload experimental data on IN-100 would be beneficial to validate this model further. In addition, temperature effects on underloads are not currently addressed but would give insight into the physics behind underload effects on crack growth.
- High temperatures can relax the residual stresses obtained from an overload and change the retardation behavior. This behavior was shown by Ling and Schijve [72] in retardation studies in aluminum alloys. In a TMF environment under variable amplitude loading, this effect can have significant relevance. This issue is not currently addressed by this model but would be a great addition to future work.
- A more comprehensive library of specimen geometries would increase the applicability of this model. Cracks growing from holes, surface flaws, and corner cracks are just a few cases that should be considered in the design and analysis process.
- Experimental data generated for a typical engine loading spectrum would be a great way to see how well the model will predict to an actual crack growing under turbine engine conditions. The parametric study performed in this research shows the trends of changing several variables but there are no means to compare the results to actual data.
- Frequency effects on crack growth are not explicitly defined in the model; however, they are considered to influence temperature interaction effects indirectly. Frequency effects on isothermal crack growth tests should be considered for future additions to the model.
- The Portevin-Le Chatelier effect has the potential to influence the crack growth rate; however, the significance of this phenomenon is not known. The current

model does not directly account for this effect since it is not considered a primary driver in crack growth and it only occurs under certain conditions.

Much more experimental testing on IN-100 is required in order to fully develop this model to a level of confidence high enough to be used in component life prediction. The basic model framework is in place.

APPENDIX

Running the Model

An executable file is used to run the simulations based upon the user-defined inputs. These inputs must be created prior to executing the crack growth model. See section 5.2.2 for details on the input files. Once the input files have been created, all of the files must be placed within the same folder. This includes both input files and the .exe file. During execution, the software will look for other input files and it only searches within the same directory for which the application was executed. After the entire package is together in the same directory, the .exe file can be executed.

A command window will appear on the screen since this software was written as a console application. It will ask the user to define a material input file, which must be specified exactly as how the name appears in the directory, including the .txt file extension. The next question will ask the user to specify the load spectrum file. Again, this file must be inputted exactly as it appears in the directory. Otherwise, the program will not be able to locate the file and the execution will terminate. Figure A1 shows the command window with sample inputs for both the material and load spectrum file.

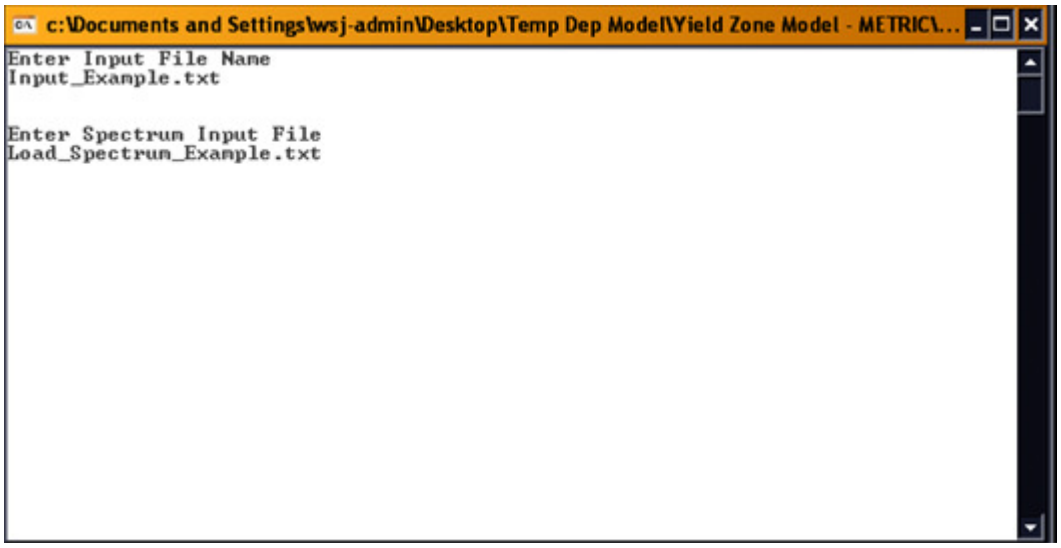

Figure A1 - Command Window with Material and Spectrum File Inputs

After both input files have been inputted, the user will be asked to specify the specimen geometry as shown in figure A2. The model will only accept single digit numerical inputs, one through five.

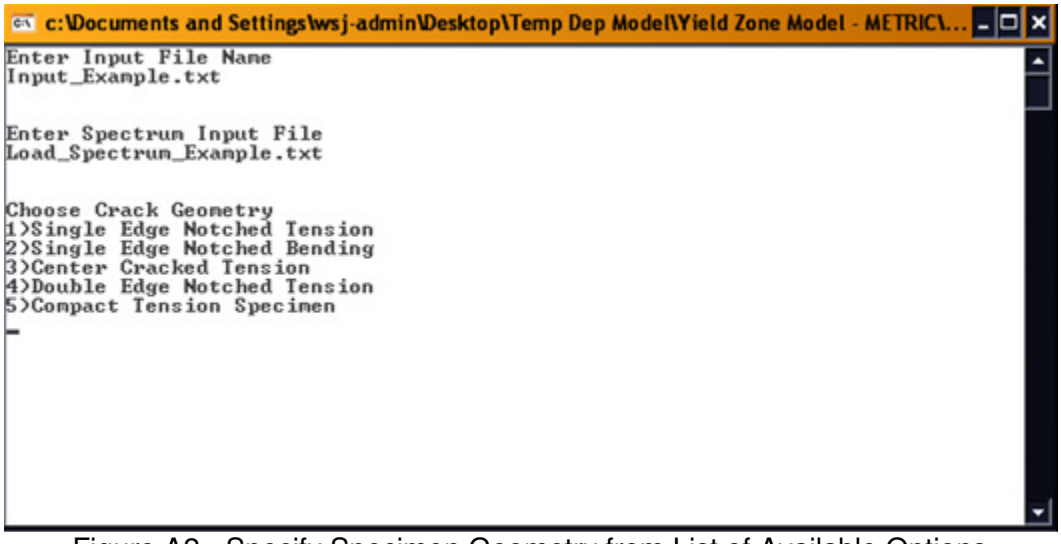

Figure A2 - Specify Specimen Geometry from List of Available Options

Once the specimen geometry is chosen, the next two questions will ask the user to determine which prediction code to use, either Paris or Foreman, and indicate the maximum number of cycles to run. The program will loop to the beginning of the load input file if the maximum number of cycles specified by the user is greater than the number of cycles in the load input file. This looping will occur until either the maximum number of cycles has been reached, or the specimen reaches failure. Figure A3 shows the input screen after this step.

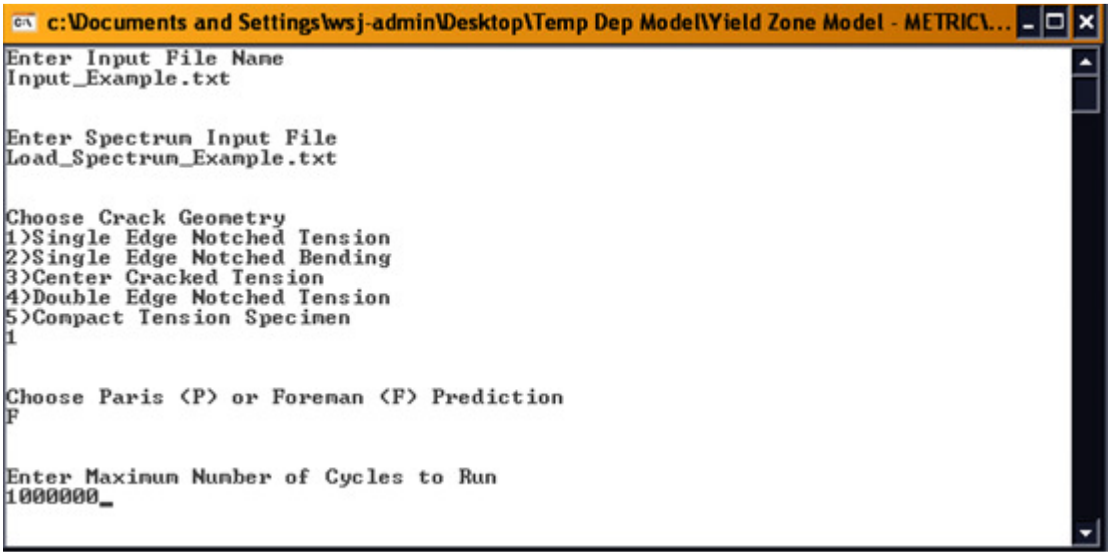

Figure A3 - Choosing a Prediction Method and Maximum Number of Cycles

The following options will ask if the user wishes to include load interaction effects, oxide induced acceleration effects, underload effects, and multiple overload effects. The appropriate inputs to these questions are either “y” or “n” depending on preference. Not including load interaction effects or temperature interaction effects will calculate crack growth based upon the constant amplitude growth rates. Figure A4 shows the console application after these decisions have been made.

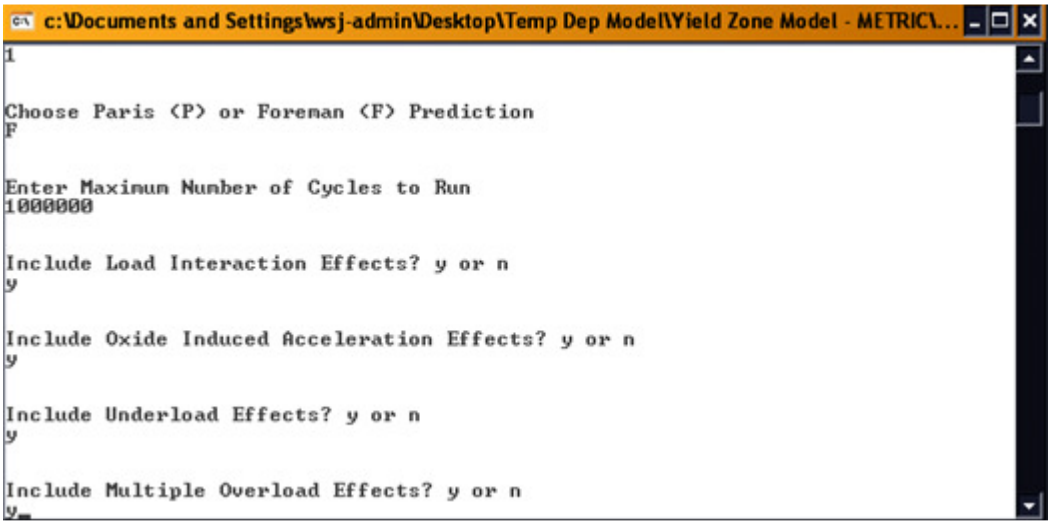

Figure A4 - User Decisions to Include Load and Temperature Interaction Effects

The model will calculate the crack growth cycle-by-cycle until failure or the maximum number of cycles is reached. The next information that will be displayed on the screen is the final crack length after the model has completed the crack growth analysis. The following question will ask the user to save the resulting analysis, as shown in figure A5.

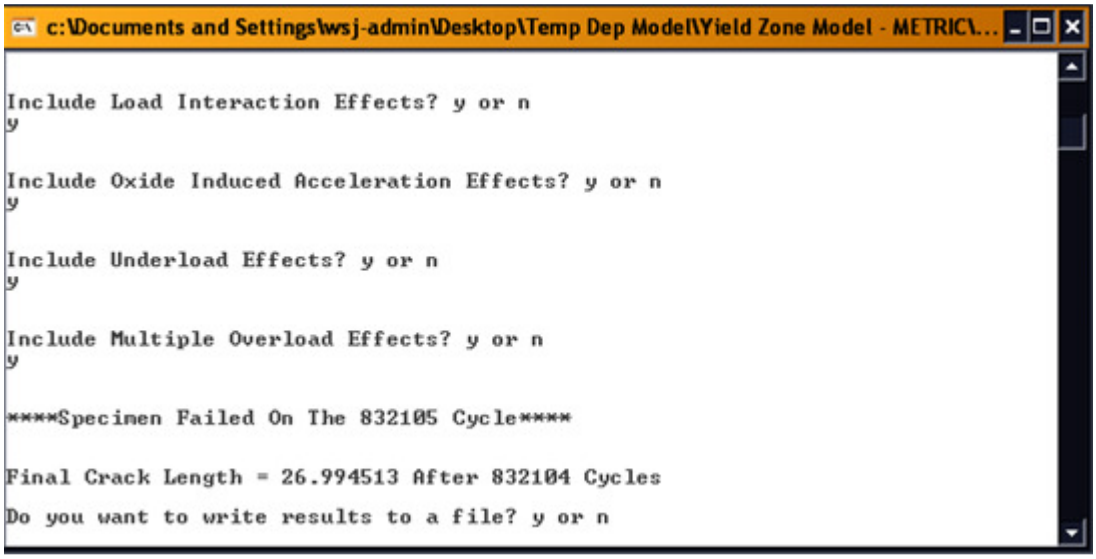

Figure A5 - Initial Results from Analysis and Option to Write Results to a File

The last two questions will ask the user to specify the number of output points and an appropriate file name. The number of output points will divide the total number of cycles into equally spaced segments to save disk space and speed up the output process. The output categories are: cycles, crack length, K_{max}, K_{min}, ΔK, and dadN. It is important to provide a ".txt" extension to the output file name to view the files correctly. Output files will be saved into the same folder as the executable and input files and the information can be recognized by most data analysis software tools.

REFERENCES

1. Dauntless-Soft. *AA 767 High Pressure Turbine Failure*. 2006 [cited 2011 April 3]; Available from: http://www.dauntless-soft.com/PRODUCTS/Freebies/AAEngine/.

2. Australian Transport Safety Bureau, *In-Flight Uncontained Engine Failure Overhead Batam Island, Indonesia 4 November 2010 VH-OQA Airbus A380-842*. 2010, Canberra City. p. 53.

3. Woods, I. *Rolls-Royce Narrows In On A380 Engine Fault*. 2010 [cited 2011 April 3]; Available from: http://news.sky.com/skynews/Home/Business/Qantas-Finds-Problems-With-Engines-Of-Airbus-A380-Superjumbos-Following-Singapore-Emergency-Landing/Article/201011215796910?f=rss.

4. Flack, R., *Fundamentals of Jet Propulsion with Applications*. 2005, New York: Cambridge University Press. p. 4-43.

5. Turns, S., *Thermal-Fluid Sciences: an Integrated Approach*. 2006, New York: Cambridge University Press. p. 1000-1006.

6. Mattingly, J.D., W.H. Heiser, and D.T. Pratt, *Aircraft Engine Design*. 2nd ed, ed. J.S. Przemieniecki. 2002, Reston, Virginia: American Institute of Aeronautics and Astronautics.

7. Donachie, M.J. and S.J. Donachie, *Superalloys: a Technical Guide*. 2nd ed. 2002, Materials Park, OH: ASM International. 439 p.

8. Durand-Charre, M., *The Microstructure of Superalloys*. 1997, Boca Raton, Florida: CRC Press. 170 p.

9. Wusatowska-Sarnek, A.M., M.J. Blackburn, and M. Aindow, *Techniques for Microstructural Characterization of Powder-Processed Nickel-Based Superalloys.* Materials Science and Engineering A, 2003. **360**(1-2): p. 390-395.

10. Beardmore, P., R.G. Davies, and T.L. Johnston, *Temperature Dependence of the Flow Stress of Nickel-Base Alloys.* Transactions of the Metallurgical Society of AIME, 1969. **245**(7): p. 1537-1545.

11. Shenoy, M., Y. Tjiptowidjojo, and D. McDowell, *Microstructure-Sensitive Modeling of Polycrystalline IN 100.* International Journal of Plasticity, 2008. **24**(10): p. 1694-1730.

12. Kear, B. and H. Wilsdorf, *Dislocation Configurations in Plastically Deformed Polycrystalline Cu3Au Alloys.* Transactions of the Metallurgical Society of AIME, 1961. **224**: p. 382-386.

13. Hardrath, H., *A Unified Technology Plan for Fatigue and Fracture Design*. NASA Technical Memorandum X-71923. 1973, Hampton: NASA Langley Research Center. 22 p.

14. Bannantine, J., J. Comer, and J. Handrock, *Fundamentals of Metal Fatigue Analysis*, ed. J. Wenzel. 1990: Prentice Hall Englewood Cliffs, NJ. 273 p.

15. Bathias, *There is No Infinite Fatigue Life in Metallic Materials.* Fatigue & Fracture of Engineering Materials & Structures, 1999. **22**(7): p. 559-565.

16. Miller and O'donnell, *The Fatigue Limit and its Elimination.* Fatigue & Fracture of Engineering Materials & Structures, 1999. **22**(7): p. 545-557.

17. Griffith, A., *The Phenomena of Rupture and Flow in Solids.* Philosophical Transactions of the Royal Society of London. Series A, 1921. **221**: p. 163-198.

18. Irwin, G., *Fracture dynamics.* Fracturing of Metals, American Society of Metals, Cleveland, OH, 1948: p. 147-166.

19. Irwin, G., *Analysis of Stresses and Strains Near the End of a Crack Traversing a Plate.* Journal of Applied Mechanics, 1958. **24**: p. 361-364.

20. Paris, P., M. Gomez, and W. Anderson, *A Rational Analytic Theory of Fatigue.* The Trend in Engineering, 1961. **13**(1).

21. Orowan, E., *Fracture and Strength of Solids.* Reports on Progress in Physics, 1948. **12**: p. 185.

22. Ghonem, H., T. Nicholas, and A. Pineau, *Elevated Temperature Fatigue Crack Growth in Alloy 718 - Part I: Effects of Mechanical Variables.* Fatigue & Fracture of Engineering Materials & Structures, 1993. **16**(5): p. 565-576.

23. Reger, M. and L. Remy, *High Temperature, Low Cycle Fatigue of IN-100 Superalloy II: Influence of Frequency and Environment at High Temperatures.* Materials Science and Engineering: A, 1988. **101**: p. 55-63.

24. Raj, R. and M. Ashby, *Intergranular Fracture at Elevated Temperature.* Acta Metallurgica, 1975. **23**(6): p. 653-666.

25. Willenborg, J., R. Engle, and H. Wood, *A Crack Growth Retardation Model Using an Effective Stress Concept*. 1971, AFFDL TM-71-1-FBR. p. 22.

26. Wheeler, O.E., *Spectrum Loading and Crack Growth.* Journal of Basic Engineering, 1972. **94**(1): p. 181-186.

27. Gallagher, J.P. and T.F. Hughes, *Influence of Yield Strength on Overload Affected Fatigue Crack Growth Behavior in 4340 Steel*. 1974, Ft. Belvoir: AFFDL-TR-74-27. 53 p.

28. Johnson, W., *Multi-parameter yield zone model for predicting spectrum crack growth.* Methods and Models for Predicting Fatigue Crack Growth Under Random Loading, ASTM STP 748, 1981: p. 85–102.

29. Alzos, W., A. Skat Jr, and B. Hillberry, *Effect of Single Overload/Underload Cycles on Fatigue Crack Propagation.* Fatigue Crack Growth under Spectrum Loads, ASTM STP 595, 1976: p. 41-60.

30. Chang, J. and C. Hudson, *Methods and Models for Predicting Fatigue Crack Growth Under Random Loading, ASTM STP 748.* ASTM, Philadelphia, Pa, 1981: p. 140.

31. Skorupa, M., *Load Interaction Effects during Fatigue Crack Growth under Variable Amplitude Loading - a Literature Review. Part II: Qualitative Interpretation.* Fatigue & Fracture of Engineering Materials & Structures, 1999. **22**(10): p. 905-926.

32. Christensen, R., *Fatigue crack, fatigue damage and their detection*. Metal Fatigue. 1959, New York: McGraw-Hill.

33. Fleck, N., *Fatigue Crack Growth due to Periodic Underloads and Overloads.* Acta Metallurgica, 1985. **33**(7): p. 1339-1354.

34. Busch, M.L. and J.L. Lebrun, *X-Ray Diffraction Study of Stress Distributions Following a Single Tensile Overload.* Fatigue Crack Growth Under Variable Amplitude Loading, 1988: p. 76-86.

35. Elber, W., *Fatigue Crack Closure Under Cyclic Tension.* Engineering Fracture Mechanics, 1970. **2**(1): p. 37-45.

36. Elber, W., *Damage Tolerance in Aircraft Structures.* ASTM STP 486, 1971: p. 230-242.

37. Newman, J., *A Crack Closure Model for Predicting Fatigue Crack Growth under Aircraft Spectrum Loading.* Methods and Models for Predicting Fatigue Crack Growth Under Random Loading, ASTM 748, 1981: p. 53.

38. Jones, R., *Fatigue Crack Growth Retardation after Single-Cycle Peak Overload in Ti-6Al-4V Titanium Alloy.* Engineering Fracture Mechanics, 1973. **5**(3): p. 585-588.

39. Schijve, J., *Fatigue Damage Accumulation and Incompatible Crack Front Orientation.* Engineering Fracture Mechanics, 1974. **6**(2): p. 245-252.

40. Schijve, J., *Shear Lips on Fatigue Fractures in Aluminium Alloy Sheet Material.* Engineering Fracture Mechanics, 1981. **14**(4): p. 789-800.

41. Boyd-Lee, A.D., *Fatigue Crack Growth Resistant Microstructures in Polycrystalline Ni-base Superalloys for Aeroengines.* International Journal of Fatigue, 1999. **21**(4): p. 393-405.

42. Suresh, S., *Micromechanisms of Fatigue Crack Growth Retardation Following Overloads.* Engineering Fracture Mechanics, 1983. **18**(3): p. 577-593.

43. Suresh, S., G. Zamiski, and D. Ritchie, *Oxide-Induced Crack Closure: An Explanation for Near-Threshold Corrosion Fatigue Crack Growth Behavior.* Metallurgical and Materials Transactions A, 1981. **12**(8): p. 1435-1443.

44. Toyosada, M. and T. Niwa, *The Significance of RPG Load for Fatigue Crack Propagation and the Development of a Compliance Measuring System.* International Journal of Fracture, 1994. **67**(3): p. 217-230.

45. Xiong, Y., J. Katsuta, K. Kawano, and T. Sakiyama, *Characteristics of Fatigue Crack Propagation Behaviour as Identified by Hysteresis Loop at the Crack Tip.* Fatigue & Fracture of Engineering Materials & Structures, 2006. **29**(6): p. 454-463.

46. Xiong, Y., J. Katsuta, K. Kawano, and T. Sakiyama, *Examination of Fatigue Crack Driving Force Parameter.* Fatigue & Fracture of Engineering Materials & Structures, 2008. **31**(9): p. 754-765.

47. Sadananda, K., A. Vasudevan, R. Holtz, and E. Lee, *Analysis of Overload Effects and Related Phenomena.* International Journal of Fatigue, 1999. **21**: p. 233-246.

48. Robinson, J.M. and M.P. Shaw, *Microstructural and Mechanical Influences on Dynamic Strain Aging Phenomena.* International Materials Reviews, 1994. **39**(3): p. 11.

49. Rodriguez, P., *Serrated Plastic Flow.* Bulletin of Materials Science, 1984. **6**(4): p. 653-663.

50. Stanford, N., I. Sabirov, G. Sha, A. La Fontaine, S. Ringer, and M. Barnett, *Effect of Al and Gd Solutes on the Strain Rate Sensitivity of Magnesium Alloys.* Metallurgical and Materials Transactions A, 2010. **41**(3): p. 734-743.

51. Cuddy, L. and W. Leslie, *Some Aspects of Serrated Yielding in Substitutional Solid Solutions of Iron.* Acta Metallurgica, 1972. **20**(10): p. 1157-1167.

52. Pink, E. and A. Grinberg, *Serrated Flow in a Ferritic Stainless Steel.* Materials Science and Engineering, 1981. **51**(1): p. 1-8.

53. Wijler, A., J. Van Westrum, and A. Van den Beukel, *A New Type of Stress-Strain Curve and the Portevin-Le Chatelier Effect in Au (14 at.% Cu).* Acta Metallurgica, 1972. **20**(3): p. 355-362.

54. Kim, I. and M. Chaturvedi, *Serrated Flow in Al-5 wt.% Mg Alloy.* Materials Science and Engineering, 1979. **37**(2): p. 165-172.

55. Prasad, K., R. Sarkar, P. Ghosal, and V. Kumar, *Tensile Deformation Behaviour of Forged Disc of IN 718 Superalloy at 650 °C.* Materials & Design, 2010. **31**(9): p. 4502-4507.

56. Hayes, R.W., *On a Proposed Theory for the Disappearance of Serrated Flow in F.C.C. Ni Alloys.* Acta Metallurgica, 1983. **31**(3): p. 365-371.

57. Hayes, R.W. and W.C. Hayes, *On the Mechanism of Delayed Discontinuous Plastic Flow in an Age-Hardened Nickel Alloy.* Acta Metallurgica, 1982. **30**(7): p. 1295-1301.

58. Hong, S.G. and S.B. Lee, *Mechanism of Dynamic Strain Aging and Characterization of its Effect on the Low-Cycle Fatigue Behavior in type 316L Stainless Steel.* Journal of Nuclear Materials, 2005. **340**(2-3): p. 307-314.

59. Reed, R.C., *The Superalloys: Fundamentals and Applications*. 2006, New York: Cambridge University Press. 372 p.

60. Gabb, T.P., J. Telesman, A. Garg, P. Lin, V. Provenzano, R. Heard, and H.M. Miller, *Grain Boundary Engineering the Mechanical Properties of Allvac 718 PlusTM Superalloy.* NASA TM - 2010-216935, 2010: p. 1-26.

61. Ricks, R., A. Porter, and R. Ecob, *The Growth of Gamma Prime Precipitates in Nickel-Base Superalloys.* Acta Metallurgica, 1983. **31**(1): p. 43-53.

62. Jha, S., M. Caton, and J. Larsen, *A New Paradigm of Fatigue Variability Behavior and Implications for Life Prediction.* Materials Science and Engineering: A, 2007. **468**: p. 23-32.

63. Adair, B., *Thermo-Mechanical Fatigue Crack Growth of a Polycrystalline Superalloy*, in *Woodruff School of Mechanical Engineering*. 2010, MS Thesis, Georgia Institute of Technology: Atlanta.

64. Cailletaud, G. and J. Chaboche, *Macroscopic Description of the Microstructural Changes Induced by Varying Temperature: Example of IN 100 Cyclic Behavior.* Mechanical Behavior of Materials, 1979. **2**: p. 23-32.

65. Penning, P., *Mathematics of the Portevin-Le Chatelier effect.* Acta Metallurgica, 1972. **20**(10): p. 1169-1175.

66. Macha, D.E., *Fatigue Crack Growth Retardation Behavior of IN-100 at Elevated Temperature.* Engineering Fracture Mechanics, 1979. **12**(1): p. 1-11.

67. Larsen, J.M., A.H. Rosenberger, G.A. Hartman, S.M. Russ, and R. John, *The Role of Spectrum Loading in Damage-Tolerance Life-Management of Fracture Critical Turbine Engine Components*, in *RTO AVT Symposium*. 2001: Manchester, UK. p. 1-12.

68. Wang, G.S. and A.F. Blom, *A Strip Model for Fatigue Crack Growth Predictions under General Load Conditions.* Engineering Fracture Mechanics, 1991. **40**(3): p. 507-533.

69. Shuter, D.M. and W. Geary, *Some Aspects of Fatigue Crack Growth Retardation Behavior Following Tensile Overloads in a Structural Steel.* Fatigue & Fracture of Engineering Materials & Structures, 1996. **19**(2-3): p. 185-199.

70. Zhang, J., X. He, and S. Du, *Analysis of the Effects of Compressive Stresses on Fatigue Crack Propagation Rate.* International Journal of Fatigue, 2007. **29**(9-11): p. 1751-1756.

71. Silva, F., *Crack Closure Inadequacy at Negative Stress Ratios.* International Journal of Fatigue, 2004. **26**(3): p. 241-252.

72. Ling, M.R. and J. Schijve, *The Effect of Intermediate Heat Treatments on Overload Induced Retardations during Fatigue Crack Growth in an Al-Alloy.* Fatigue & Fracture of Engineering Materials & Structures, 1992. **15**(5): p. 421-430.